UNIVERSITY OF CALIFORNIA
Santa Barbara

Signal Processing/Hardware Co-Design for High-Speed A/D Conversion and Millimeterwave Sensor Nets

A Dissertation submitted in partial satisfaction
of the requirements for the degree of

Doctor of Philosophy

in

Electrical and Computer Engineering

by

Munkyo Seo

Committee in Charge:

Professor Mark Rodwell, Chair

Professor Stephen Long

Professor Upamanyu Madhow

Professor Robert York

Professor Patrick Yue

December 2007

The Dissertation of
Munkyo Seo is approved:

Professor Stephen Long

Professor Upamanyu Madhow

Professor Robert York

Professor Patrick Yue

Professor Mark Rodwell, Committee Chairperson

December 2007

Signal Processing/Hardware Co-Design for High-Speed A/D Conversion and Millimeterwave Sensor Nets

by

Munkyo Seo

Acknowledgements

I would like to acknowledge and thank my advisors Professor Mark Rodwell and Professor Upamanyu Madhow. Their guidance, expertise and the unique interdisciplinary environment have made this dissertation possible. Their passion and professionalism in academic research always make me question myself: *Am I doing my best?*

I would like to thank my Ph.D. committee members Professor Steve Long, Professor Robert York and Professor Patrick Yue, for many suggestions and discussions, which significantly improved the dissertation.

I would like to thank all members in Professor Rodwell's, Professor Madhow's and Professor Yue's research group, for enduring my inquisitiveness, for numerous discussions, and for overnight experiments.

I would like to thank my parents, in-laws, sisters and especially my wife Sukkyung, for unconditional support, except that I do not know how to thank them enough.

Curriculum Vitæ
Munkyo Seo

Education

2007	Doctor of Philosophy in Electrical and Computer Engineering, University of California, Santa Barbara, CA.
1996	M.S. in Engineering, Seoul National University, Seoul, Korea
1994	B.S. in Engineering, Seoul National University, Seoul, Korea

Experience

2003 – 2007	Research Assistant, Dept. of Electrical and Computer Engineering, University of California, Santa Barbara, CA
2006	Summer intern, Intel Corporation, Hillsboro, OR
2001 – 2002	Senior Engineer, Mobile Handset R&D Group, LG Electronics, Korea
1997 – 2001	Research Engineer, Transmission Systems R&D Group, LG Electronics, Korea
1996 – 1997	Research Assistant, Applied Electromagnetics Lab, Seoul National University, Korea

Fields of Study

Millimeter-wave circuits and systems, adaptive signal processing, and numerical analysis techniques for nonlinear circuits.

Publications

M. Seo, M. Rodwell and U. Madhow, "A feedback-based distributed phased array technique and its application to 60-GHz wireless sensor network," *submitted to 2008 IEEE Int. Microwave Symposium (IMS).*

M. Seo, and M. Rodwell, "Mixed-domain adaptive blind correction of high-resolution time-interleaved ADCs: Theory and experiment," *IEEE Trans. Circuits and Systems-I: Regular papers*, under review.

M. Seo, M. Rodwell and U. Madhow, "Comprehensive digital correction of mismatch errors for a 400-MSamples/S, 80-dB SFDR time-interleaved analog-to-digital converter," *IEEE Trans. Microwave Theory Tech.*, vol. 53, no. 3, pp. 1072-1082, Mar. 2005.

V. Paidi, Z. Griffith, Y. Wei, M. Dahlstrom, M. Urteaga, N. Parthasarathy, M. Seo, L. Samoska, A. Fung, M. Rodwell,, "G-band (140-220-GHz) and W-band (75-110-GHz) InP DHBT Power Amplifiers," *IEEE Trans. Microwave Theory Tech.*, vol. 53, no. 2, pp. 598-605, Feb. 2005.

M. Seo, B. Ananthasubramaniam, M. Rodwell and U. Madhow, "Recent progress on a 60-GHz imaging sensor network," *40th Asilomar Conference on Signals, Systems, and Computers*, Pacific Grove, CA, Oct. 2007.

M. Seo, B. Ananthasubramaniam, M. Rodwell and U. Madhow, "Millimeterwave imaging sensor nets: A scalable 60-GHz wireless sensor network," *IEEE Int. Microwave Symposium (IMS)*, Honolulu, HI, pp. 563-566, June 2007.

M. Seo and M. Rodwell, "Generalized blind mismatch correction for a two-channel time-interleaved ADC: Analytic approach," *IEEE Int. Symp. Circuits and Systems (ISCAS)*, New Orleans, LA, pp. 109-112, May 2007.

M. Seo, S. Joshi and I. A. Young, "A blind calibration technique for memory errors in amplifier-sharing pipelined ADCs," *IEEE Int. Symp. Circuits and Systems (ISCAS)*, New Orleans, LA, pp. 3610-3613, May 2007.

M. Seo, M. Rodwell and U. Madhow, "Generalized blind mismatch correction for two-channel time-interleaved A-to-D converters," *IEEE Int. Conf. Acoustics, Speech and Signal Processing (ICASSP)*, Honolulu, HI, pp. 1505-1508, Apr. 2007.

M. Seo, M. Rodwell and U. Madhow, "A low computation adaptive blind correction for time-interleaved ADC's," *IEEE 49th Int. Midwest Symp. Circuits and Systems (MWSCAS)*, Puerto Rico, pp. 292-296, Aug. 2006

C. Carta, M. Seo and M. Rodwell, "A mixed-signal row/column architecture for very large monolithic mm-Wave phased arrays," *IEEE Lester Eastman Conference on High Performance Devices*, Cornell University, NY, Aug. 2006.

M. Seo, M. Rodwell and U. Madhow, "Blind correction of gain and timing mismatches for a two-channel time-interleaved analog-to-digital converter: Experimental verification," *IEEE Int. Symp. Circuits and Systems (ISCAS)*, Greece, pp. 3394-3397, May 2006.

M. Seo, M. Rodwell and U. Madhow, "Blind correction of gain and timing mismatches for a two-channel time-interleaved analog-to-digital converter," *39th Asilomar Conference on Signals, Systems, and Computers*, Pacific Grove, CA, pp. 1121-1125, Oct. 2005.

Z. Griffith, M. Dahlstrom, M. Seo, M. Rodwell, M. Urteaga, R. Pierson, P. Rowell, B. Brar, S. Lee, N. Nguyen, C. Nguyen, "Ultra high frequency static dividers in

a narrow mesa InGaAs/InP DHBT technology," *16th IEEE Int. Conf. Indium Phosphide and Related Materials (IPRM)*, Japan, May 2004

Abstract

Signal Processing/Hardware Co-Design for High-Speed A/D Conversion and Millimeterwave Sensor Nets

Munkyo Seo

Signal processing (S/P) algorithms and hardware (H/W) implementations have been regarded as separate disciplines, so they are typically designed separately. However, for many cutting-edge applications, co-design of signal processing and hardware is the only option for attaining system-level goals regarding speed, power consumption or complexity. This dissertation presents the outcome of two research projects based on co-design approach: High-speed A/D conversion system, and millimeter-wave sensor network.

First, the theory and experiment of time-interleaved A/D converters (TIADC), enhanced by adaptive signal processing, is presented. TIADC can, in principle, maximize speed-resolution product by using multiple parallel A/D converters. However, H/W mismatches between TIADC channels seriously degrade TIADC noise performance. It is shown that digital S/P can compensate for such H/W errors with 20–50 dB improvements in SNR. Various scenarios are considered: "blind" error estimation as well as "training-based" calibration, full-digital S/P as well as mixed-domain S/P. Key enablers in S/P techniques are weighted least-

squares (for training methods), parameterized filter bank (for modeling), and cyclostationary spectral analysis (for blind methods).

Second, a new approach to a wireless sensor network (WSN) is demonstrated by an experimental 60 GHz prototype, which can collect data from sensors and identify their 3-D locations. The proposed approach draws upon an imaging principle, interpreting sensors as a reflective information source, or a "pixel." Key motivation is to strip down the complexity of sensor H/W, as this favors very large-scale networks. The system, instead, exploits millimeterwave frequencies and S/P techniques to compensate for simplistic sensor H/W. The design of a prototype collector and passive sensors are discussed. Results from indoor radio experiments will be presented.

Professor Mark Rodwell
Dissertation Committee Chair

Contents

List of Figures

Chapter 1

Introduction

This dissertation is the outcome of two research projects: high-resolution time-interleaved A/D converter (TIADC) and millimeter-wave wireless sensor network (WSN). The research goal was to identify and address key challenges in ultra high-performance A/D converters and large-scale wireless sensor networks (WSN), respectively. The nature of these research programs required simultaneous consideration of hardware design and signal processing algorithms from the system level viewpoint. In the first project, deterministic/statistical signal processing techniques are used to compensate for hardware imperfections in TIADCs. In the second project, centralization of sophisticated signal processing at collector nodes, as well as the exploitation of millimeterwave frequencies, enables drastic simplifications of sensor hardware.

For many cutting-edge applications, as these two projects illustrate, co-design of signal processing and hardware is the only option for attaining system-level goals regarding speed, power consumption or complexity [1].

This chapter provides a brief introduction for each project.

1.1 Time-Interleaved ADCs (TIADC)

Time-interleaved A/D conversion provides a scalable way of increasing sampling rate. By using multiple parallel A/D converters (ADC), the overall sampling rate is proportional to the number of ADC channels. TIADCs find their applications in high-speed communication, instrumentation, radar, etc. It has been well known, however, that the spectral performance of TIADCs is seriously degraded by hardware mismatches between ADC channels. These mismatch errors effectively modulate the input signal, creating a distortion (or *aliasing*, in the frequency domain). Therefore, compensation of TIADC mismatches has been the subject of much research.

Most previously known correction methods start with two simplifying assumptions. First, TIADC mismatches can be represented by a few parameters, i.e. gain, sampling time and offset. Second, these mismatch parameters are a priori known or can be measured with desired accuracy. While certainly restrictive, this sim-

plified approach has been successful for low to medium resolution applications (e.g. SNR $<$ 30–50 dB). While a growing number of applications require higher level of performance (e.g. SNR $>$ 70–80 dB), the traditional parametric approach can not deliver the required level of mismatch suppression. The failure of traditional approaches for high-resolution applications is partly due to the starting assumptions abovementioned, and partly due to the lack of clear understanding of TIADC operation, and hence its modeling thereof.

The present thesis work takes *generalized* modeling approaches for significantly higher TIADC performance. Each of TIADC channels are modeled as a general linear time-invariant (LTI) system, and this forms a basis of accurate mismatch correction.

First, a training-based estimation/correction method is developed based on the generalized mismatch model. Signal processing techniques are tightly coupled to TIADC model, and this approach resulted in record spur-free dynamic range performance (SFDR) of 80–90 dB (actual measurement was limited by quantization noise). While capable of meeting performance level of most high-end applications, training-signal based calibration methods are subject to detuning due to temperature change, parts aging, etc. This requires periodic re-calibration.

The second contribution is the proposal and demonstration of "blind" mismatch estimation/correction. In this correction method, we do not need to apply

a prior known calibration signal to the TIADC. Instead, mismatch estimation is continuously, and adaptively carried out by only observing the TIADC output. "Blind" mismatch correction can, therefore, eliminate the need of re-calibration, which is a significant benefit for certain applications where TIADC cannot stop A/D conversion just for calibration. The principle of the proposed blind method makes extensive use of techniques from statistical signal processing.

Last, a novel mixed-domain approach to the TIADC mismatch correction is proposed. In this method, mismatch errors are detected in the digital domain, but their correction is partly done in the analog domain by directly tuning the sampling clock. The proposed mixed-domain approach provides blind error correction with minimal computational complexity.

1.2 Wireless Sensor Networks

Recently, there have been significant research and development efforts on sensor networks. A sensor network is a collection of devices with limited sensing, computation capability that collaborate to observe the environment in which they are placed [2]. Many applications can benefit from such a sensor network: environmental monitoring [3], geological studies [4], wildlife research, seismic activity detection [5], remote sensing, battle field surveillance, border policing, smart

homes [6], etc. More exotic applications are also possible such as planetary exploration, body-area network, etc.

Conventional wireless sensor networks rely on *multi-hop* based communication, where neighboring sensors communicate with each other, to reach the final information collector [7, 8]. The information transfer tends to be robust in this way, since the mesh-like network structure lends itself tolerant to individual sensor failure. In most applications, a sensor node must provide its own location information, as well as its sensing data. Pre-programming the sensor node with a fixed ID code can be a simple localization method, but this is not applicable to a mobile network, and also inconvenient for a large-scale network. A GPS receiver can provide precise location information. Various ranging techniques using radio waves or acoustic waves can also be employed for self-consistent location acquisition of a network of sensors [9].

The primary disadvantage of the conventional approach mentioned above is that it does not easily scale into large-scale networks [10]. The information transfer becomes inefficient as the network size grows, especially when the final collector is far away (e.g. satellite). Ad-hoc networking with neighboring nodes needs a certain protocol stack, as well as RF transceivers, and this increases the complexity of sensor hardware. Location devices for each sensor also results in complex sensor

hardware. As the sensor hardware becomes more complex, its power consumption will also increase, in general, reducing its battery life.

In this thesis, we propose a novel approach to the wireless sensor network, in collaboration with Bharath Ananthasubramaniam and Professor Upamanyu Madhow, ECE Department, UCSB. The key motivation is to drastically simplify sensor hardware to retain minimal functionality. The system, instead, exploits millimeterwave frequencies and signal processing techniques at the collector side to compensate for simplistic sensor hardware. The proposed approach draws upon an imaging principle, interpreting sensors as a reflective information source, or a "pixel." In the proposed architecture, sensor nodes need not communicate with each other, and their location can be a priori unknown. The 60-GHz prototype system consists of collector transceiver, mechanically steerable high-gain antenna, signal-processing algorithms and passive sensors. Results from indoor radio experiment are presented.

Chapter 2

Mismatch Correction for TIADCs: Training-based Method

In this chapter, a training-based calibration method for a TIADC is presented with comprehensive mismatch modeling approach [11]. First, a generalized linear model of TIADC is developed in Section 2.2. Next, an intuitive explanation of aliasing-error generation is given in terms of sub-converter transfer functions in Section 2.3. In Section 2.4, the characterization of sub-converter transfer functions is discussed along with practical concerns. Section 2.5 presents a novel design method of correction finite-impulse response (FIR) filters which, unlike the previous techniques, fully exploits the stopband structure of input analog circuitry. Finally, experimental results and conclusion are given in Section 2.6 and Section 2.7, respectively.

2.1 Introduction

In order to increase the sampling rate of an analog-to-digital converter (ADC) beyond a certain process technology limit, the use of a time-interleaved analog-to-digital converter (TIADC) has been proposed [12–34]. A TIADC has a parallel structure where a number of ADCs independently sample the input signal. The input analog signal is successively sampled by each ADC in a cyclic manner, and the digital output is similarly taken from each ADC to reconstruct the signal stream in digital form. The overall sampling rate is, therefore, multiplied by the number of ADCs. A TIADC finds its application in electronic systems such as radar, direct digital receivers, base-station receivers, and high-speed instrumentation, as well as opto-electric systems including photonic ADCs [15–18].

A TIADC performs high-throughput analog-to-digital (A/D) conversion with no degradation in spectral purity if all ADCs have identical electrical characteristics (e.g., gain, sampling time, input bandwidth, dc offset, etc.). In practice, however, various electrical mismatches are inevitable, which periodically modulate the input signal. The array's spurious-free dynamic range (SFDR) is then reduced due to spurious sidebands generated by this modulation.

Therefore, to achieve the highest SFDR feasible, channel mismatches must be eliminated or calibrated by using either analog circuitry [19, 20, 22–24] or digital

signal processing [25–31]. Digital correction is preferred due to its reliability and flexibility. Continued scaling of process technologies also make digital processing increasingly inexpensive.

Traditionally, TIADC mismatch correction has been mostly attempted in terms of several frequency-independent parameters such as gain, sampling time, and offset mismatches. This parametric approach is easily implemented, and is adequate for low-to-moderate resolutions. In high-resolution data conversion, however, spectral purity is easily compromised by even slight channel mismatches because of the low quantization noise floor. For example, 80 dB of SFDR requires approximately 0.01% of residual channel mismatches [18]. Parametric correction is, in general, not able to achieve this level of mismatch correction over a wide frequency range and, therefore, comprehensive (i.e., frequency dependent) mismatch correction is necessary. Very high-speed time-interleaved A/D conversion may also require comprehensive mismatch correction due to differences between channels in the high-frequency transfer functions of the input analog circuitry.

The application of hybrid filter banks (HFBs) to TIADC has been proposed to attenuate channel mismatches [32, 35–37]. In this architecture, a set of analog filters split the input signal into separate frequency bands in either discrete [38] or continuous [35,37,39] time. Outputs from sub-converters are combined through a digital filter bank. Although the performance of HFB converters is less sensitive

to mismatch errors than conventional TIADCs, the need of accurate analog filters restricts their practical use.

Recently, an important observation has been made by Velazquez and Velazquez [36]: analog filters at the input are not necessary given a properly designed digital filter bank. This suggests a practical way of mismatch correction for high-performance TIADCs, i.e., comprehensive error correction only by digital post-processing. Commercial TIADC products, with 12-bit resolution and 400–500 Msamples/s (MSPS) conversion rate, are also developed based on his approach [40, 41].

In this chapter, a novel comprehensive mismatch correction method is presented, as well as its experimental verification, which, unlike the previous techniques, fully exploits the stopband structure of input analog circuitry for more efficient correction. In designing correction finite-impulse response (FIR) filters, aliasing spurs due to the sub-converter mismatches are individually controlled within the computational framework of the weighted least squares (WLS).

2.2 Linear Model of TIADC

Figure 2.1(a) shows a four-channel TIADC configuration. Each channel converts analog input signal every $4T_s$ with an appropriate delay so that the aggregate

sampling rate is f_s (=$1/T_s$). The bandwidth of the input signal has to be smaller than $f_s/2$ to avoid aliasing. Although operation in any Nyquist-zone is possible as long as the sample-and-hold (S/H) circuitry has sufficient bandwidth, we assume, for simplicity, that the input signal is confined within the first Nyquist-zone, i.e., from dc to $f_s/2$. It is noted that, for M-channel interleaved operation, the S/H blocks must have M-times wider bandwidth than is required for single-channel conversion at f_s/M, i.e., their input bandwidth has to be equal to or greater than $f_s/2$. M-channel interleaved A/D conversion also requires the sampling clock to have M-fold higher timing stability (i.e., lower phase noise).

The assumption of a bandlimited input simplifies notation by allowing discrete-time representation of all signals including the ADC input. Although $H(e^{j2\pi fT_s})$ is the conventional notation for a discrete-time frequency spectrum with period f_s, we instead use $H(f)$ throughout the paper for readability. All S/H and ADC blocks are assumed to be linear and have zero offset. Channel offset is independently measured during calibration and is subsequently digitally subtracted from each ADC output. Time-invariance (or shift-invariance) is assumed for all linear systems. Assuming that the resolution of the individual ADC's is high, we neglect their quantization effects.

In Figure 2.1(a), two typical sources of mismatches are shown: G_k's and Δt_k's for A/D conversion gain and systematic timing deviation from a nominal sampling

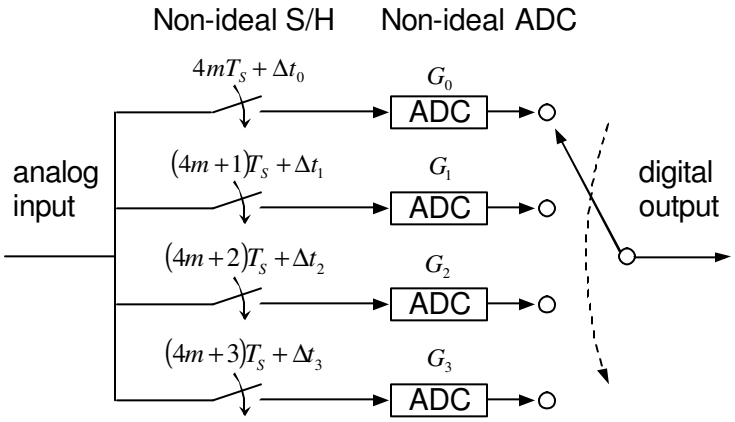

(a) Actual system with two representative linear imperfections (i.e., unequal sampling time deviation and ADC gain)

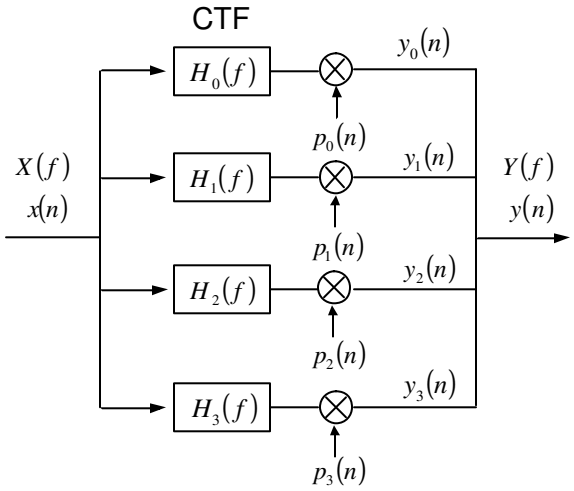

(b) General linear model with channel-transfer-functions (CTF). All the linear distortions in each channel are lumped into a single CTF

Figure 2.1: A four-channel time-interleaved ADC system

point, respectively. As we will show later with experimental data, G_k and Δt_k are not sufficient to describe all significant TIADC errors. For example, S/H blocks may have different 3-dB bandwidth, and the adjacent channels may have unequal crosstalk due to the integrated-circuit (IC) interconnect environment or due to a finite S/H off-state isolation. Small variations will exist between channels in their mid-band frequency response due to power supply and ground impedance and standing waves on interconnects.

A TIADC system with all these linear imperfections can be conveniently modeled with a set of equivalent channel-transfer-functions (CTF) followed by a multiplication by an impulse train, as can be seen in Figure 2.1(b),

$$p_k(n) = \sum_{m=-\infty}^{\infty} \delta\left(n - (mM + k)\right), \quad k = 0, 1, ..., M-1$$

whose period is equal to M, the number of TIADC channels. $\delta(n)$ is the delta function. With only gain and timing error, for example, a CTF will have the form $H_k(f) = G_k e^{-j2\pi f \Delta t_k}$. A CTF may actually include *any linear* distortion pertaining to each channel from S/H input to ADC output. It may also incorporate preceding linear systems common to all channels (e.g., an anti-aliasing filter). It is noted that CTF's are not necessarily causal, especially when there is a sampling time mismatch. This comes from the fact that a bandlimited signal at any instance can be represented as a weighted sum of nominal sample values, both in the past and future [42].

2.3 Generation of Aliasing Error

Aliasing in the presence of individual gain, timing, and offset mismatches has been extensively discussed in the literature [12,14,21,32–35,37]. This section gives more general description in terms of CTF. The TIADC linear model in Figure 2.1(b) suggests each channel output is a *filtered* (by a CTF) and *aliased* (by an impulse train) version of the input spectrum. It can be shown that the kth channel output is written as

$$Y_k(f) = \frac{1}{M}\sum_{m=0}^{M-1} e^{-j2\pi k\frac{m}{M}} X\left(f - \frac{m}{M}f_s\right) H_k\left(f - \frac{m}{M}f_s\right), \quad k = 0, 1, ..., M-1 \quad (2.1)$$

where $X(f)$ is the Fourier transform of the input signal $x(n)$, and $H_k(f)$ is the kth channel CTF. The first term with $m = 0$ corresponds to a desired signal component, while terms with $m = 1, 2, ..., M-1$ are frequency-shifted versions of the input spectrum. When all channel outputs are combined to yield a TIADC output $Y(f)$, these frequency-translated versions of the input spectrum are cancelled if all CTF's are the same. In the presence of CTF mismatches, however, cancellation is imperfect, producing aliasing error, as will be discussed next.

The final output of the four-channel TIADC, $Y(f)$ in Figure 2.1(b), is obtained by summing all channel outputs

$$Y(f) = \begin{pmatrix} c_0(f)X(f) \\ +c_1(f-\frac{1}{4}f_s)X(f-\frac{1}{4}f_s) \\ +c_2(f-\frac{2}{4}f_s)X(f-\frac{2}{4}f_s) \\ +c_3(f-\frac{3}{4}f_s)X(f-\frac{3}{4}f_s) \end{pmatrix}, \tag{2.2}$$

where $c_m(f)$'s are defined as

$$\begin{aligned} c_0(f) &= \tfrac{1}{4}\left(H_0(f)+H_1(f)+H_2(f)+H_3(f)\right), \\ c_1(f) &= \tfrac{1}{4}\left(H_0(f)-jH_1(f)-H_2(f)+jH_3(f)\right), \\ c_2(f) &= \tfrac{1}{4}\left(H_0(f)-H_1(f)+H_2(f)-H_3(f)\right), \\ c_3(f) &= \tfrac{1}{4}\left(H_0(f)+jH_1(f)-H_2(f)-jH_3(f)\right). \end{aligned} \tag{2.3}$$

Equation (2.2) shows the TIADC output spectrum generally has both the desired signal and a frequency-shifted aliasing component, each with a corresponding gain defined in (2.3). Therefore, $c_m(f)$ is an effective conversion gain from an input signal at f to a frequency-shifted output at $f+(m/M)f_s$. Throughout this paper, $c_0(f)$ will be referred to as *signal conversion gain*, while $c_{m\neq 0}(f)$ will be referred to as *noise conversion gain*.

It is interesting to note from (2.3) that the set of conversion gain $\{c_0(f),\ c_1(f),\ c_2(f),\ c_3(f)\}$ can be regarded as a four-point discrete Fourier transform (DFT) of the CTF sequence $\{H_0(f),\ H_1(f),\ H_2(f),\ H_3(f)\}$. If all CTFs are the same

(i.e., no mismatch), then all DFT coefficients, except $c_0(f)$, cancel, resulting in zero aliasing error. In this case, SFDR is, therefore, not limited by aliasing spurs. With the presence of channel mismatches, however, $c_{m\neq 0}(f)$ is nonzero, in general, and SFDR is limited by the aliasing spurs whose magnitude is proportional to the corresponding noise conversion gain $c_{m\neq 0}(f)$. Figure 2.2 graphically illustrates how CTF mismatch generates spurious signals on the TIADC output spectrum.

It is noted in Figure 2.2(b) that the positive and negative frequency components of the input spectrum each experiences different conversion gains. For example, assume a real-valued input sinusoid at f_{in}, which has two complex exponentials at frequencies f_{in} and $-f_{in}$ (or, equivalently, $f_{in}+f_s$). The positive-frequency tone at f_{in} passes through the CTFs $\{H_0(f_{in}),\ H_1(f_{in}),\ H_2(f_{in}),\ H_3(f_{in})\}$, and, by DFT analysis, we obtain the conversion gain $\{c_0(f_{in}),\ c_1(f_{in}),\ c_2(f_{in}),\ c_3(f_{in})\}$ with corresponding aliasing spurs at $\{f_{in},\ f_{in}+\frac{1}{4}f_s,\ f_{in}+\frac{2}{4}f_s,\ f_{in}+\frac{3}{4}f_s\}$. On the other hand, the image tone at $-f_{in}$ experiences the channel gain $\{H_0(-f_{in}),\ H_1(-f_{in}),\ H_2(-f_{in}),\ H_3(-f_{in})\}$, which is equal to $\{H_0^*(f_{in}),\ H_1^*(f_{in}),\ H_2^*(f_{in}),\ H_3^*(f_{in})\}$ where $(\cdot)^*$ denotes the complex conjugate. According to the properties of DFT [42], the resulting conversion gain is $\{c_0^*(f_{in}),\ c_3^*(f_{in}),\ c_2^*(f_{in}),\ c_1^*(f_{in})\}$ with output spurs at $\{-f_{in},\ -f_{in}+\frac{1}{4}f_s,\ -f_{in}+\frac{2}{4}f_s,\ -f_{in}+\frac{3}{4}f_s\}$.

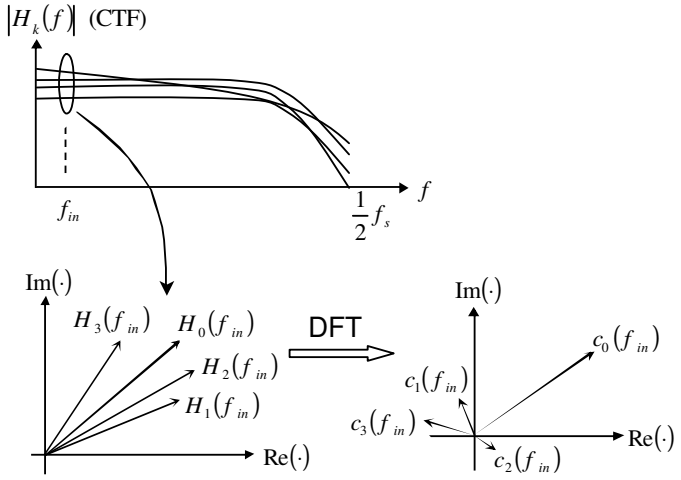

(a) In general, with channel mismatches, each CTF is a different function of frequency. CTF's and their DFT coefficients at f_{in} are plotted on a complex plane. It is seen $c_{m\neq 0}(f_{in})$ are nonzero vectors due to the CTF mismatch at .

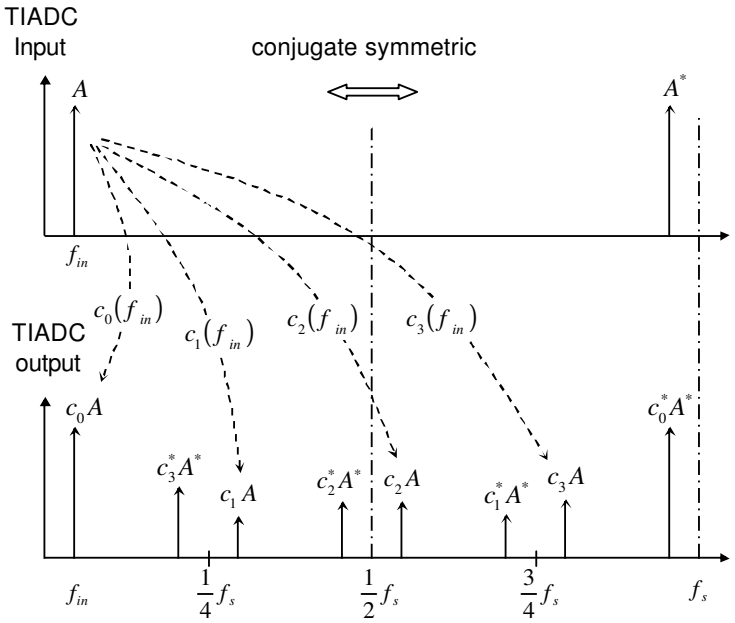

(b) Input and output spectrum with a real-valued sinusoid at f_{in}. The DFT coefficients of CTF play the role of conversion gain from an input tone to each output spectral line. Note that spurious tones reduce the maximum SFDR achievable.

Figure 2.2: Illustration of aliasing-spur generation mechanism

In summary, for an M-channel TIADC, with a real-valued input sinusoid at f_{in}, spurious tones due to the CTF mismatch are generated at

$$f_{\text{CTF mismatch}} = \pm f_{in} + \frac{m}{M} f_s, \quad m = 1, 2, ..., M-1. \tag{2.4}$$

On the other hand, the mismatch in channel dc offset produces error tones at the frequencies [34]

$$f_{\text{offset mismatch}} = \frac{m}{M} f_s, \quad m = 1, 2, ..., M-1. \tag{2.5}$$

It should be noted that offset mismatch does not modulate the input signal, but always produces spurs at fixed frequencies.

2.4 Characterization of CTF

The CTF can be characterized at a single frequency by first applying a sinusoid with known frequency at the TIADC input, and then measuring the individual channel outputs. For a full characterization over a frequency range of interest, either a series of single-frequency tests must be performed or a carefully designed wide-band signal (e.g., a frequency-domain comb signal [35]) is required. The work presented in this thesis is based on a series of single-frequency measurements.

Consider a single sinusoid excitation. If we consider only the signal part (i.e., the output spectral line at the input frequency) from each channel output given

by (2.1), then $Y_k(f) = (1/M)X(f)H_k(f)$. Hence, knowledge of the magnitude and phase of the input sinusoid allows unique determination of the value of the CTF at the test frequency. In order to identify the signal part, frequency-shifted spectra should not fall into the same frequency bin with the signal tone. It can be shown from (2.4) and (2.5) that the input signal frequency should satisfy $f_{test} \neq (m/2M)f_s$ and $f_{test} \neq (m/M)f_s$, where $m = 1, 2, ..., M-1$. These conditions can be met by a careful selection of test frequencies. For example, setting f_{test} to an integer multiple of $(1/P)f_s$, and making $2M$ and P relatively prime (i.e., have 1 as the only common factor) guarantees the signal tone is not ruined by mismatch spurs. In the case where the test signal generator has significant harmonic contents, care has to be taken to avoid aliasing due to harmonics folded down to the first Nyquist zone. In some cases, bandpass filtering of the signal generator may provide enough attenuation. Alternatively, a certain set of calibration frequencies may be discarded. On the other hand, uncorrelated noise, such as phase noise, quantization noise, or wide-band white noise can be averaged out by taking a long acquisition time on the channel outputs.

The set of test frequencies should span at least the frequency range of interest (i.e., the passband of the input analog circuitry or the entire Nyquist zone if all-pass). The frequencies should be dense enough to accurately characterize channel mismatches. The value of CTF between measurement points, if needed in

correction FIR filter design, may be estimated by interpolation [42]. It is noted, however, there is no practical substitute for an initial pilot characterization with a sufficiently large number of test frequencies. The number of test frequencies may be kept minimal once CTFs have been accurately characterized. In practice, it is convenient to normalize a CTF with respect to an appropriately chosen reference (e.g., first-channel gain [35] or averaged CTF across channels). This is more practical than characterizing input sinusoids using an external amplitude and phase reference. Linear gain and phase distortion information, which is common to all channels in this case, may be lost during normalization. However, channel mismatch information, which is crucial to the SFDR performance of TIADC and, hence, also to the correction FIR filter design, is still preserved.

2.5 Design of Correction FIR Filters

Once CTFs are measured, digital filters can be designed to correct mismatch errors. In Figure 2.3, a length-N FIR filter is cascaded for every channel, and the filter outputs are then combined to form $\tilde{X}(f)$, the error-corrected output. Our goal is to make a faithfully reconstructed version of the input $X(f)$. For an M-channel TIADC, $\tilde{X}(f)$ can be written, similarly as in (2.2), as a weighted sum

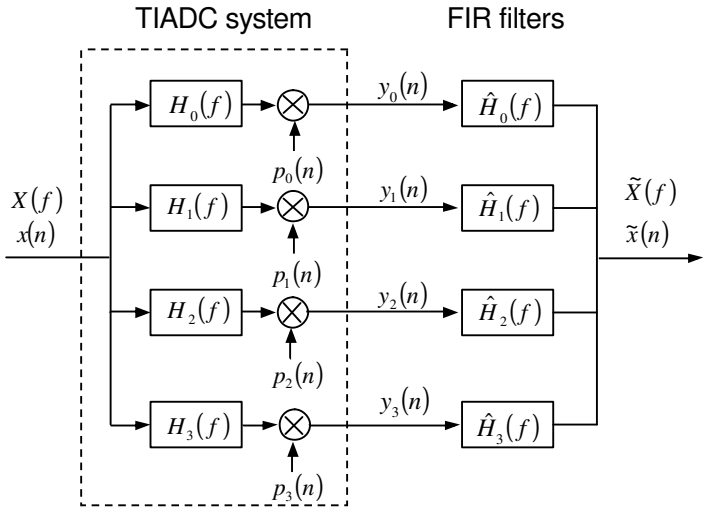

Figure 2.3: TIADC cascaded by a set of mismatch-correction FIR filters.

of frequency-shifted input signal spectrum

$$\tilde{X}(f) = \sum_{m=0}^{M-1} \tilde{c}_m \left(f - \frac{m}{M} f_s\right) X\left(f - \frac{m}{M} f_s\right). \tag{2.6}$$

The conversion gain after correction, $\tilde{c}_m(f)$, is now a function of FIR filter coefficients as follows:

$$\begin{aligned} \tilde{c}_m(f) &= \frac{1}{M} \sum_{k=0}^{M-1} e^{-j2\pi k \frac{m}{M}} H_k(f) \hat{H}_k\left(f + \frac{m}{M} f_s\right) \\ &= \frac{1}{M} \sum_{k=0}^{M-1} \sum_{n=0}^{N-1} e^{-j2\pi k \frac{m}{M}} e^{-j2\pi n\left(\frac{f}{f_s} + \frac{m}{M}\right)} H_k(f) \hat{h}_k(n). \end{aligned} \tag{2.7}$$

In (2.7), $\hat{h}_k(n)$ and $\hat{H}_k(f)$ are the impulse and frequency response of the kth channel length-N FIR filter, respectively. For perfect reconstruction of the input signal, $\hat{h}_k(n)$ needs to be designed so that $\tilde{c}_0(f)$ and $\tilde{c}_{m\neq 0}(f)$ are as close to an ideal time-delay system and zero as possible, respectively. For aliasing-free re-

construction, on the other hand, the only strict requirement is to make $\tilde{c}_{m\neq 0}(f)$ zero across the entire frequency range. In this case, $\tilde{c}_0(f)$ may introduce additional linear distortion as well as time delay. Mismatch spurs are still suppressed, however, and the spectral purity is not compromised by them. Therefore, both reconstruction strategies are equally effective in achieving a high SFDR as long as the linear distortion due to $\tilde{c}_0(f)$ is tolerable. In certain TIADC applications, where subsequent digital filtering is provided, the residual linear distortion can be further equalized.

There are MN unknown FIR filter coefficients, $\hat{h}_k(n)$'s, in (2.7), and these can be uniquely determined given a proper number of desired values of $\tilde{c}_m(f)$. One possible method is to solve the system of MN equations with an equal number of unknowns by specifying the desired conversion gain for $m = 0, 1, ..., M-1$ over L discrete frequencies [35, 36, 39]. The proposed design approach based on WLS, however, fully exploits the stopband structure, thus, providing greater flexibility and a useful tradeoff in signal reconstruction.

2.5.1 WLS Formulation

First, form a system of conversion gain equations, for both signal and noise, by equating the right-hand side of (2.7) to a desired gain value over L discrete frequencies. With the incorporation of equation-wise weighting, the entire system

of equations can be written in a standard matrix-vector form

$$\sqrt{\mathbf{W}}\mathbf{A}\hat{\mathbf{H}} = \sqrt{\mathbf{W}}\mathbf{D}, \tag{2.8}$$

where each matrix or vector has a substructure as follows:

$$\begin{aligned}
\mathbf{A} &= \begin{pmatrix} \mathbf{a_{0,0}} & \mathbf{a_{0,1}} & \cdots & \mathbf{a_{0,M-1}} \\ \mathbf{a_{1,0}} & \mathbf{a_{1,1}} & & \mathbf{a_{1,M-1}} \\ \vdots & & \ddots & \vdots \\ \mathbf{a_{M-1,0}} & \mathbf{a_{M-1,1}} & \cdots & \mathbf{a_{M-1,M-1}} \end{pmatrix}, \\
\sqrt{\mathbf{W}} &= \begin{pmatrix} \sqrt{\mathbf{w_{0,0}}} & \mathbf{0} & \cdots & \mathbf{0} \\ \mathbf{0} & \sqrt{\mathbf{w_{1,1}}} & & \mathbf{0} \\ \vdots & & \ddots & \vdots \\ \mathbf{0} & \mathbf{0} & \cdots & \sqrt{\mathbf{w_{M-1,M-1}}} \end{pmatrix}, \\
\hat{\mathbf{H}} &= \begin{pmatrix} \hat{\mathbf{h}}_\mathbf{0} & \hat{\mathbf{h}}_\mathbf{1} & \cdots & \hat{\mathbf{h}}_\mathbf{M-1} \end{pmatrix}^\mathbf{T}, \\
\mathbf{D} &= \begin{pmatrix} \mathbf{d_0} & \mathbf{0} & \cdots & \mathbf{0} \end{pmatrix}^\mathbf{T}.
\end{aligned} \tag{2.9}$$

where

$$\begin{aligned}
\sqrt{\mathbf{W_m}} &= \text{diag}\left(\sqrt{w_m(f_0)}\ \sqrt{w_m(f_1)}\ \cdots\ \sqrt{w_m(f_{L-1})}\right), \\
[\mathbf{a_{m,k}}]_{l,n} &= \frac{1}{M} e^{-j2\pi k\frac{m}{M}} e^{-j2\pi n\left(\frac{f}{f_s}+\frac{m}{M}\right)} H_k(f_l), \\
\left[\hat{\mathbf{h}}_\mathbf{k}\right]_n &= \hat{h}_k(n), \\
[\mathbf{d_0}]_l &= d(f_l). \\
m, k &= 0, 1, ..., M-1 \ \ (M\text{: the number of channels}) \\
l &= 0, 1, ..., L-1 \ \ (L\text{: the number of evaluation frequencies}) \\
n &= 0, 1, ..., N-1 \ \ (N\text{: FIR filter length})
\end{aligned}$$

In (2.8), $\mathbf{A}$ is an $LM \times NM$, $\sqrt{\mathbf{W}}$ is an $LM \times LM$, $\hat{\mathbf{H}}$ is an $NM \times 1$, and $\mathbf{D}$ is an $LM \times 1$ matrix or row vector. The weighting matrix is represented in a square-root form for convenience. The desired conversion gain is specified by $\mathbf{D}$ (specifically, $\mathbf{d_0}$ and $\mathbf{0}$ for signal and noise conversion gain, respectively). Each conversion gain is evaluated at L discrete frequencies f_0 from to f_{L-1} . The first L equations in (2.8) define the signal conversion gain, and the remaining $(M-1)L$ equations dictate the aliasing noise conversion gain. If $L > N$, which is true, in general, (2.8) is an overdetermined system of equations, and the unique solution in a least square sense is [43]

$$\hat{\mathbf{H}}_\mathbf{WLS} = \left(\mathbf{A^H W A}\right)^{-1} \mathbf{A^H W D}, \tag{2.10}$$

where $(\cdot)^\mathbf{H}$ denotes complex-conjugate transpose. It can be shown that $\hat{\mathbf{H}}_\mathbf{WLS}$ minimizes the *weighted* mean-squared error between the desired conversion gain

$\mathbf{D}$ and actual conversion gain $\mathbf{A}\hat{\mathbf{H}}_{\mathbf{WLS}}$. If $\mathbf{d_0}$ and L test frequencies are chosen such that complex-conjugate symmetry is obeyed, $\hat{\mathbf{H}}_{\mathbf{WLS}}$, obtained by (2.10)), will be real valued. Otherwise, if we explicitly constrain $\hat{\mathbf{H}}$ to be real valued, the optimum solution is $\hat{\mathbf{H}}_{\mathbf{WLS}} = \left(\mathbf{Re}(\mathbf{A^H W A})\right)^{-1} \mathbf{Re}\left(\mathbf{A^H W D}\right)$. Two design options are of interest: unweighted and weighted design.

2.5.2 Unweighted Filter Design

In unweighted design, the weighting matrix is an identity matrix so that no equation in (2.8) is weighted heavier or lighter than others. The only parameter that controls the quality of error correction is N, the FIR filter length. Due to the *Gibbs* phenomenon [42, 44], the conversion gains realized by the resulting FIR filters usually have significant ripples. Ripples in signal conversion gain have a minor effect on SFDR, but ripples in noise conversion gains directly reduce SFDR by generating excessive aliasing spurs, as experimental results will later show. Therefore, in order to remove such ripples, filter coefficients are multiplied by a window function. Unweighted design is simple to use, but lacks flexibility. The designed filter, if multiplied by a window, is not optimal in any sense.

2.5.3 Weighted Filter Design

Weighted design provides more control over mismatch correction, and allows full exploitation of "don't care" frequency bands. In a classical FIR filter design, a "don't care" band (or "transition" band) refers to a frequency region where no desired filtering response is specified [44]. For TIADC mismatch correction, there is another useful observation: aliasing spurs are free to remain uncancelled within "don't care" bands. This additional benefit from "don't care" bands has not been exploited before to the authors' knowledge. All these relaxed requirements are taken into account by assigning zero or very small weights to the corresponding gain equations in (2.8). The resulting set of equations achieves a smaller total mean-squared error with the same number of FIR filter taps, yielding more satisfactory error correction.

In general A/D conversion systems, a bandpass input signal conditioning circuit (e.g., a transformer) introduces both lower and upper cutoff frequencies (f_L and f_H), and we naturally have two "don't care" bands: one in a lower end (dc to f_L) and the other in a higher end (f_H to $f_s/2$). Even without bandpass input circuitry, sampling time mismatches justify the use of a higher-end "don't care" band. In correcting timing mismatches by using FIR filters, there always exists an upper end frequency band where the approximation error is relatively

large [45]. Although this error can be made smaller by using more FIR filter taps, the upper-end band can be advantageously considered a "don't care" one as well.

One may also employ unequal weighting between signal and noise conversion gain equations for a tradeoff between the degree of aliasing-spur cancellation and the amount of residual linear gain-phase distortion. This realizes aliasing-free reconstruction (instead of perfect reconstruction) in a controllable manner.

With the incorporation of all previous considerations, weighting factors can be defined as (See Figure 2.4 for a four-channel example)

$$\begin{aligned} w_0(f) &= \begin{cases} \delta_s, & f \in \{\text{"don't care" band}\} \\ W_s, & \text{otherwise} \end{cases} \\ w_{m\neq 0}(f) &= \begin{cases} \delta_n, & f \text{ or } f + (m/M)f_s \in \{\text{"don't care" band}\} \\ W_n, & \text{otherwise} \end{cases} \end{aligned} \tag{2.11}$$

where $w_0(f)$ and $w_{m\neq 0}(f)$ quantifies the individual contribution of signal and noise conversion gain errors, respectively. It is understood that $W_s \gg \delta_s$ and $W_n \gg \delta_n$.

Weighting strategies for TIADC correction are summarized as:

1. Signal and noise conversion gain may be arbitrarily defined within "don't care" bands.
2. Aliasing spurs may fall into and remain uncancelled within "don't care" bands.
3. The amount of residual linear distortion can be traded off with the degree of aliasing-spur cancellation by adjusting W_n/W_s.

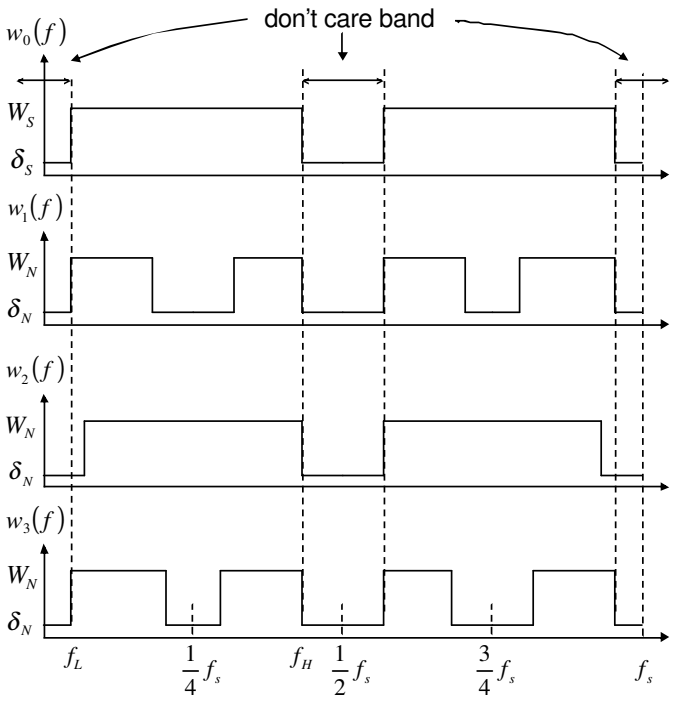

Figure 2.4: Representative weighting scheme for a four-channel TIADC (i.e., illustration of (2.11) when $M = 4$). Input analog circuitry is assumed to have a passband from f_L to f_H. Corresponding stopbands are designated as "don't care", and hence have a very small weighting factor (δ_S or δ_N). Small-weight regions around $(1/4)f_s$ correspond to input frequency bands where aliasing spurs fall into "don't care" bands.

Applicability of each strategy may depend on the application. For example, 1) assumes input signal within the "don't care" bands is sufficiently weak or attenuated so that its aliasing spurs are negligible, and 2) and 3) implies subsequent digital filtering is capable of removing aliasing spurs within "don't care" bands or of equalizing the linear gain-phase distortion common to all channels.

2.6 Experimental Results

To demonstrate the proposed calibration method, a four-channel TIADC prototype was built, and the performance of mismatch correction was evaluated. 400 MSPS of aggregate sampling rate is achieved with 14-bit resolution by interleaving four 14-bit 100 MSPS ADC chips [46]. Figure 2.5(a) shows the experimental configuration. The clock and input test signal are phase-locked to each other, and appropriately filtered to reject harmonics and wide-band white noise. A distribution board consists of power splitters and delay lines to provide four-phase 100 MHz clocks (i.e., 0°, 90°, 180°, and 270°) and an equal phase input signal to the four ADC boards. The digital output is captured by a logic analyzer, and calibration is done on MATLAB. All instruments are controlled by custom software for automatic characterization.

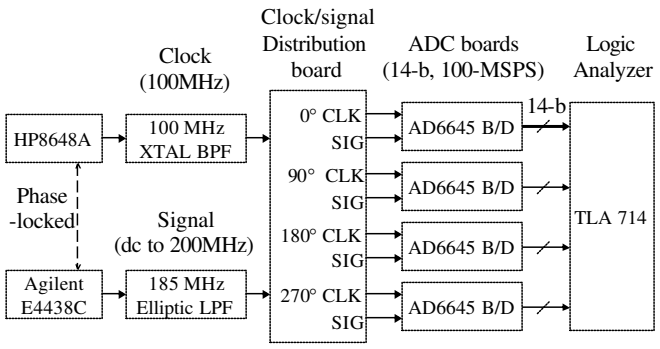

(a) Block diagram

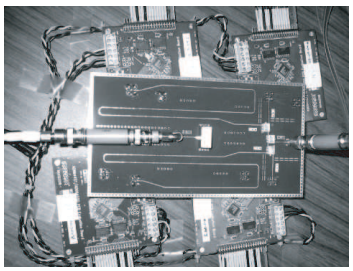

(b) Photograph of a clock/signal distribution board and four ADC boards

Figure 2.5: Experimnetal setup for a 14-bit 400 MSPS TIADC prototype

2.6.1 Data Acquisition and CTF Characterization

For performance evaluation of the proposed correction method, data is acquired at 249 signal frequencies with $(1/500)f_s$ (=0.8 MHz) of spacing. The TIADC is first calibrated using every fourth frequency for CTF characterization: $(1/125)f_s$, $(2/125)f_s$, ..., $(62/125)f_s$. This particular choice of characterization frequencies systematically avoids aliasing due to mismatch spurs since 125 is relatively prime with $2M(= 8)$ (Section 2.4). Although the signal generator's fourth harmonic falls into the same frequency bin as the fundamental tone at $(25/125)f_s$ and $(50/125)f_s$, the antialiasing filter (Figure 2.5(a)) attenuates the fourth harmonic to a negligible level. Channel offset is estimated by averaging the measured

ADC dc output voltage for each run across the whole range of characterization frequencies.

Figure 2.6(a) shows the average magnitude response of the measured CTFs (the output power variation with frequency arising from the signal generator is also lumped into the magnitude response). Figure 2.6(b) and Figure 2.6(c) show the magnitude and phase response after normalization with respect to the average value across channels for each frequency, respectively. The relatively large mismatch at very low frequencies is due to differences between the low-frequency cutoffs of the ADC input transformers (which is approximately 2 MHz). The phase response at midband frequencies approximates a straight line, which suggests timing mismatch is dominant (approximately 1.3%, 0.6%, 0.4%, and 1.1% of T_s). The input antialiasing filter has approximately 50 dB of attenuation near 200 MHz. Random measurement error is, thus, amplified around this frequency, producing a large CTF mismatch near 200 MHz.

Figure 2.7 shows noise conversion gains, which are calculated from DFT analysis of the normalized CTFs. Superposition of all three noise gains in a single decibel plot (Figure 2.7(b)) allows the prediction of uncalibrated SFDR performance to within the magnitude response of a normalization reference (i.e., average CTF values). It is seen in Figure 2.7(a) and Figure 2.7(b) that $c_2(f)$ creates the dominant aliasing spur ($\simeq$ -30 dB at high frequencies). $c_2(f)$ is the highest frequency

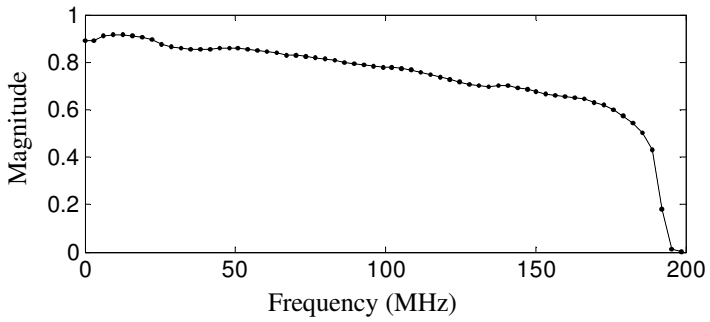

(a) Average magnitude response before normalization. Dots denote measurement points. The anti-aliasing filter creates large attenuation over 185 MHz.

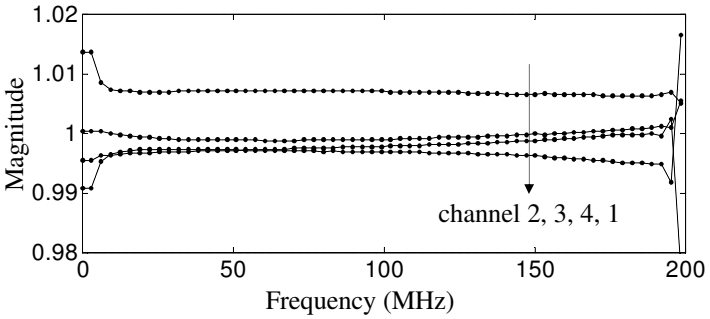

(b) CTF magnitude response after normalization. Dots denote measurement points.

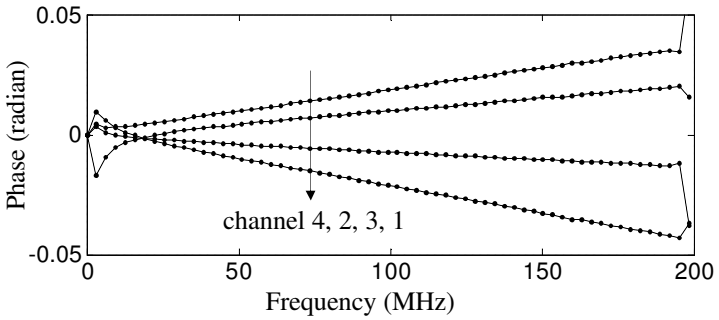

(c) CTF phase response after normalization Dots denote measurement points.

Figure 2.6: Measured CTFs

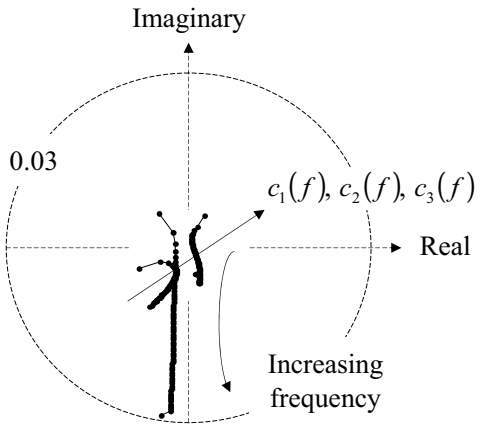

(a) Polar plot of noise conversion gains calculated from the measured CTFs

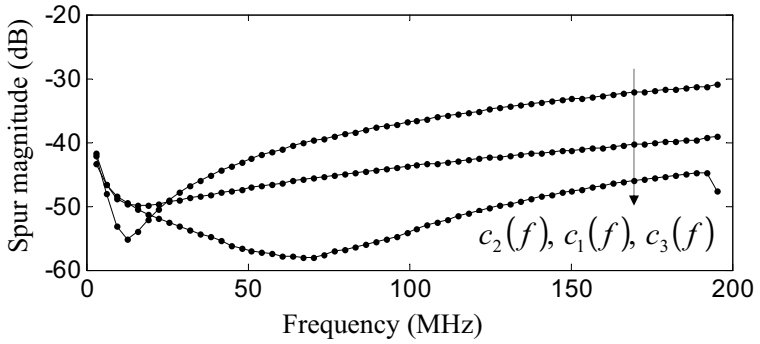

(b) decibel plot of noise conversion gains calculated from the measured CTFs. $c_0(f)$ is always 1 due to the CTF normalization. Note that $c_2(f)$ is the dominant aliasing error except at low frequencies.

Figure 2.7: Measured noise conversion gains.

component obtainable from four-point DFT, and its basis vector is an alternating sequence $\{1, -1, 1, -1\}$. This specific mismatch pattern can be traced back to the clock/signal distribution board where channel 1, 3 (two right ADC boards in Figure 2.5(b)) and channel 2, 4 (two left ADC boards in Figure 2.5(b)) each have identically shaped delay lines.

2.6.2 Mismatch Correction with Unweighted Filter Design

The previously estimated offset is subtracted from a corresponding channel output before comprehensive mismatch correction. The FIR filter coefficients are first obtained by the unweighted least squares method, and then multiplied by a Hanning window to eliminate ripples in the frequency response. It has been found experimentally that 18 bit is sufficient for coefficient quantization with a reasonably small loss of performance (e.g., <1 dB SFDR loss). Figure 2.8(a) and Figure 2.8(b) show the magnitude and phase response of the resulting 41-tap FIR filters. Dotted and solid lines each represent the frequency response before and after applying a Hanning window to the tap coefficients, respectively. It is seen that significant passband ripples are present before windowing, but they are smoothed out after windowing.

Figure 2.9 shows a typical output spectrum before and after mismatch correction. The CTF and offset mismatch spurs (marked as X and O, respectively)

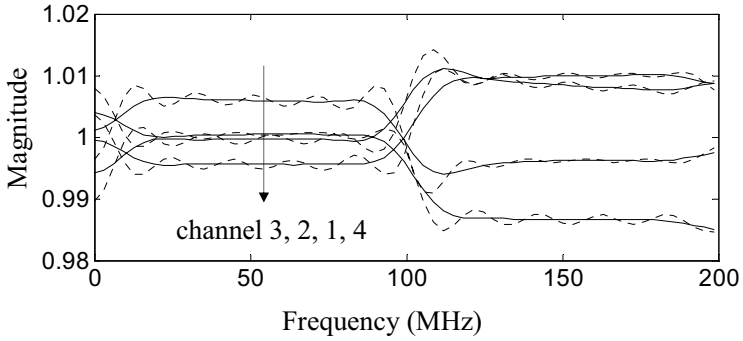

(a) Magnitude response of the correction FIR filters

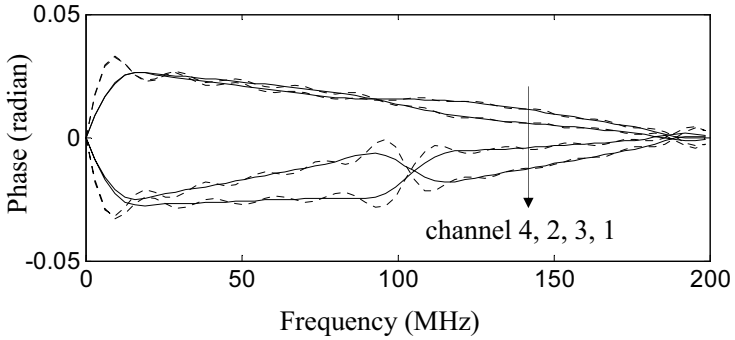

(b) Phase response of the correction FIR filters

Figure 2.8: Frequency response of the correction FIR filters. Unweighted design with 41 taps. The center tap is chosen as the time reference. Dotted and solid lines each represent the frequency response before and after applying Hanning window to the tap coefficients.

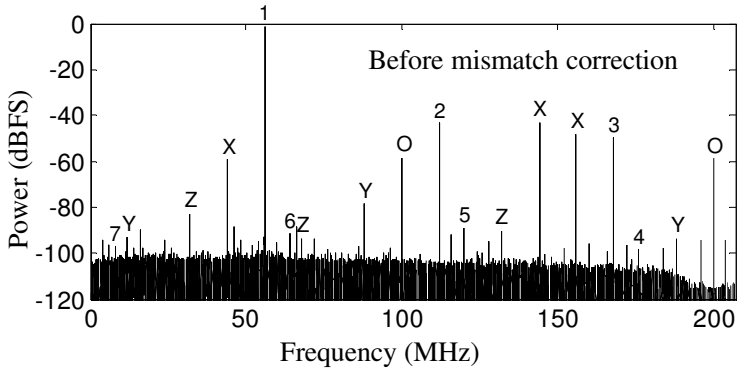

(a) Measured output spectrum before mismatch correction

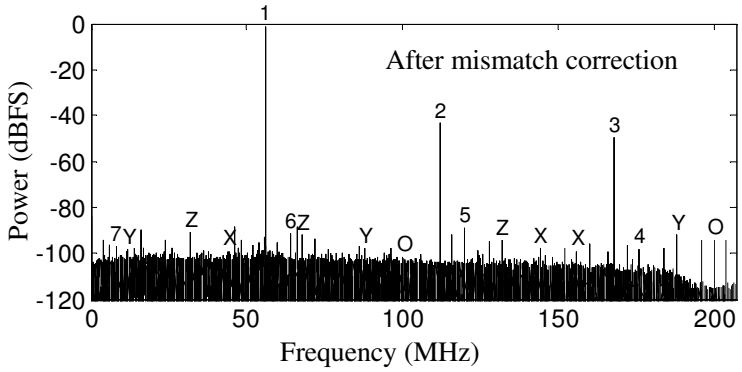

(b) Measured output spectrum after mismatch correction

Figure 2.9: Typical TIADC output spectrum (DFT of 62,000 samples). Correction is done by 21-tap FIR filters (unweighted design). An input sinusoid is applied at -1 dBFS and $(70/500)f_s$ which falls midway between two CTF characterization frequencies. Note that the noise floor reflects the anti-aliasing filter roll-off. The label '1' designates a fundamental tone, '2', '3', , and '7' harmonics of the signal generator, 'X', 'Y', and 'Z' CTF mismatch spurs due to the fundamental, 2nd-, and 3rd-order harmonics, respectively, and the 'O' offset mismatch spurs

are typically suppressed to better than 80 dB below full scale (dBFS). Low-order harmonics from the signal generator are seen to have a significant power level since they are within the passband of the antialiasing filter. It is noted that the signal generator harmonics, as well as a fundamental tone, generate corresponding aliasing spurs. The signal labels, X, Y, and Z in Figure 2.9 represent mismatch spurs at $\pm f_{in} + (m/M)f_s$, $\pm 2f_{in} + (m/M)f_s$, and $\pm 3f_{in} + (m/M)f_s$, respectively.

Figure 2.10 shows the SFDR improvement over a full Nyquist zone by mismatch correction before and after windowing of FIR filter coefficients. Signal generator harmonics up to seventh order are neglected for all SFDR measurements. The inferior SFDR characteristics seen in Figure 2.10(a) compared to those of Figure 2.10(b) is a direct result of excessive ripples in realized noise conversion gains, which are, in turn, due to the ripples in the frequency response of the unwindowed FIR filters. For the remainder of this paper, windowing of tap coefficients is assumed whenever an unweighted FIR design is discussed.

Before correction, the SFDR is limited by mismatch spurs over the entire Nyquist zone. After correction, the percentage of bandwidth where mismatch spurs determine SFDR is only 52%, 27%, and 22% for 21-, 41-, and 61-tap FIR filters, respectively, if we disregard the upper and lower 20 MHz. For the rest of the frequency region, SFDR is typically limited by nonharmonic spurs at $f_{in} \pm$ 10 MHz or higher order (>seventh) harmonics, both coming from the signal generator.

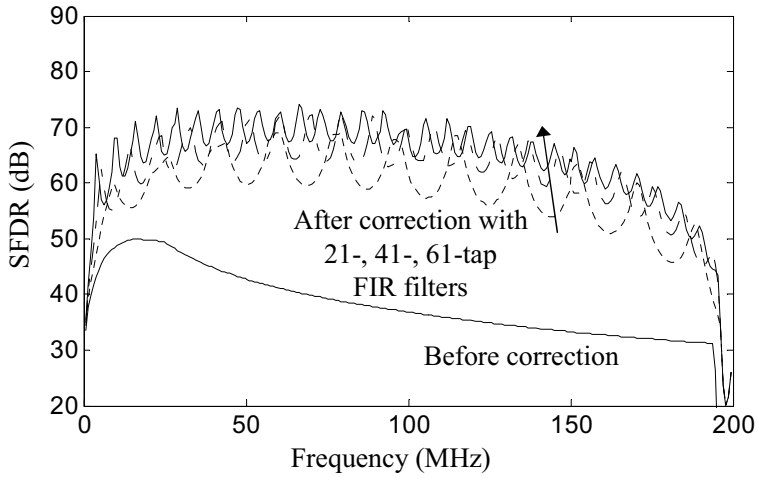

(a) Measured SFDR before applying a Hanning window

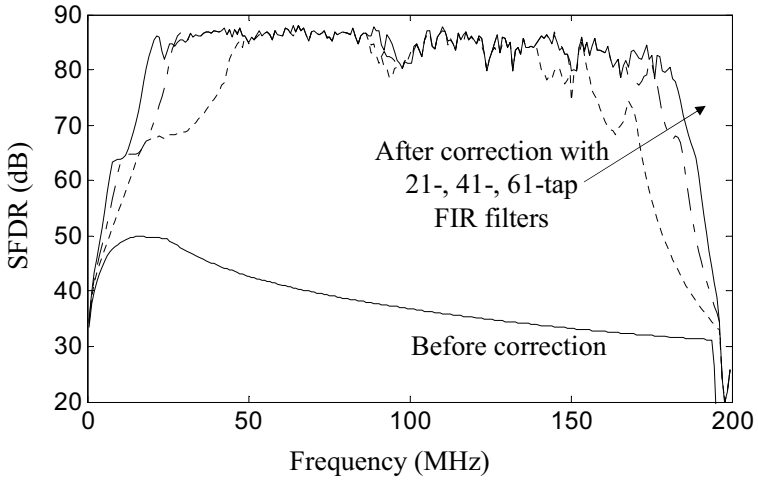

(b) Measured SFDR after applying a Hanning window

Figure 2.10: The effect of windowing on the performance of mismatch correction (unweighted FIR design).

The SFDR drop at both ends of the Nyquist zone originates from phase discontinuities near dc and 200 MHz as seen in Figure 2.6(c). These discontinuities cannot be perfectly equalized by FIR filters and, therefore, approximation error is inevitably introduced. Windowing of the filter coefficients spreads this error in frequency [47] into a narrow frequency region if the FIR filter has many taps. Therefore, a longer FIR filter provides error correction over a wider range of frequencies. The sharp cutoff of antialiasing filter also contributes to a sudden SFDR drop near 200 MHz by quickly attenuating signal power.

The drop in SFDR at low frequencies may be eliminated by making the CTF phase continuous across dc (e.g., by using dc-coupled input analog circuitry or by sharing a single ac-coupled circuitry for all channels). In contrast, the drop in SFDR near $f_s/2$ cannot be completely removed because of the inherent phase discontinuity across the Nyquist frequency in the presence of timing mismatches. Using longer FIR filters, however, extends effective mismatch correction to higher frequencies.

Note the close agreement of uncalibrated SFDR between the measurement (Figure 2.10) and prediction (Figure 2.7(b)).

2.6.3 Unweighted Versus Weighted Filter Design

Figure 2.11 compares weighted and unweighted filter design. The FIR filters have 21 taps in both cases. The unweighted FIR filter design is the same as in Figure 2.10(b). For the weighted design, "don't care" bands are set to the upper and lower 7.6% of Nyquist zone, where systematic SFDR drop occurs. We also choose W_n/W_s to be large in favor of strong cancellation of aliasing spurs rather than perfectly flat gain and phase response. Resulting weighting factors are $W_s = 1$ and $W_n = 3{\cdot}10^5$. As seen in Figure 2.11(a), the weighted design enables a wider frequency range of mismatch correction than the unweighted design with an equal number of FIR filter taps. Spurious signals within the "don't care" bands are ignored in the SFDR calculation for the weighted design. This improvement is obtained, however, by introducing some amount of linear gain-phase distortion into the overall system transfer function from TIADC analog input to corrected digital output. In Figure 2.11(b), the dotted curve is the system gain realized with the unweighted FIR filter design, and is equal to the average CTF, which serves as a reference for CTF normalization. It is seen that the system gain with weighted filter design (solid line in Figure 2.11(b)) has additional linear distortion (<2.5 dB) with respect to the reference. This distortion may be equalized by subsequent digital filtering if needed.

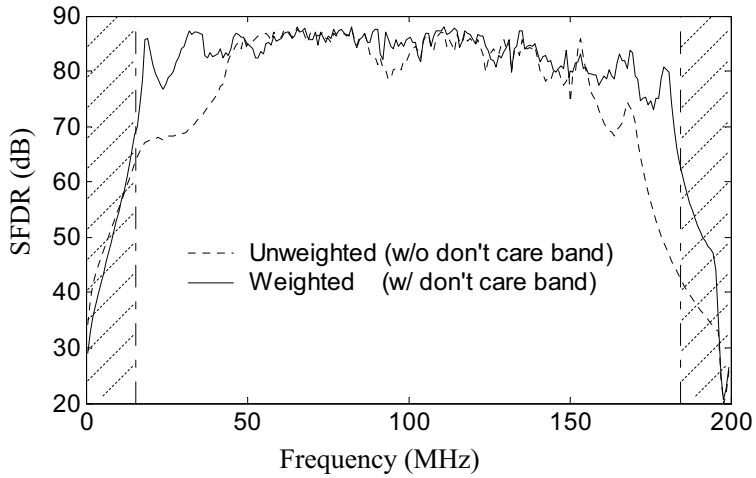

(a) SFDR performance after correction

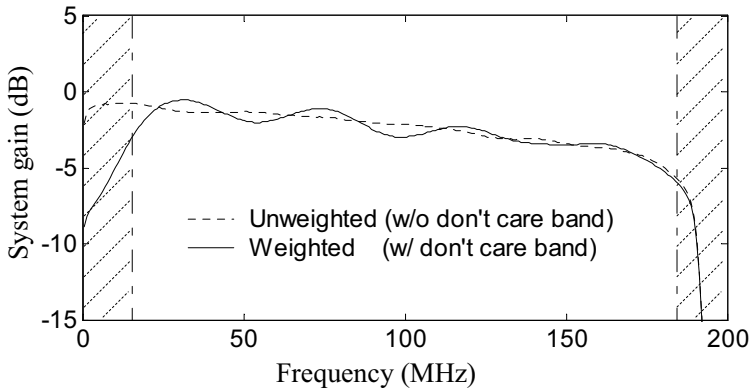

(b) Overall system gain from the TIADC input to corrected output

Figure 2.11: Comparison of unweighted and weighted FIR filter design (21-tap). Shaded regions are "don't care" bands for weighted design.

Although sinusoids are used for the SFDR performance test, it is noted that the proposed calibration method is equally effective with any bandlimited input signal, as this can be represented as a sum of sinusoids within the Nyquist zone. The TIADC system attains linear and time-invariant (LTI) property once mismatches are corrected (this can be seen from (2.6) with $\tilde{c}_{m\neq 0}(f) = 0$).

2.6.4 Frequency-Dependent Versus Frequency-Independent Correction

In this section, traditional frequency-independent calibration is compared with the proposed correction method. From the measured CTFs in Figure 2.6, a best-fit static gain and timing error (G_k and Δt_k in Figure 2.1(a)) are individually extracted for each channel. The upper and lower 20 MHz are not considered during the extraction for a better fit within the passband (20–180 MHz). A new set of CTFs are generated by directly calibrating out the errors, i.e., $H'_k(f) = H_k(f)/G_k e^{-j2\pi f \Delta t_k}$. The magnitude of aliasing spurs are predicted from noise conversion gains, which are obtained by DFT analysis, as discussed in Section 2.3. The resulting SFDR is shown as a solid curve in Figure 2.12, and is typically 10–25 dB worse than the one attained with the comprehensive correction in Figure 2.10 and Figure 2.11. Also shown in Figure 2.12 are the maximum

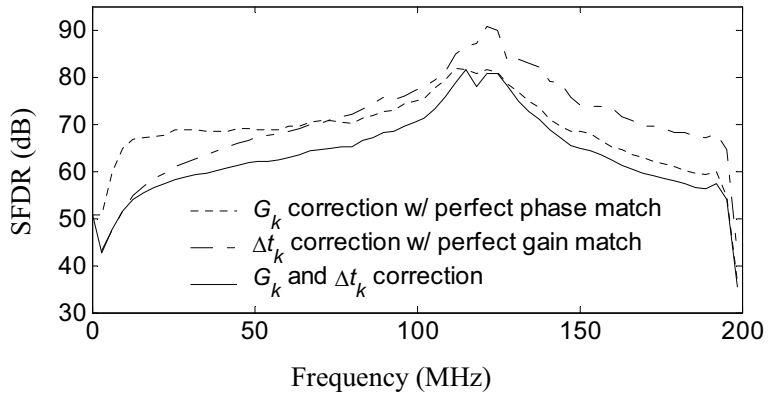

Figure 2.12: Performance comparison between parametric (i.e. frequency-independent) and comprehensive (i.e. frequency-dependent) mismatch correction. Dotted and dash-dot line each represents the limiting SFDR after frequency-independent correction considering only gain and phase mismatch, respectively.

SFDR achievable after frequency-independent correction, limited by the residual gain (or phase) mismatch assuming no phase (or gain) mismatch.

2.6.5 System Drift

The TIADC prototype system was put into 4 h of continuous operation after a 1.5 h warm-up period. Data was acquired every half hour. Correction FIR filters were designed using the first acquisition data, and SFDR performance was evaluated for every subsequent data. Calibration accuracy (∼80 dB of SFDR) was maintained up to the third acquisition (1 h operation). The loss of SFDR after 4 h was approximately 10–15 dB. We expect that the drift rate may be much less

with a monolithic implementation, where thermal gradients and PC-boards and cable phase shifts are minimized.

2.7 Conclusions

Digital correction of frequency-dependent mismatch error is essential for high-resolution and high-speed TIADCs. In this chapter, a general linear correction method is proposed and demonstrated, which is additionally capable of exploiting stopband structure. Although linearity is assumed, actual ADCs may exhibit significant nonlinearity. For example, it has been found experimentally that the CTF is a weak function of input signal amplitude. For a high-resolution converter, even a slight calibration detuning may result in a significant loss of SFDR. Further research will be required to address secondary effects not considered in this chapter such as nonlinearity, temperature effect, aging, component drift, etc.

Chapter 3

Mismatch Correction for TIADCs: Blind Method

The previous chapter discussed about a training-based method for TIADC mismatch correction. Training-based calibration method, in general, provides superior accuracy due to the dedicated characterization setup. However, it is not a suitable correction method when mismatches are time varying, or when the system interruption is not allowed, for example. Under these special circumstances, we have to find another way of mismatch correction with the system continuously working on data conversion. A *blind* method serves this need in that no special calibration signal or system stoppage is required [48–51], and therefore complements the training-based calibration methods. A new blind method is proposed in this chapter, based on wide-sense stationary (WSS) assumption. The proposed method is more comprehensive than previous efforts since we do not rely on special distribution or bandwidth restriction of the input signal, other than WSS

property and Nyquist sampling criterion. It is also novel that gain and sampling time mismatches are incorporated within a common framework of parameterized filter banks. Based on the cyclic spectral density representation of wide-sense cyclostationary (WSCS) signals, a proof is given that the proposed algorithm always achieves mismatch correction for a two-channel TIADC.

Section 3.1 gives background and system model based on the parameterized filter bank. Characterization of WSCS processes is discussed in Section 3.2. The proposed algorithm is described along with the sufficiency check in Section 3.3. Simulation and experimental results are presented in Section 3.4 and Section 3.5, respectively.

3.1 Background and System Model

Figure 3.1(a) shows a two-channel TIADC system. Individual A/D converters have $2T_s$ of conversion time so that the aggregate sampling rate is f_s ($=1/T_s$). Each channel has respective gain, G_i, and timing error, Δt_i. In practice, sub-converters will also have different dc offsets, but we assume they are independently compensated. The input $x(t)$ is assumed bandlimited from dc to $f_s/2$. Figure 3.1(b) is an equivalent system where quantization effects are ignored. A simple transform yields a normalized system in Figure 3.1(c). If we regard $x'(t)$ as the new TIADC input, then the upper channel becomes error-free, and it is immediately seen that only relative errors, i.e. $G^* \equiv G_1/G_0, \Delta t^* \equiv \Delta t_1 - \Delta t_0$, are relevant. This normalization is justified when raw mismatches are relatively small, or when we are not interested in the change of the output signal in absolute timing and magnitude. Whenever $G^* \neq 1$ or $\Delta t^* \neq 0$, the TIADC effectively modulates the input. Modulation sidebands (i.e., "aliasing spurs") are then produced at the output, limiting the maximum signal-to-noise plus distortion ratio (SNDR) and spurious-free dynamic range (SFDR) achievable.

Once mismatches are estimated or measured, a reconstruction system can be cascaded (Figure 3.1(d)) for mismatch correction so that the aliasing spurs no longer limit the spectral performance. In standard offline calibration methods [11],

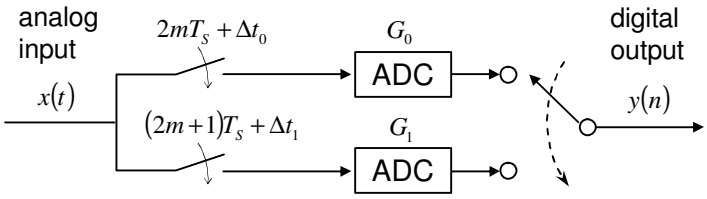

(a) Actual system

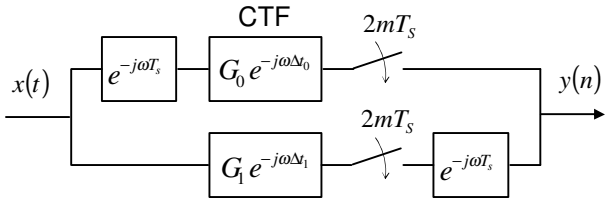

(b) Equivalent system

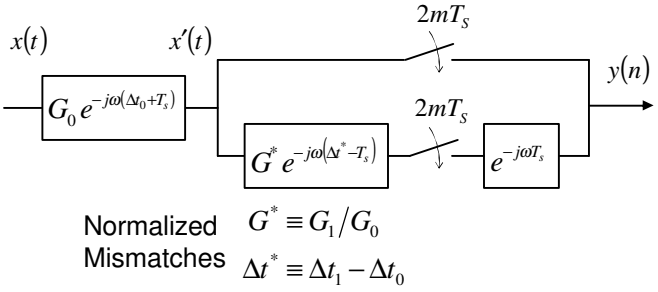

(c) Normalized system

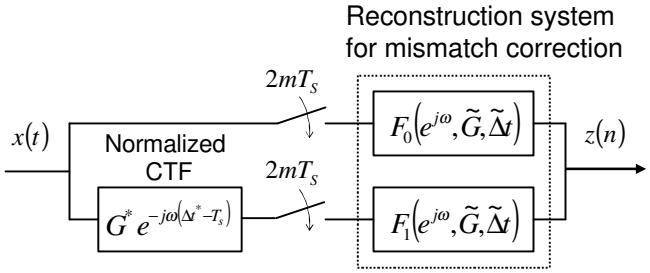

(d) Cascaded with a reconstruction system

Figure 3.1: Two-channel TIADC system

a known input signal is applied, and observing the output enables us to characterize channel mismatches. Our objective is, however, to estimate and correct the mismatches without explicit (in a deterministic sense) knowledge of the input . First, note the key fact that a TIADC system is linear time-invariant (LTI) if and only if it is aliasing-free, and linear periodically time-varying (LPTV) otherwise [52]. Thus, an equivalent statement of our goal is, to design the reconstruction system so that the overall TIADC system regains LTI property, without explicitly knowing the input. It is also known that, for every WSS input, an LTI and LPTV system yields a WSS and WSCS output, respectively. This is basic motivation for the proposed blind correction method which can be stated as follows: *assuming* $x(t)$ *is a zero-mean WSS random process, design reconstruction filters so that the output* $z(n)$ *also becomes WSS*. It is emphasized that the sufficiency of this input-output pairwise WSS condition remains to be proven. Equivalently, it is needed to check if this pairwise WSS condition guarantees that the entire TIADC system is LTI. This check is practically important due to the undesirable possibility of false correction, i.e., both input and output are WSS, but with nonzero residual mismatches.

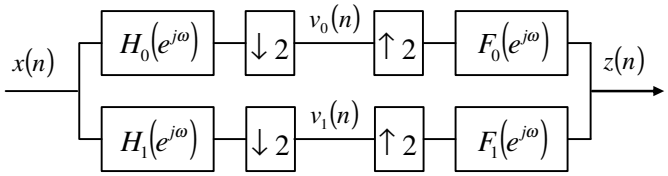

Figure 3.2: Two-channel filter bank system.

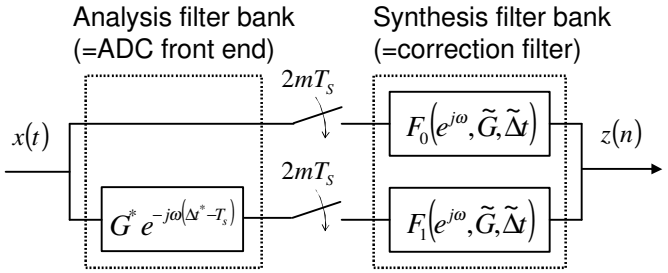

Figure 3.3: Filter bank model of a $M = 2$ TIADC.

3.1.1 Parameterized Filter Bank Model

There can be several realizations of the reconstruction system in Figure 3.1(d) [48–51, 53]. Although their signal processing is all equivalent, i.e., mismatch correction, it is noted that gain and timing mismatches traditionally have been individually equalized. The present thesis proposes to employ a parameterized filter bank for unified treatment of gain and timing errors. The filter bank representation also provides convenient framework for the sufficiency check of the pairwise WSS condition, as will be seen in later section.

A filter bank consists of analysis filters and synthesis filters as in Figure 3.2, and is a useful tool for general multi-rate digital signal processing applications [52].

Similarities between Figure 3.2 and Figure 3.1(d) are readily seen. A TIADC with correction filters can be interpreted as a filter bank as shown in Figure 3.3 with the choice of an analysis bank, $H_0(j\omega) = 1$ and $H_1(j\omega) = G^* e^{-j\omega(\Delta t^* - T_s)}$, for $|\omega| < \omega_s/2 = \pi/T_s$ (Undersampling switches in Figure 3.1(d) is equivalent to the cascade of two-fold decimator and interpolator in Figure 3.2).

The alias component (AC) matrix for the analysis and synthesis bank is then defined by [52]

$$\begin{aligned}
\mathbf{H_{AC}}(\omega) &= \begin{pmatrix} H_0(\omega) & H_1(\omega) \\ H_0(\omega - \omega_s/2) & -H_1(\omega - \omega_s/2) \end{pmatrix} \\
&= \begin{pmatrix} 1 & G^* e^{-j\omega(\Delta t^* - T_s)} \\ 1 & -G^* e^{-j(\omega-\omega_s)(\Delta t^* - T_s)} \end{pmatrix}, (0 \le \omega < \omega_s/2) \qquad (3.1) \\
\mathbf{F_{AC}}(e^{j\omega}) &= \begin{pmatrix} F_0(e^{j\omega}) & F_1(e^{j\omega}) \\ F_0(e^{j(\omega-\omega_s/2)}) & -F_1(e^{j(\omega-\omega_s/2)}) \end{pmatrix}.
\end{aligned}$$

3.1.2 Correction Filter Calculation

It can be shown that the perfect reconstruction condition for this two-channel filter bank, in terms of AC matrices, is given by

$$\mathbf{H_{AC}}(\omega)\mathbf{F_{AC}^T}(e^{j\omega}) = 2\mathbf{I}. \qquad (3.2)$$

It follows that

$$\mathbf{F_{AC}}(e^{j\omega}, G, \Delta t) = 2\mathbf{H_{AC}^{-T}}(\omega, G, \Delta t), \tag{3.3}$$

where $\mathbf{I}$ is a 2×2 identity matrix. The dependence of $\mathbf{H_{AC}}$ and $\mathbf{F_{AC}}$ on mismatch parameters is explicitly shown for clarity. The first row of $\mathbf{F_{AC}}$, i.e. $[F_0(e^{j\omega})$ $F_1(e^{j\omega})]$, completely specifies the reconstruction system required for gain and timing mismatch correction. The true mismatch parameters (G^*, Δt^*) are unknown *a priori*, and therefore we instead rely on their estimates, ($\widetilde{G}$, $\Delta\widetilde{t}$), to calculate the reconstruction filters by (3.3).

3.2 Characterization of Cyclostationary Process

The characterization of WSCS processes is central to the proposed blind estimation method, and is briefly reviewed in this section following the convention in the literature [54, 55]. The autocorrelation function of a real-valued zero-mean random process $y[n]$ is given by

$$R_y[n, n'] = E[x[n]x[n']] \text{ for all } n \text{ and } n'.$$

If $x[n]$ is WSS, its autocorrelation function, by definition, only depends on a time lag, such that

$$R_y[u] = R_y[n + u, n] \text{ for all } n \text{ and } u. \tag{3.4}$$

Note again that the output of an LTI system (e.g., mismatch corrected TIADC), with a WSS input, is always WSS. On the other hand, the output autocorrelation out of an LPTV system (e.g., mismatch uncorrected TIADC) features periodic shift-dependence, such that

$$R_y[n+M, n'+M] = R_y[n, n'] \text{ for all } n \text{ and } n'. \tag{3.5}$$

Equation (3.5) defines WSCS random processes with period M. Since $R_x[n+u, n]$ is periodic with respect to n, its Fourier series coefficient can be obtained by

$$R_x^\alpha[u] = \frac{1}{M} \sum_{k=0}^{M-1} R_x[k+u, k] e^{-j2\pi\alpha k}, \tag{3.6}$$

where $\alpha \in \{0, 1/M, ..., (M-1)/M\}$ has a physical interpretation of frequency. Each coefficient is a function of the time lag u, which suggests we can define a spectral density for each $R_x^\alpha[u]$ as follows.

$$S_x^\alpha(\omega) = \sum_{u=-\infty}^{\infty} R_x^\alpha[u] e^{-j\omega u}. \tag{3.7}$$

$R_x^\alpha[u]$ and $S_x^\alpha(\omega)$ are called the cyclic correlation function and cyclic spectral density of $x[n]$, respectively, and either one for all α completely characterizes a WSCS process. In the special case when $x[n]$ is WSS, only $R_x^0[u]$ and $S_x^0(\omega)$ are nonzero, and they reduce to the conventional autocorrelation function and spectral density for a WSS process.

For the $M = 2$ filter bank in Figure 3.2, cyclic spectral density matrices for the input $x[n]$ and output $z[n]$ is defined as follows [55], where $x[n]$ is assumed

WSS.

$$\begin{aligned} \mathbf{S_x}(\omega) &= \begin{pmatrix} S_x^0(\omega) & 0 \\ 0 & S_x^0(\omega - \omega_s/2) \end{pmatrix}, \\ \mathbf{S_z}(\omega) &= \begin{pmatrix} S_z^0(\omega) & S_z^{\frac{1}{2}}(\omega) \\ S_z^{\frac{1}{2}}(\omega - \omega_s/2) & S_z^0(\omega - \omega_s/2) \end{pmatrix}. \end{aligned} \tag{3.8}$$

It is noted these matrices becomes diagonal for a WSS signal. $\mathbf{S_z}(\omega)$ can be written as a function the input cyclic spectral density $\mathbf{S_x}(\omega)$ and AC matrices, as follows.

$$\mathbf{S_z}(\omega) = \frac{\mathbf{1}}{\mathbf{4}} \left(\mathbf{F_{AC}} \mathbf{H_{AC}^T}\right) \mathbf{S_X}(\omega) \left(\mathbf{F_{AC}} \mathbf{H_{AC}^T}\right)^{\mathbf{H}}, \tag{3.9}$$

where the frequency and mismatch parameter dependency of AC matrices is omitted for simplicity. $(\cdot)^*$ and $(\cdot)^H$ denote complex conjugate and complex conjugate transpose, respectively.

Cyclic correlation funcions or cyclic spectral densities provide a convenient measure of how a given signal is close to being WSS or WSCS, which is exploited by the proposed algorithm described next.

3.3 Algorithm Description and Sufficiency Check

Referring to Figure 3.1(d), let $x(t)$ be the TIADC output, assumed WSS, and $z[n]$ be the output of the reconstruction system designed by (3.3) with mismatch estimates $(\widetilde{G}, \Delta\widetilde{t})$. Let's define the following error measure to quantify how $z[n]$

is close to being WSS.

$$J = \sum_{u=0}^{U_{max}} \sum_{\alpha \neq 0} \left(R_y^{\alpha}(u) \right)^2, \tag{3.10}$$

where U_{max} is the maximum time lag to consider. Then, the best estimates $(\widetilde{G}_{opt}, \widetilde{\Delta}t_{opt})$ can be obtained by minimizing the error measure J.

$$(\widetilde{G}_{opt}, \Delta\widetilde{t}_{opt}) = \arg\min_{(G,\Delta t)} J \tag{3.11}$$

When $(\widetilde{G}_{opt}, \Delta\widetilde{t}_{opt})$ is equal to the true mismatches $(G^*, \Delta t^*)$, which is the desired case, $z[n]$ becomes WSS, and J is identically zero.

Now, consider this question: Is there any other $(\widetilde{G}_{opt}, \Delta\widetilde{t}_{opt}) \neq (G^*, \Delta t^*)$ which will also yield zero error measure? First, assume J is zero, i.e., pairwise WSS condition, with both $\mathbf{S_x}(\omega)$ and $\mathbf{S_z}(\omega)$ being a diagonal matrix. For simplicity, let $\mathbf{H_{AC*}} = \mathbf{H_{AC}}(\omega, G^*, \Delta t^*)$ and $\widetilde{\mathbf{H}}_{\mathbf{AC}} = \mathbf{H_{AC}}(\omega, \widetilde{G}, \Delta\widetilde{t})$. With the parameterized reconstruction filter bank $\mathbf{F_{AC}} = 2\widetilde{\mathbf{H}}_{\mathbf{AC}}^{-\mathbf{T}}$, (3.9) can be rewritten as

$$\widetilde{\mathbf{H}}_{\mathbf{AC}}^{T} \mathbf{S_z}(\omega) \widetilde{\mathbf{H}}_{\mathbf{AC*}}^{*} = \mathbf{H}_{\mathbf{AC}}^{\mathbf{T}} \mathbf{S_x}(\omega) \mathbf{H}_{\mathbf{AC*}}^{*}. \quad (|\omega| < \omega_s/2)$$

This, in turn, can be cast into the form,

$$\mathbf{C}(\omega)\mathbf{s}(\omega) = \mathbf{0}, \tag{3.12}$$

where $\mathbf{C}(\omega)$ is a 4×4 coefficient matrix. $\mathbf{s}(\omega)$ is a non-negative vector, consisting of input and output power spectral densities,

$$\mathbf{s}(\omega) = \left[S_x^0(\omega) \;\; S_x^0(\omega - \omega_s/2) \;\; S_y^0(\omega) \;\; S_y^0(\omega - \omega_s/2) \right]^T.$$

Note the implicit constraint from physical reasoning: elements of $\mathbf{s}(\omega)$ are non-negative, and at least one of them is nonzero (i.e. positive) at some frequency. Any combination of $\left(\widetilde{G}_{opt}, \Delta\widetilde{t}_{opt}\right)$ and $(G^*, \Delta t^*)$ will result in the pairwise WSS condition, as long as it supports a nontrivial null space vector of $\mathbf{C}(\omega)$ with the above constraint. It can further be shown that, the only possible combination is $\widetilde{G} = \pm G^*$, and $\Delta\widetilde{t} = \Delta t^*$, provided $|\Delta t|, |\Delta\widetilde{t}| < T_s$. Under the small-mismatch regime, which is usually met in practice, sign ambiguity in gain is easily resolved, and timing mismatches are also smaller than the sampling interval T_s. This proves that the accomplishment of pairwise WSS condition is indeed sufficient for mismatch correction, and therefore we are assured that there is no false correction for a two-channel TIADC.

The rank of $\mathbf{C}(\omega)$ in (3.12) is two, and its null space is spanned by any $\mathbf{s}(\omega)$ satisfying $S_z^0(\omega) = S_x^0(\omega)$, and $S_z^0(\omega - \omega_s/2) = S_x^0(\omega - \omega_s/2)$. This is a direct result of the perfect reconstruction property by a parameterized filter bank

3.4 Simulation Results

This section presents simulation results to demonstrate the proposed correction method. The following example signals are considered as a representative narrowband and wideband input.

- *SINE*: Single sinusoid at frequency $0.15\omega_s$.
- *WIDE*: Uniform i.i.d samples filtered by h=[0.925 −0.277 −0.185 0.185], and further bandlimited to $0.45\omega_s$ by a 5th-order Butterworth filter.

The impulse response of a raised-cosine filter with 10% excessive bandwidth, after shifted by $\Delta t^* = 0.041T_s$, multiplied by $G^* = 0.917$, and sampled at every T_s, serves as a normalized mismatch response for $M = 2$ TIADC in Figure 3.1. Then, 10-bit quantization is applied throughout the simulation. The reconstruction system consists of two 51-tap FIR filters designed by a conventional frequency-sampling method, and parameterized by $(\widetilde{G}, \Delta\widetilde{t})$.

Empirical autocorrelation function for a raw (uncorrected) TIADC output is first estimated by time averaging. Then, the autocorrelation function, after reconstruction filters, is obtained by double-sided convolution, from which $R_z^{\alpha}[u]$ follows. For the calculation of the error measure in (3.10), the maximum time lag $U_{max} = 10$ for all cases. The number of samples used for correlation estimation is N.

First, the error measure (3.10) is examined on a $(\widetilde{G}, \Delta\widetilde{t})$ space as shown in Figure 3.4. The actual shape of error surface depends on the input signal, but a well-defined global minimum at $G^* = 0.917$ and $\Delta t^*/T_s = 0.041$ is clearly seen in both cases.

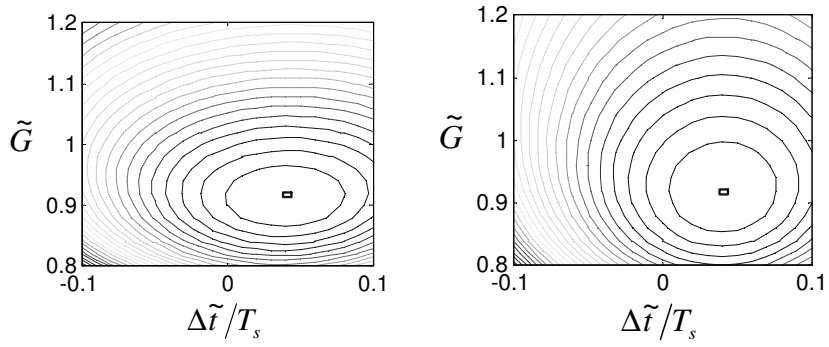

(a) *SINE* input (b) *WIDE* input

Figure 3.4: Calculated error surface (3.10) with $N = 10^4$.

Next, Monte Carlo run is performed varying the sample size N from 10^2 to 10^6 (30 simulations for each sample size). Mismatch parameters are uniformly distributed within $\pm 10\%$ and $\pm 5\%$ for G^* and $\Delta t^*/T_s$, respectively. After the blind mismatch correction, the standard deviation of residual mismatches, $G^*/\widetilde{G}$ and $\left(\Delta t^* - \Delta\widetilde{t}\right)/T_s$, are recorded. Figure 3.5(a) and Figure 3.5(b) shows the standard deviation of gain and sampling time mismatches, respectively. Correction accuracy is seen to improve as the length of observation increases. The estimation accuracy for *SINE* input is mainly limited by the reconstruction filter for this simulation, which explains the flattening of the deviation curve around $N = 10^5$. The residual error, however, can be further reduced by using longer FIR filters (i.e. >51 taps). In contrast, for *WIDE* input, the estimation error of sample autocorrelation function is seen to dominate residual mismatches. Richer spectrum

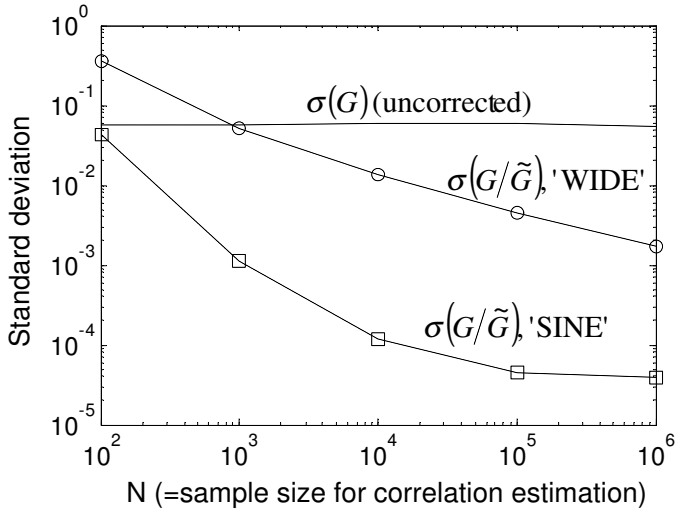

(a)

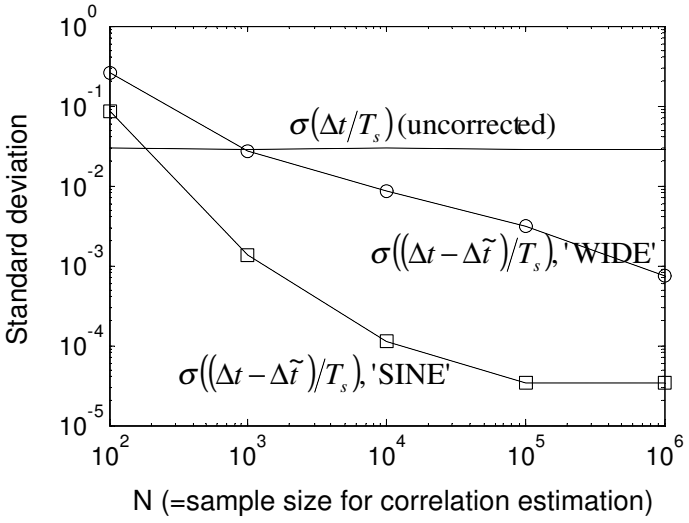

(b)

Figure 3.5: Monte Carlo simulation result for a $M = 2$ TIADC. Dotted and solid lines denote standard deviation before and after blind correction, respectively. Residual mismatches after correction are marked with a circle and square for *WIDE* and *SINE* input, respectively.

of *WIDE* input than *SINE* renders its performance more sensitive to observation sample size.

At $N = 10^5$, residual mismatches are suppressed by 20 dB and 50 dB with *WIDE* and *SINE* input, respectively. This will directly translate to the increase in SFDR or SNDR by the same amount under mismatch dominant regime.

3.5 Experimental Results

In this section, experimental results are presented to demonstrate the proposed blind method. Various input signals are applied to a prototype $M = 2$ TIADC, and the proposed blind correction method is evaluated for each input signals. Performance improvement, as well as limitations, will be discussed.

3.5.1 Setup

Experimental results on this section is based on the experimental TIADC prototype in Figure 2.5. In order to generate wideband signals, an arbitrary waveform generator (AWG520 from Sony/Tektronix) is employed. Clock and input signals are fed to four A/D boards (AD6645 from Analog Devices, Inc.), each having 14-bit resolution and 100-Msamples/S (MSPS) of sampling rate. A logic analyzer captures the digital output, and mismatch correction is carried out

on MATLAB. The setup in Figure 2.5 has four channels overall ($M = 4$), but can be configured as a $M = 2$ TIADC as well by pairing channel-1 with channel-3, or channel-2 with channel-4. Each pairing will be referred to as *TIADC-13* and *TIADC-24*.

The overall experiment consists of two phases: *Estimation Phase* and *Evaluation Phase*. The purpose of *Estimation Phase* is to obtain the best estimate of static gain and timing delay, given test input signals. Correction filter coefficients can then be calculated based on these estimates. In *Evaluation Phase*, we perform a series of single-tone SFDR tests over entire the first Nyquist Zone to see how well the mismatch correction suppresses aliasing error. Since we are only interested in the suppression of gain-timing mismatch, offset spurs and harmonics from the signal generator is disregarded in measuring SFDR.

1. *Estimation phase*
   (a) Apply test input signal (Section 3.5.2)
   (b) Find the best parameter estimate by (3.10) and (3.11).
   (c) Calculate correction filter coefficients by (3.3).

2. *Evaluation phase*
   (a) Apply a series of single-tones covering an entire Nyquist zone (dc–$f_s/2$).
   (b) Measure SFDR for each evaluation frequency.

Optimization of the error measure in (3.10) is carried out by calling a MATLAB built-in function, *fminsearch*, with all available data samples, rather than in

adaptation with incremental samples [49–51]. This allows us to look at more fundamental behaviors without artifacts due to the adaptation. No local minimum was observed throughout optimization runs. Important parameters are $L(=71)$, the number of correction filter taps, $N(=3 \cdot 10^4$ for sinusoids, and 10^6 otherwise), observation sample size, and U_{max} (=10), autocorrelation window in (3.10). Default values are shown in the parenthesis.

3.5.2 Test Input Signals for Blind Estimation

Blind estimation methods observe only the TIADC output without *a prior* knowledge to the input signal. Their performance is, therefore, expected to vary with one input signal to another. There are in general an infinite number of input signals that could possibly be applied to a TIADC, but exhaustive input test is obviously not possible. In this work, two presentative classes of input signals are considered for *Estimation Phase*.

- Narrowband signals: Sinusoids from 1.6–99.2 MHz in steps of 1.6 MHz.
- Wideband signals: dc–80 MHz$(=0.4f_s)$ bandwidth signals with six different spectrum shaping (Figure 3.6).

Wideband signals are prepared by generating an i.i.d sequence of uniform-distributed samples, filtering sharply to define the occupied bandwidth$(=0.4f_s)$,

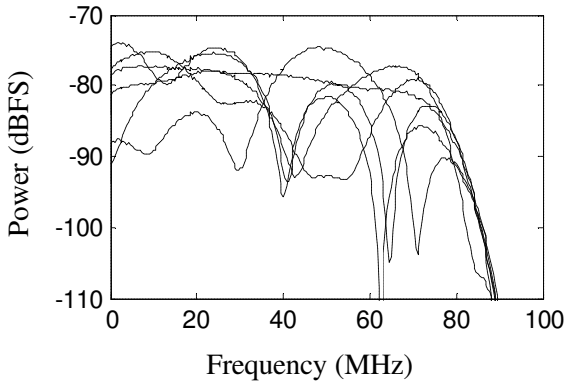

Figure 3.6: Spectra of six 80 MHz bandwidth test signals for blind mismatch estimation).

and spectrum-shaping by six different 10-tap FIR filters with arbitrary coefficients. See Figure 3.6 for their measured spectra.

3.5.3 Measured Channel-Transfer-Function

Figure 3.7 shows measured (and normalized) CTF's for *TIADC-13* and *TIADC-24* characterized by a training method in Chapter 2. In this figure, it is seen that, except at low frequencies below 20 MHz, the CTF can be approximately described by a static gain time delay model, $(G, \Delta t)$, which is roughly $(1.002, 0.005T_s)$, and $(0.99, 0.002T_s)$ for *TIADC-13* and *TIADC-24*, respectively. Large deviations from gain-timing model, below 20 MHz, is due to the mismatch in input transformer cut-off frequencies on ADC boards.

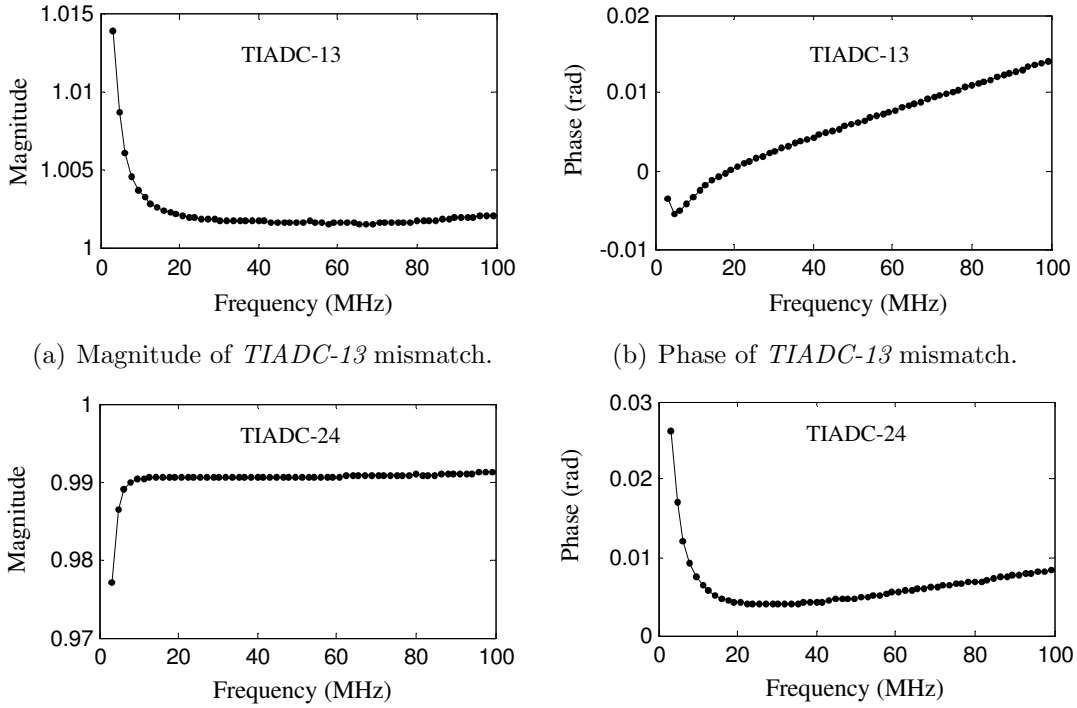

(a) Magnitude of *TIADC-13* mismatch.

(b) Phase of *TIADC-13* mismatch.

(c) Magnitude of *TIADC-24* mismatch.

(d) Phase of *TIADC-24* mismatch.

Figure 3.7: Measured channel-transfer-functions (CTF) for *TIADC-13* ((a),(b)) and *TIADC-24* ((c),(d)).

The parametric blind method proposed in this chapter will remove such static gain and time delay mismatches. There will remain, however, residual mismatch responses which cannot be entirely removed by gain-timing correction alone, limiting the performance of gain-timing error correction. This modeling error is a fundamental drawback of gain-timing correction approaches, and will be further investigated in the next section. In general, full correction of frequency-dependent

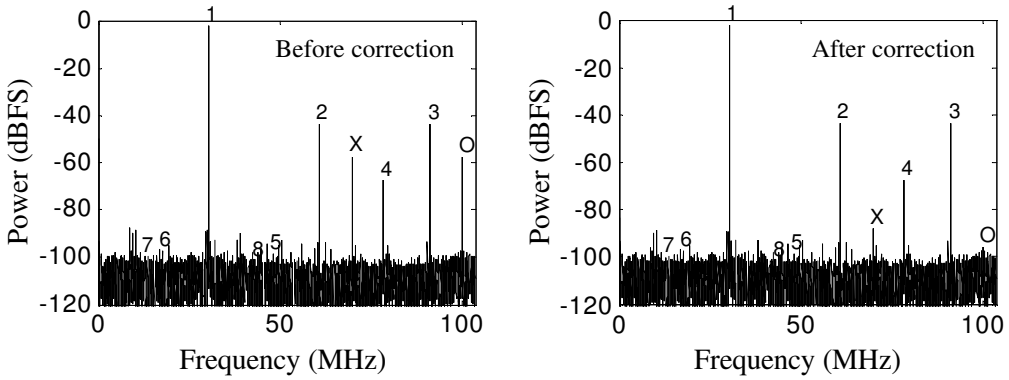

(a) (b)

Figure 3.8: Typical output spectrum (a) before, and (b) after blind correction. The input is a single tone at 30.4 MHz. The gain and timing mismatch spurs are marked as 'X', and offset spur as 'O'. Harmonics from the signal generator are marked with numbers.

mismatches will require either training methods in Chapter 2 or generalized blind correction methods in Chapter 4.

3.5.4 Blind Correction with Sinusoidal Inputs

In this section, the proposed blind method is demonstrated with narrowband input signals. First, in the *Estimation Phase*, a single tone at a certain input frequency is applied for blind estimation (Section 3.5.1). Then, The *Evaluation Phase* performs a single-tone SFDR test. Figure 3.8 shows typical TIADC output spectrum before and after blind correction. It is seen that the mismatch spur is suppressed by 30 dB after blind correction.

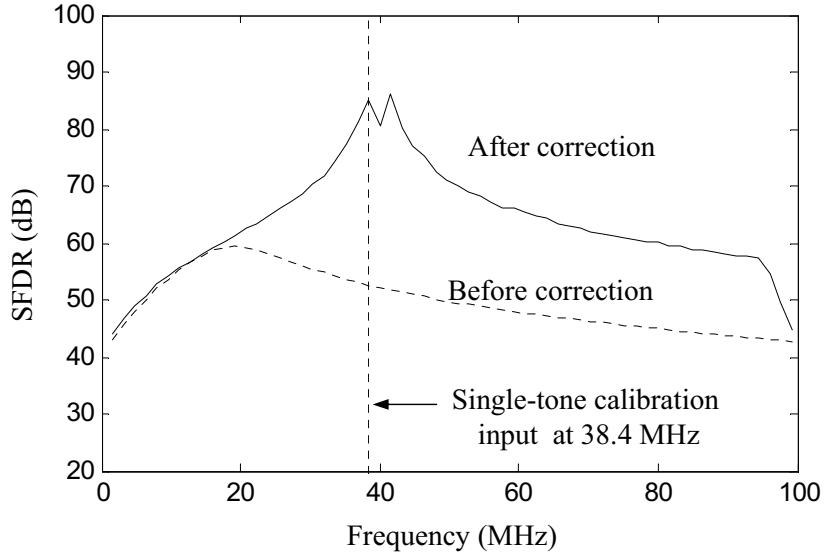

Figure 3.9: Measured full-band SFDR characteristic (*TIADC-13*) after blind mismatch estimation with a 38.4 MHz single-tone.

Figure 3.8 proves that the blind method effectively removes channel mismatches at the estimation (i.e. calibration) frequency. Will the error correction still be good at all other frequencies? Figure 3.9 shows SFDR test results across the entire Nyquist zone. Calibration frequency is 38.4 MHz for the *Estimation Phase*. It is seen that SFDR is improved over the entire Nyquist zone by up to 30 dB. Specifically, the improvement in SFDR is at its peak (> 80 dB) around the calibration frequency 38.4 MHz. As we move away from the calibration frequency, the SFDR starts to drop. Note here two important properties of the blind correction method based on gain-timing model.

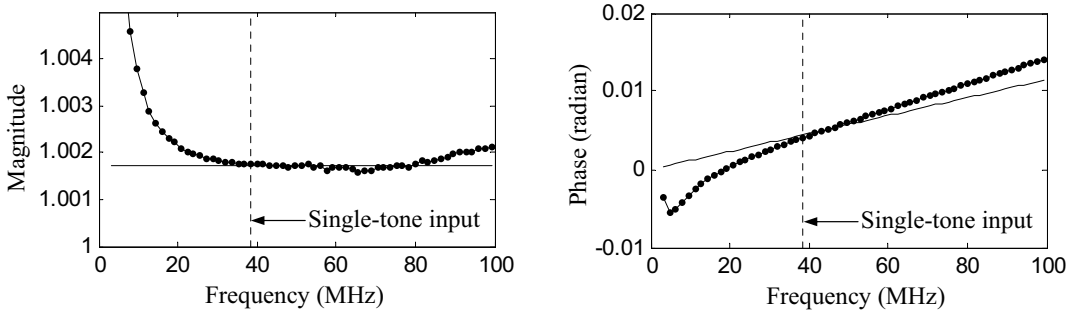

(a) (b)

Figure 3.10: Comparison of the true mismatch response (dot) and gain-timing model (solid line). Gain and time-delay parameters were obtained with a single-tone input at 38.4 MHz. Therefore, the gain-timing model provides near perfect magnitude/phase match to the true mismatch response at 38.4 MHz. The global fit is not as good.

1. The blind algorithm only *sees* the CTF at those frequencies where the TIADC input has nonzero power. In other words, the TIADC output does not have any information about the unexcited mode of the A/D converter frequency response.

2. The blind algorithm seeks to find the best estimate (G,Δt) which can compensate for the excited mode of the actual mismatch response. Assume a single-tone input at ω_{in}, and the CTF at this frequency $H(j\omega_{in})$. Then, the blind algorithm will conclude parameter search with the following equivalent gain and time delay.

$$\begin{aligned} G_{eq} &= |H(j\omega_{in})|\,, \\ \Delta t_{eq} &= \frac{\angle H(j\omega_{in})}{\omega_{in}} \end{aligned} \tag{3.13}$$

Therefore, if the actual CTF is exactly represented by static gain and time delay over the entire Nyquist zone, then the estimates (3.13) will provide perfect mismatch correction over the full Nyquist zone. If, however, the CTF deviates from (G,Δt) model, then (3.13) will provide only narrowband mismatch correction at ω_{in}. At other frequencies, the mismatch may or may not be corrected. Figure 3.10 compares the true mismatch response and its best estimate at the calibration frequency of 38.4 MHz. It is seen that the estimated gain-timing model near perfectly match the true mismatch at the calibration frequency, but obviously global match is not as good. Figure 3.13 shows similar SFDR results with different calibration frequencies.

Noting that the correction is still locally valid around the calibration frequency, even in the presence of modeling error, one can now recalculate the correction filter for every SFDR evaluation frequency, and the result is shown in Figure 3.12. Since the correction filter is re-designed for every evaluation frequency, now the SFDR consistently improves across the entire Nyquist range. This level of correction performance is nearly equivalent to the training method (e.g. compare Figure 3.12 with Figure 2.10(b)). It is noted that, however, in a training method, the full-band correction is achieved by a *single* set of filter coefficients, unlike the blind method case where correction filters are re-designed for every input sinusoidal frequency. Sudden SFDR drop around 50 MHz is due to the artificial, unreal

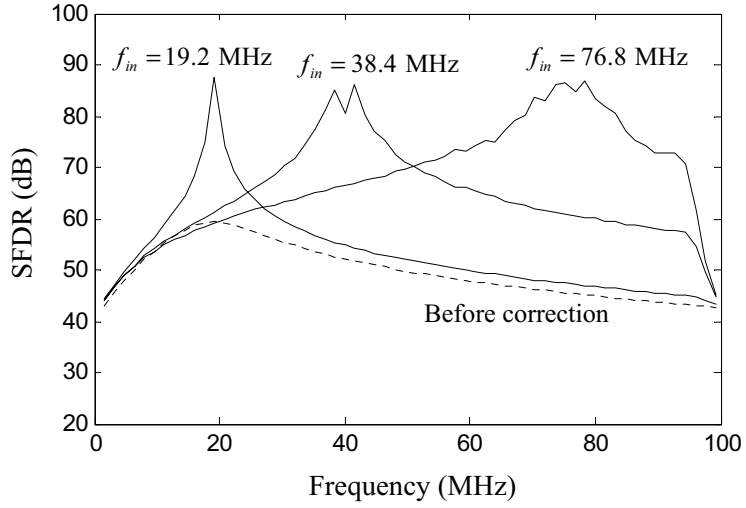

(a) *TIADC-13*

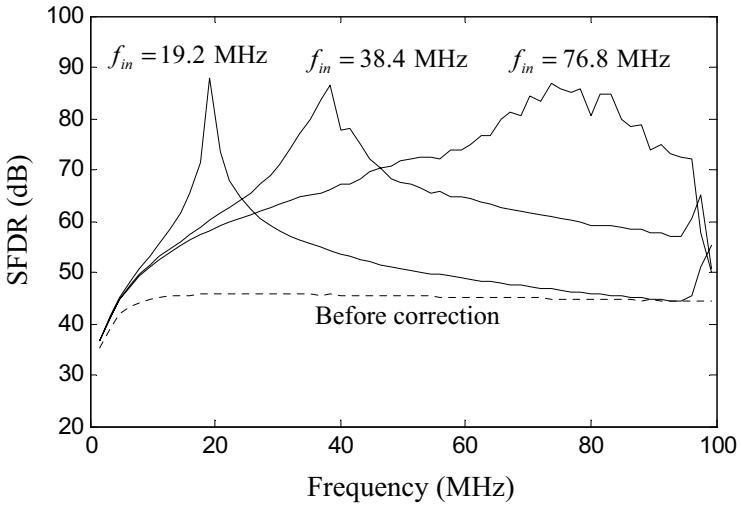

(b) *TIADC-24*

Figure 3.11: Measured SFDR characteristics after single-tone blind estimation. Correction filter coefficients are fixed once calculated with three different sinusoidal input signals. Compare with Figure 3.12.

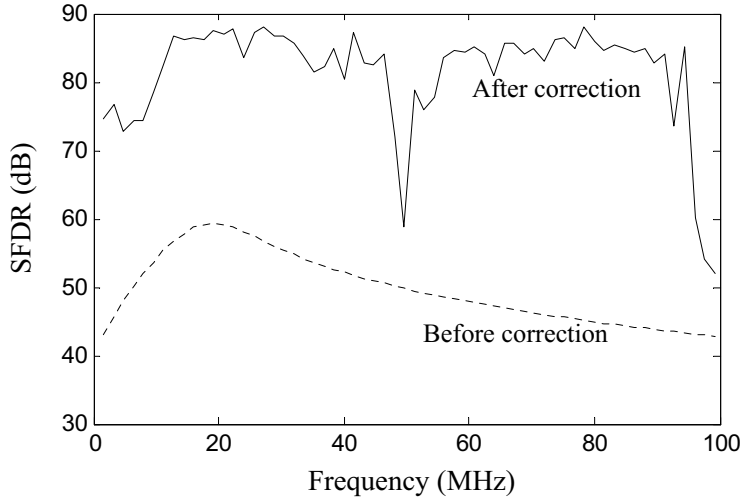

(a) *TIADC-13*

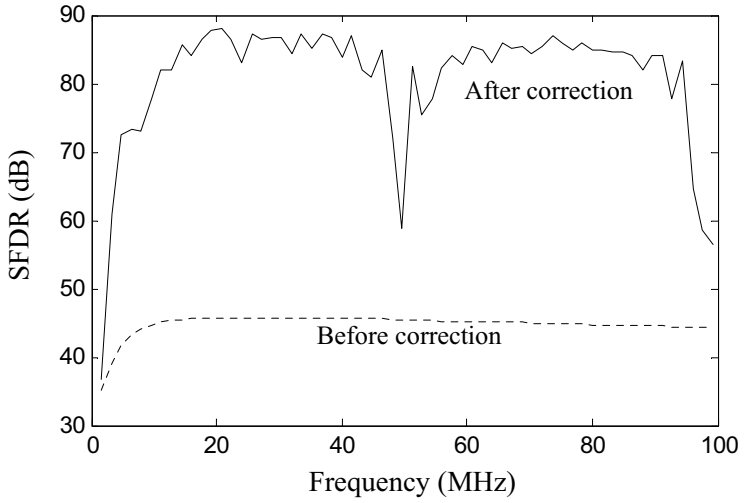

(b) *TIADC-24*

Figure 3.12: Measured SFDR characteristics after single-tone blind estimation. Correction filter coefficients are re-calculated at every SFDR evaluation frequency. Compare with Figure 3.11.

mismatch induced by the input signal, not actual channel mismatches. A single period of a 50 MHz sinusoid is exactly equal to $4T_s$, such that, in the worst case, the first and second A/D converter may only catch peaks and zero-crossings, or vice versa, of the input sinusoid, respectively. This signal-induced mismatch is indistinguishable from actual channel mismatches with the present method. Put in another way, input WSS assumption is not valid in this case and we need either much longer observation or randomization techniques.

Figure 3.11 and Figure 3.12 are representative demonstrations of the blind method assuming narrowband WSS signals. In reality, the center frequency of the input may be time-varying and the correction filter will also be updated at a certain rate. Figure 3.11 shows the expected SFDR performance after a sudden change in input frequency before filter coefficients are updated. Figure 3.12, on the other hand, exemplifies the opposite scenario where the input frequency changes more slowly than the coefficient update rate.

3.5.5 Blind Correction with 80 MHz Bandwidth Signals

Six 80-MHz bandwidth signals are applied for the purpose of mismatch estimation. The SFDR performance is evaluated by using sinusoids and summarized in Figure 3.13. The blind algorithm now *sees* the CTF over a wider range of frequencies than the narroband input case, and therefore the improvement in SFDR

is more evenly distributed across the entire frequency range, than the narrowband input case (Figure 3.11).

3.5.6 The Effects of Observation Sample Size

The estimation error of the proposed blind method is critically related to the autocorrelation estimation accuracy ((3.10)). Assuming a WSS source, it can be shown that the variance of non-WSS noise of autocorrelation estimation, due to the finite observation, is inversely proportional to N^2 and N, for asymptotically narrowband and wideband signals, respectively. Representative experimental results are shown in Figure 3.14.

3.6 Conclusions

This chapter proposed and demonstrated a novel blind method of mismatch correction for an M=2 TIADC, based on a parameterized filter bank and WSCS characterization of relevant signals. Assuming WSS input, the proposed algorithm corrects gain and timing errors by restoring the shift-invariance of the output autocorrelation function. Extension of the proposed algorithm to $M > 2$ cases should be straightforward, but its corresponding sufficiency check seems to be an open question due to the complexity of the problem.

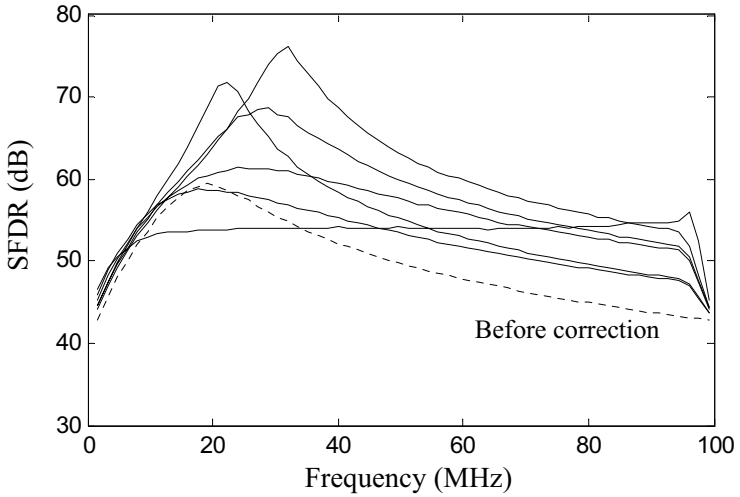

(a) *TIADC-13*

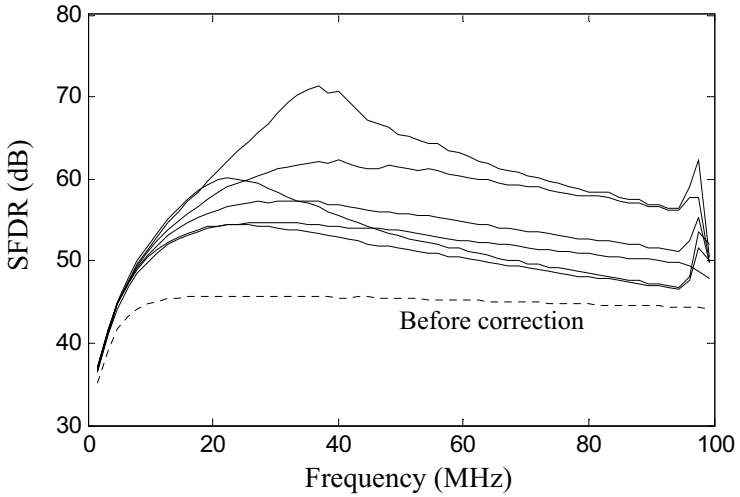

(b) *TIADC-24*

Figure 3.13: Measured SFDR characteristics after wideband blind estimation. Corection filters are calculated with six different 80 MHz bandwidth signals.

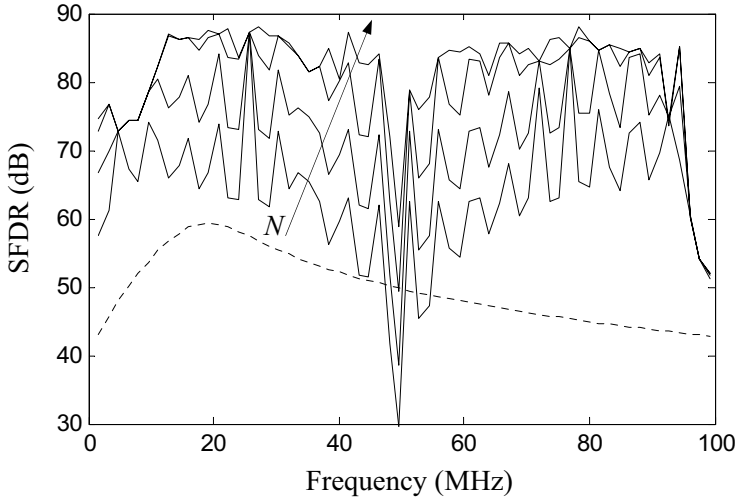

(a) Narrowband input signal. N=10^3, $3 \cdot 10^3$, 10^4, and $3 \cdot 10^4$.

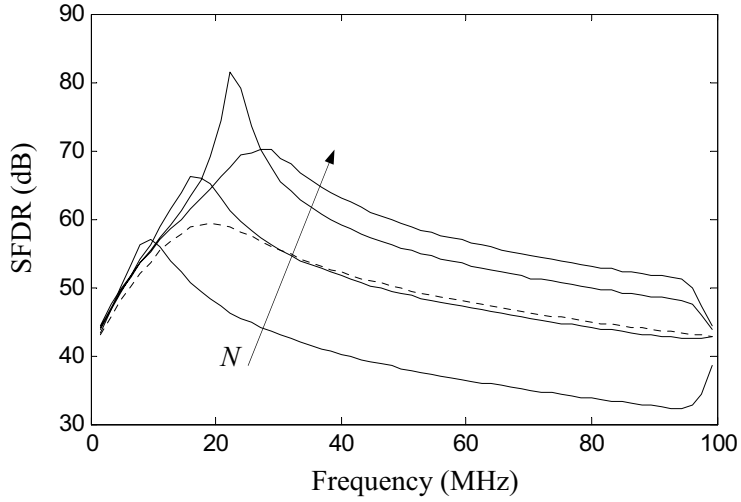

(b) Wideband input signal. N=$3 \cdot 10^4$, 10^5, $3 \cdot 10^5$, and 10^6.

Figure 3.14: The effect of observation sample size N (*TIADC-13*).

The proposed blind method is also experimentally verified. Under the present experimental condition, mismatch modeling error is limiting broadband correction. The finite observation sample size also limits the SFDR performance with wideband signals. In Chapter 4, another novel blind method will be introduced which can effectively address the problem of mismatch modeling error.

In general, blind correction methods can complement training-based calibration methods by providing 100% availability of data conversion and the ability to track time-varying mismatches.

Chapter 4

Mismatch Correction for TIADCs: Generalized Blind Method

In Chapter 3, a blind mismatch correction is proposed, based on the assumption that TIADC channels can be modeled as static gain-timing model. The performance of this gain-timing correction, in general, depends on specific converter hardware and the input signal bandwidth (Section 3.5). If the TIADC input circuitry and sub-converters have high enough bandwidth with no in-band poles or zeros, then the static gain and time delay may adequately model a sub-converter. If, however, the lowest input pole (or zero) is not sufficiently higher than the input bandwidth, the gain and phase response is no longer a straight line. As a result, mismatches in the location of pole (or zero) between channels will produce nonlinear gain and phase response. If the input circuitry has a band-pass nature, the displacement of lower-frequency poles (or zeros) will also result

complicated mismatch behavior [11]. This modeling error is irreducible and acts as residual mismatches, making gain-timing model inadequate for high-resolution applications. The effect of such under-modeled mismatches is more serious with wideband input signals [56].

Generalized mismatch modeling For a higher level of calibration performance, therefore, generalized mismatch correction is necessary to break the limitation of simple gain-timing model. Generalized error modeling, however, poses a fundamental problem to blind techniques: How to *uniquely* identify multiple parameters? Now, we need to handle an increased number of parameters resulting from generalizing correctible mismatches. The blind search algorithm will more likely end up at local minima, resulting *false* correction. The pertinent goal is to find a combination of realistic constraints and mismatch parameterization such that the blind algorithm can uniquely identify a necessary number of mismatch parameters under most practical cases.

Demanding computational cost Blind methods typically require a very high computational cost. Iterative parameter search (closed-form solution generally unavailable) needs accurate gradient information, which involves intensive calculation. Signal reconstruction, given error estimate, is also computationally expensive. This is partly due to the transformation between time- and frequency-

domain, and partly due to the long impulse response in the presence of sampling time error (recall $\text{sinc}(n)$ decays as $1/n$) (Chapter 5 will discuss a special mixed-domain approach to significantly reduce the computational requirement).

In this chapter, a generalized blind correction method is proposed for the first time. The proposed blind estimation method is based on polynomial mismatch modeling, as well as input-WSS assumption. It will be shown that this particular combination enables unique multi-parameter estimation, eliminating false correction in most practical cases.

A very efficient implementation of the proposed method is also presented. The polynomial representation of mismatch errors is actively exploited to get an analytic form of error measure and gradient with no time-frequency transformation. This enables more efficient parameter search and real-time adaptation.

The WSS input assumption is mainly for theoretical purpose, and, in practice, the proposed method performs equally with most stochastically non-WSS signals as well. This is because we rely on time-averaging (rather than stochastic expectation) to get the empirical autocorrelation. Therefore, non-stationary part of the input will be effectively smoothed out, unless the input signal has exact phase relationships with the sampling clock (e.g. $\sin(\pi(m/M)f_s t),\ m = 1, ..., M-1$ where M is the number of TIADC channels)

4.1 System Model

A two-channel TIADC system is shown in Figure 4.1(a). The sample period and frequency of the array is T_s and $\omega_s = 2\pi/T_s$, respectively. The analog input $x(t)$ is bandlimited from dc to $0.5\omega_s$, and assumed to be a real-valued, zero-mean and WSS random process. Figure 4.1(b) illustrates a linear equivalent model with channel transfer function (CTF) $H_0(\omega)$ and $H_1(\omega)$. Any linear filtering effects before A/D conversion are lumped into the CTF, including static gain, sampling time shift, pole-zero effect, etc. Assuming the bit-resolution is high, quantization effects are ignored.

Normalization with respect to the first channel yields Figure 4.1(c), where the correction digital filters $F_0(e^{j\omega})$ and $F_1(e^{j\omega})$ are also shown. This normalization clarifies we are interested only in channel mismatches, disregarding common linear time-invariant (LTI) filtering. There are two justifications for this: first, an LTI system does not create distortion sidebands, and second, common filtering due to CTF is acceptable in most cases. Now, the normalized CTF $H(\omega) \equiv H_1(\omega)/H_0(\omega)$ fully characterizes the general linear mismatches between the two channels.

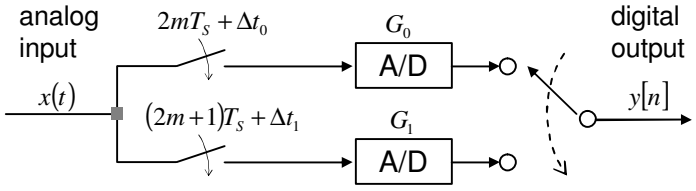

(a) Actual system

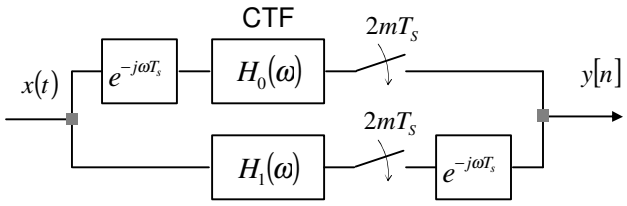

(b) Equivalent system

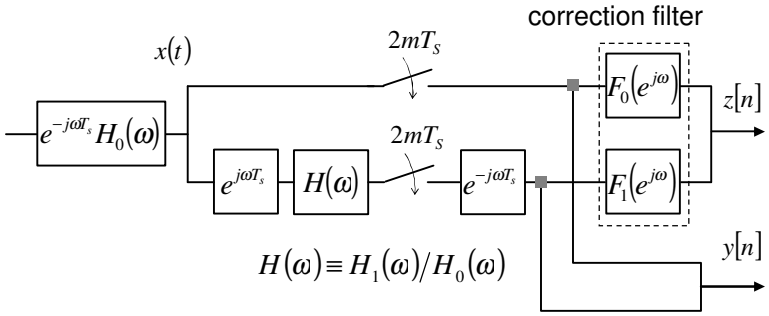

(c) Normalized system with correction filter bank

Figure 4.1: $M = 2$ TIADC system model. $z[n]$ and $y[n]$ are corrected and uncorrected TIADC output, respectively.

4.1.1 Parameterized Filter Bank Model

The system in Figure 4.1(c) can be regarded as an $M = 2$ filter bank, with analysis and synthesis filter bank equal to the analog and digital filters, respectively. The alias component (AC) matrix for each bank is then defined as

$$\begin{aligned}
\mathbf{H_{AC}}(\omega, \mathbf{p}^*) &= \begin{pmatrix} 1 & H(\omega, \mathbf{p}^*) \\ 1 & -H(\omega - \omega_s/2, \mathbf{p}^*) \end{pmatrix} \begin{pmatrix} 1 & 0 \\ 0 & e^{j\omega T_s} \end{pmatrix} \\
\mathbf{F_{AC}}(e^{j\omega}, \widetilde{\mathbf{p}}) &= \begin{pmatrix} F_0(e^{j\omega}, \widetilde{\mathbf{p}}) & F_1(e^{j\omega}, \widetilde{\mathbf{p}}) \\ F_0(e^{j(\omega-\omega_s/2)}, \widetilde{\mathbf{p}}) & -F_1(e^{j(\omega-\omega_s/2)}, \widetilde{\mathbf{p}}) \end{pmatrix} \begin{pmatrix} 1 & 0 \\ 0 & e^{-j\omega T_s} \end{pmatrix}. \\
& \qquad (0 \le \omega < \omega_s/2)
\end{aligned} \tag{4.1}$$

Note that $\mathbf{H_{AC}}$ and $\mathbf{F_{AC}}$ is a function of $\mathbf{p}^*$ and $\widetilde{\mathbf{p}}$ which is an actual and estimated mismatch parameter vector, respectively. The perfect reconstruction condition is

$$\mathbf{H_{AC}}\mathbf{F_{AC}^T} = 2\mathbf{I}, \tag{4.2}$$

which means that the entire system in Figure 4.1(c) reduces to an LTI system with no aliasing error.

4.1.2 Correction Filter Calculation

Equation (4.2) suggests that the correction filter, given mismatch estimate$\widetilde{\mathbf{p}}$, should be designed as

$$\mathbf{F_{AC}}(e^{j\omega}, \widetilde{\mathbf{p}}) = 2\mathbf{H_{AC}^{-T}}(\omega, \widetilde{\mathbf{p}}), \tag{4.3}$$

where $\mathbf{H_{AC}}(\omega, \widetilde{\mathbf{p}})$ is the AC matrix of a hypothetical analysis filter bank (assumed to be invertible),

$$\mathbf{H_{AC}}(\omega, \widetilde{\mathbf{p}}) = \begin{pmatrix} 1 & H(\omega, \widetilde{\mathbf{p}}) \\ 1 & -H(\omega - \omega_s/2, \widetilde{\mathbf{p}}) \end{pmatrix} \begin{pmatrix} 1 & 0 \\ 0 & e^{j\omega T_s} \end{pmatrix}. \tag{4.4}$$

$H(\omega, \widetilde{\mathbf{p}})$ is the estimated CTF parameterized by mismatch estimation $\widetilde{\mathbf{p}}$. The correction filters can be designed as follows: First, specify $H(\omega, \widetilde{\mathbf{p}})$ using the current estimation $\widetilde{\mathbf{p}}$, second, build $\mathbf{H_{AC}}$ using (4.4), third, invert it to obtain $\mathbf{F_{AC}}$ using (4.3), and finally obtain the time-domain impulse response using any conventional filter design method (e.g. frequency sampling, least-squares, etc).

$$\begin{aligned} f_0[n, \widetilde{\mathbf{p}}] &= \text{IDFT}\left(F_0(e^{j\omega}, \widetilde{\mathbf{p}})\right), \\ f_1[n, \widetilde{\mathbf{p}}] &= \text{IDFT}\left(F_1(e^{j\omega}, \widetilde{\mathbf{p}})\right). \end{aligned} \tag{4.5}$$

In (4.5), IDFT$(\cdot)$ is the inverse discrete Fourier transform operator. $f_0[n, \widetilde{\mathbf{p}}]$'s and $f_1[n, \widetilde{\mathbf{p}}]$'s are correction filter taps, whose combined output is the mismatch-corrected TIADC output in Figure 4.1(c).

So far, we have not assumed any specific parameterization of $H(\omega, \mathbf{p}^*)$ or $H(\omega, \widetilde{\mathbf{p}})$ (and $h[n, \mathbf{p}^*]$ or $h[n, \widetilde{\mathbf{p}}]$ thereof). The proposed system configuration in

Figure 4.1(c) and the derivation of correction filter in (4.5) is completely general and capable of generalized mismatch correction. The traditional gain-timing model can be handled as a special case. One important question remains: how to model or parameterize CTF as a function of mismatch parameters.

4.2 Polynomial Mismatch Modeling

In general, the modeling of channel mismatches should be application-specific; different analog front-ends will exhibit different mismatch behaviors. The best mismatch modeling will be physics-based, such that a small number of intrinsic parameters provide a good global fit to actual mismatch responses.

Among many possible parameterizations, polynomial approximation in polar coordinate has desirable properties in particular. First, under WSS input and small mismatch assumption, it guarantees unique parameter identification under mild conditions, as will be shown in the following section. Second, polynomial modeling can closely approximate arbitrary linear transfer functions if they are smooth and continuous within the band of interest (See e.g. Figure 2.6 and Figure 3.7). Last, the traditional static gain and timing mismatch can be readily handled as a special case of polynomial modeling.

Consider magnitude-phase decomposition of channel response, omitting dependency on mismatch parameters $\mathbf{p}^*$ or $\widetilde{\mathbf{p}}$ for simplicity,

$$H(\omega) = (1 + g(\omega))\, e^{j\phi(\omega)}, \tag{4.6}$$

where $g(\omega)$ and $\phi(\omega)$ is general gain and phase mismatch, respectively. Under small-mismatch assumption,

$$H(\omega) \approx 1 + g(\omega) + \phi(\omega). \tag{4.7}$$

Representing $g(\omega)$ and $\phi(\omega)$ as a frequency polynomial,

$$\begin{aligned} g(\omega) &= \sum_{k=0}^{Q} a_k \omega^k, \\ \phi(\omega) &= \sum_{k=0}^{Q} b_k \omega^k. \end{aligned} \tag{4.8}$$

It is assumed $g(\omega)$ and $\phi(\omega)$ has the same order, Q, for simplicity, but they can be of a different order as well.

4.3 Stationarity-Based Blind Multi-Parameter Estimation

The proposed blind estimation method in this chapter is based on the assumption that the TIADC input is WSS [56, 57]. If channel mismatches are present, the TIADC output is not WSS in general. The blind algorithm adjusts mismatch estimates to restore WSS property at the TIADC output.

Let $R_y[n,m] \equiv E[y[n]y[m]]$ and $R_z[n,m] \equiv E[z[n]z[m]]$ be the autocorrelation of uncorrected and corrected TIADC output, respectively (Figure 4.1(c)). It can be shown that R_z is periodic with respect to a common shift, due to the periodic channel switching, satisfying

$$R_z[n,m] = R_z[n+2, m+2], \quad \text{for all } n \text{ and } m. \tag{4.9}$$

If channel mismatch is present, R_z is generally (but not necessarily) shift-dependent,

$$R_z[n,m] \neq R_z[n+1, m+1], \quad \text{for some } n \text{ and } m. \tag{4.10}$$

It follows from (4.9) and (4.10) that $R_z[n,m]$ is completely specified by $R_z[u,0]$ and $R_z[u+1,1]$. The TIADC output $z[n]$ will become WSS if and only if $R_z[u,0]$=$R_z[u+1,1]$. Therefore, the optimum mismatch parameter $\widetilde{\mathbf{p}}_{\mathbf{opt}}$ can be obtained by the following minimization,

$$\widetilde{\mathbf{p}}_{\mathbf{opt}} = \arg\min_{\widetilde{\mathbf{p}}} J, \tag{4.11}$$

where the error measure J is defined as

$$J \equiv \sum_{u=0}^{U_{max}} \left(R_z[u+1,1] - R_z[u,0]\right)^2. \tag{4.12}$$

U_{max} is the maximum time lag to consider. Equation (4.12) can also be written in terms of cyclic correlation,

$$J \equiv \sum_{u=0}^{U_{max}} \left(R_z^{\frac{1}{2}}[u]\right)^2. \tag{4.13}$$

Minimization of (4.11) can be realized in many different ways. For example, if given enough computational power, exhaustive search can be performed over a single batch of data. Otherwise, gradual descent to the minimum over multiple batches may also be attempted with reduced computational cost (but with slower convergence). Depending on the implementation, observation of either corrected or uncorrected output may be more convenient than the other (i.e. $z[n]$ or $y[n]$ in Figure 4.1(c), respectively)

4.4 Uniqueness of Solution

Regading the optimum estimate obtained by (4.11), the following question needs to be answered: *Is the solution unique?* Equivalently, *under what conditions does* $J = 0$ *imply* $\widetilde{\mathbf{p}}_{\mathbf{opt}} = \mathbf{p}^*$*?* To answer this question, consider the cyclic spectral density $S_y^{1/2}(\omega)$ (i.e. Fourier transform of $R_y^{1/2}[u]$. See Section 3.2 for review of cyclostationary random process). It can be shown that $S_y^{1/2}(\omega)$ is written as

$$\begin{aligned} S_y^{1/2}(\omega) = S_x^0(\omega) \left(\widetilde{H}^*(\omega) - H^*(\omega)\right) \left(H(\omega) + \widetilde{H}(\omega - \omega_s/2)\right) \\ + S_x^0(\omega - \omega_s/2) \left(\widetilde{H}(\omega - \omega_s/2) - H(\omega - \omega_s/2)\right) \\ \cdot \left(\widetilde{H}^*(\omega) + H^*(\omega - \omega_s/2)\right). \end{aligned} \tag{4.14}$$

One can rewrite CTF's in a polar form, and apply small-mismatch assumption to yield

$$\begin{aligned} H(\omega) &= (1+g(\omega))\, e^{j\phi(\omega)} \approx 1 + g(\omega) + j\phi(\omega), \\ \widetilde{H}(\omega) &= (1+\widetilde{g}(\omega))\, e^{j\widetilde{\phi}(\omega)} \approx 1 + \widetilde{g}(\omega) + j\widetilde{\phi}(\omega). \end{aligned} \tag{4.15}$$

Representing each error term in (4.15) as a Q-th order polynomial,

$$\begin{aligned} g(\omega) &= \sum_{k=0}^{Q} a_k \omega^k, \quad \phi(\omega) = \sum_{k=0}^{Q} b_k \omega^k, \\ \widetilde{g}(\omega) &= \sum_{k=0}^{Q} \widetilde{a}_k \omega^k, \quad \widetilde{\phi}(\omega) = \sum_{k=0}^{Q} \widetilde{b}_k \omega^k. \end{aligned} \tag{4.16}$$

Thus, $\mathbf{p}^* = [a_0\ a_1\ ...\ a_Q\ b_0\ b_1\ ...\ b_Q]^T$ and $\widetilde{\mathbf{p}}^* = [\widetilde{a}_0\ \widetilde{a}_1\ ...\ \widetilde{a}_Q\ \widetilde{b}_0\ \widetilde{b}_1\ ...\ \widetilde{b}_Q]^T$. Plugging (4.15)–(4.16) into (4.14), and taking real and imaginary part, one can show that, to a first-order approximation, $S_y^{1/2}(\omega) \equiv 0$ is equivalent to

$$\begin{aligned} \mathbf{W}\mathbf{e_g} &= \mathbf{0}, \\ \mathbf{W}\mathbf{e}_\phi &= \mathbf{0}, \end{aligned} \tag{4.17}$$

where $\mathbf{W}$ and coefficient error vectors $\mathbf{e_g}$ and $\mathbf{e}_\phi$ are defined as

$$\begin{aligned} [\mathbf{W}]_{n,m} &= S_y^0(\omega_n)\omega_n^m + S_y^0(\omega_n - \omega_s/2)\,(\omega_s/2 - \omega_n)^m\,, \\ [\mathbf{e_g}]_{n,1} &= \widetilde{a}_n - a_n, \\ [\mathbf{e}_\phi]_{n,1} &= \widetilde{b}_n - b_n. \\ & \qquad (0 \le n \le F-1,\ \ 0 \le m \le Q,\ \ 0 < \omega_n < \omega_s/2) \end{aligned} \tag{4.18}$$

ω_n's are F frequency points where either $S_y^0(\omega_n)$ or $S_y^0(\omega_n - \omega_s/2)$ is nonzero (hence positive). If W has at least $(Q+1)$ linearly independent rows, then the

only solution of (4.17) is $\mathbf{e_g} = \mathbf{0}$ and $\mathbf{e}_\phi = \mathbf{0}$, which means that $\widetilde{\mathbf{p}}_{\mathbf{opt}} = \mathbf{p}^*$. Obviously, the input needs to have at least $(Q+1)$ spectral tones, and this will enable identification of up to $2(Q+1)$ real-valued mismatch parameters. As the input spectrum becomes richer, it is more likely that at least $(Q+1)$ rows are independent with each other, guaranteeing unique parameter identification.

For theoretical purpose, consider the following assumption: The TIADC input has at least $(Q+1)$ distinct spectral tones at ω_n's, such that only one of $S_y^0(\omega_n)$ or $S_y^0(\omega_n - \omega_s/2)$ is nonzero. Under this minimal asymmetric tone (MAT) assumption, (4.17) simplifies to

$$\begin{aligned} \mathbf{V}\mathbf{e_g} &= \mathbf{0}, \\ \mathbf{V}\mathbf{e}_\phi &= \mathbf{0}, \end{aligned} \tag{4.19}$$

where $\mathbf{V}$ is now a diagonally weighted vandermonde matrix,

$$[\mathbf{V}]_{n,m} = S_y^0(\omega_n)\omega_n^m. \tag{4.20}$$

V is nonsingular if and only if ω_n's are distinct. Therefore, the MAT condition strictly guarantees unique mismatch identification. The MAT condition can be met if the input spectrum has a small unoccupied region (not in a mirror symmetry) across $f = 1/4f_s$. Since the probability of W being singular has zero measure, W will be almost always nonsingular even if MAT is not met, as long as the input spectrum is rich enough.

4.5 Simulation Results

In this section, a numerical example is presented to demonstrate the proposed generalized blind method. The $M = 2$ TIADC under simulation has 12-bit resolution, and each channel has a single pole around $0.6\omega_s$. Mismatch parameters are 3% static gain error, 0.6% sampling time error and 2% pole location mismatch. The input signal has three equal-magnitude tones at $0.065\omega_s$, $0.185\omega_s$ and $0.405\omega_s$. It is readily seen that the MAT condition (Section 4.4) is satisfied with Q up to 2.

A batch of $N = 100,000$ samples of uncorrected TIADC output $y[n]$ is time-averaged to obtain R_y. Next, R_y goes through double convolution with correction filters to calculate R_z, autocorrelation of corrected TIADC output. R_z is then passed to a minimizer routine to find out the best mismatch estimate ((4.12)). The number of tap for each correction filter is $L = 61$, and the maximum time lag to consider is $U_{max} = 10$.

Two representative mismatch models are tested for comparison: conventional gain-timing model and 2nd-order polynomial model ($Q = 2$). Figure 4.2(a) and Figure 4.2(b) each compares the true CTF and its estimates with either mismatch model. Dotted lines are true magnitude and phase response, where the curvature is due to the pole location mismatch. Solid lines correspond to the best esti-

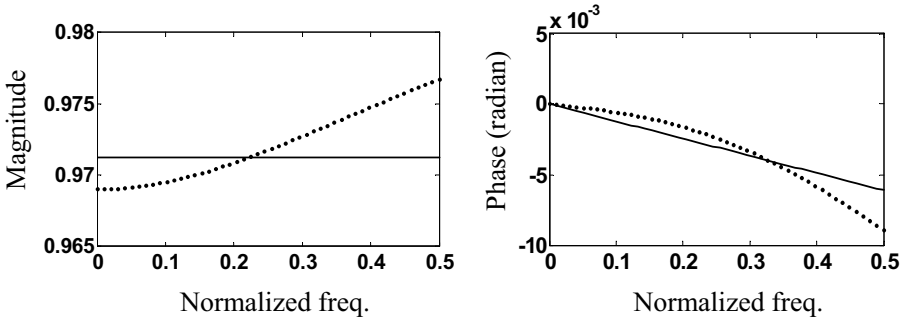

(a) Dotted line: actual mismatch. Solid line: Estimates of gain-timing model

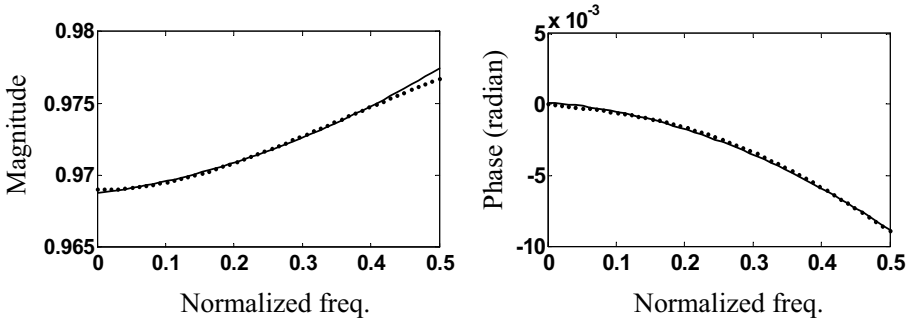

(b) Dotted line: actual mismatch. Solid line: Estimates of generalized mismatch model (2nd-order polynomial)

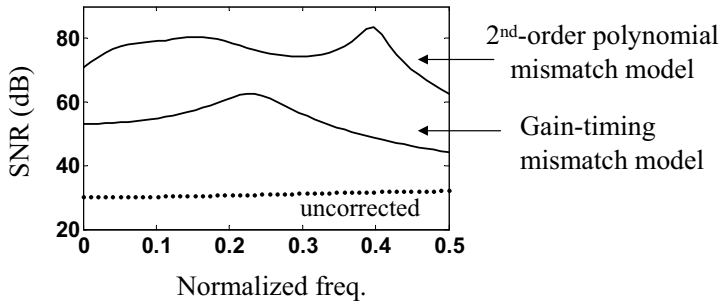

(c) Comparison of SNR improvement

Figure 4.2: Comparison of correction results from gain-timing model and generalized model. It is clearly seen that the generalized model provides a superior match to the actual mismatch response, and hence greater SNR improvement than gain-timing model.

mation, which is also the best fit to the true responses weighted by the input spectral density. Second-order modeling gives a good match, and the limitation of gain-timing model is clearly seen. Mismatch-limited SNR is closely approximated by $1/\left|H(\omega,\widetilde{\mathbf{p}})-H(\omega,\mathbf{p}^*)\right|$ which is plotted in Figure 4.2(c). Up to 35 dB of improvement is observed as a result of generalized mismatch modeling

4.6 Efficient Adaptive Implementation

The correction and estimation of generalized mismatches is discussed in Section 4.3 and Section 4.1.2 in a general context. In this section, an efficient implementation of the proposed method is introduced, exploiting polynomial representation of mismatch. First, consider simpler correction filter structure by introducing an appropriate normalization.

4.6.1 Correction Filter Normalization

From (4.3) and (4.4), $\mathbf{F_{AC}}$ can be shown to be

$$\begin{aligned}\mathbf{F_{AC}}(e^{j\omega},\widetilde{\mathbf{p}}) &= \frac{2}{H(\omega,\widetilde{\mathbf{p}})+H(\omega-\omega_s/2,\widetilde{\mathbf{p}})} \\ &\cdot\begin{pmatrix} H(\omega-\omega_s/2,\widetilde{\mathbf{p}}) & 1 \\ H(\omega,\widetilde{\mathbf{p}}) & -1 \end{pmatrix}\begin{pmatrix} 1 & 0 \\ 0 & e^{-j\omega T_s} \end{pmatrix}.\end{aligned} \tag{4.21}$$

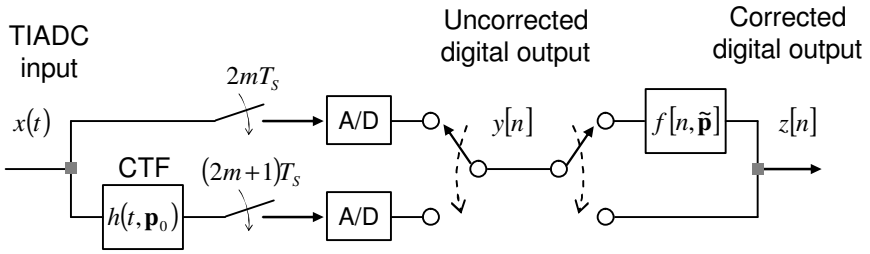

Figure 4.3: $M = 2$ TIADC system with a normalized correction filter.

One can ignore the common filtering factor $2/\left(H(\omega, \widetilde{\mathbf{p}}) + H(\omega - \omega_s/2, \widetilde{\mathbf{p}})\right)$ (valid under small-mismatch assumption). Then, it is readily seen that correction filters are given by

$$\begin{aligned} F_0(e^{j\omega}, \widetilde{\mathbf{p}}) &= H(\omega - \omega_s/2, \widetilde{\mathbf{p}}), \\ F_1(e^{j\omega}, \widetilde{\mathbf{p}}) &= 1, \end{aligned} \tag{4.22}$$

suggesting that only one non-trivial filter is required, $F_0(e^{j\omega}, \widetilde{\mathbf{p}})$.

Let $h(t)$ and $f[n]$ be the impulse response of $H(\omega, \widetilde{\mathbf{p}})$ and $F_0(e^{j\omega}, \widetilde{\mathbf{p}})$, respectively. Then, $f[n]$ directly follows from (4.22),

$$f[n] = (-1)^n \, h(nT_s). \tag{4.23}$$

The equivalent TIADC system with a normalized correction filter is shown in Figure 4.3 ($h[n] \equiv h(nT_s)$).

4.6.2 Analytic Filter Calculation

Assuming a polynomial representation of generalized mismatches, as discussed in Section 4.2, one can explicitly represent the correction filter coefficients $f[n]$ in terms of polynomial coefficients. This enables bypassing of time-consuming numerical operations such as matrix inversion, time-frequency domain transformation, etc, significantly increasing numerical efficiency.

From (4.7), (4.8), and (4.23), correction filter coefficients $f[n]$ can be written as a function of polynomial coefficients (for $Q = 2$)

$$f[n] = (-1)^n \left(\delta[n] + \sum_{k=0}^{2} a_k h_k[n] + \sum_{k=0}^{2} b_k h_{k+3}[n] \right), \tag{4.24}$$

where subsequences $h_k[n]$'s are defined as

$$\begin{aligned} h_0[n] &= \delta[n], \\ h_1[n] &= \frac{\pi}{2}\delta[n] + \frac{(-1)^n - 1}{n^2\pi}, \\ h_2[n] &= \frac{\pi^2}{3}\delta[n] + \frac{2(-1)^n}{n^2}, \\ h_3[n] &= \frac{(-1)^n - 1}{n\pi}, \\ h_4[n] &= \frac{(-1)^n}{n}, \\ h_5[n] &= \frac{2\left(1 - (-1)^n\right)}{n^3\pi} + \frac{\pi(-1)^n}{n}. \end{aligned} \tag{4.25}$$

Equation (4.24)–(4.25) define $Q = 2$ parameterization of $f[n, \widetilde{\mathbf{p}}]$, where $\widetilde{\mathbf{p}} = [\widetilde{a}_0\ \widetilde{a}_1\ \widetilde{a}_2\ \widetilde{b}_0\ \widetilde{b}_1\ \widetilde{b}_2]^T$. Extension to $Q > 2$ is straightforward.

4.6.3 Analytic Error Measure and Gradient

Now, using (4.24)–(4.25), the error measure (4.12) as well as its gradient can be obtained in an analytical form. First, represent $R_z[u,0]$ and $R_z[u+1,1]$ in terms of polynomial mismatch coefficients

$$\begin{aligned} R_z[u,0] = & \sum_{k=-L}^{L}\sum_{l=-L}^{L} f[k]f[l]I_e[u-k]I_e[-l]R_y[u-k,-l] \\ & + \textstyle\sum_{k=-L}^{L} f[k]I_o[u]I_e[-k]R_y[u,-k], \end{aligned} \tag{4.26}$$

$$\begin{aligned} R_z[u+1,1] = & \sum_{k=-L}^{L}\sum_{l=-L}^{L} f[k]f[l]I_e[u+1-k]I_e[1-l]R_y[u+1-k,1-l] \\ & + \sum_{k=-L}^{L} f[k]I_e[u+1-k]R_y[u+1-k,1] \\ & + \sum_{k=-L}^{L} f[k]I_o[u+1]I_e[1-k]R_y[u+1,1-k] \\ & + R_y[u+1,1]I_o[u+1]. \end{aligned} \tag{4.27}$$

In (4.26)–(4.27), $R_y[n,m]$ is the autocorrelation measured at the uncorrected TIADC output $y[n]$. $(2L+1)$ is the number of $f[n]$ taps. $I_e[n] = 1$ if n is even, 0 if not. Similarly, $I_o[n] = 1$ for odd n, and 0 otherwise.

The derivative of autocorrelation coefficients similarly follows.

$$\begin{aligned} \frac{\partial R_z[u,0]}{\partial \widetilde{p}_m} = & \sum_{k=-L}^{L}\sum_{l=-L}^{L} \left(h_m[k]f[l] + f[k]h_m[l]\right) \\ & \cdot I_e[u-k]I_e[-l]R_y[u-k,-l] \\ & + \sum_{k=-L}^{L} h_m[k]I_o[u]I_e[-k]R_y[u,-k], \end{aligned} \tag{4.28}$$

$$\begin{aligned}\frac{\partial R_z[u+1,1]}{\partial \widetilde{p}_m} = & \sum_{k=-L}^{L}\sum_{l=-L}^{L}\left(h_m[k]f[l]+f[k]h_m[l]\right) \\ & \cdot I_e[u+1-k]I_e[1-l]R_y[u+1-k,1-l] \\ & + \sum_{k=-L}^{L} h_m[k]I_e[u+1-k]R_y[u+1-k,1], \\ & + \sum_{k=-L}^{L} h_m[k]I_o[u+1]I_e[1-k]R_y[u+1,1-k],\end{aligned} \tag{4.29}$$

where $\widetilde{p}_m$ is m-th mismatch parameter in $\widetilde{\mathbf{p}}$.

4.6.4 Steepest Descent Iteration

Finally, the minimization of J in (4.12) can be performed by the following iteration rule,

$$\widetilde{p}_m^{(i+1)} = \widetilde{p}_m^{(i)} - \alpha \left.\frac{\partial J}{\partial \widetilde{p}_m}\right|_{\widetilde{p}_m=\widetilde{p}_m^{(i)}}, \tag{4.30}$$

where the error gradient $\partial J/\partial \widetilde{p}_m$ is obtained by differentiating (4.12) and substituting (4.26)–(4.27) and (4.28)–(4.29)

$$\frac{\partial J}{\partial \widetilde{p}_m} = 2\sum_{u=0}^{U_{max}}\left(R_z[u+1,1]-R_z[u,0]\right)\left(\frac{\partial R_z[u+1,1]}{\partial \widetilde{p}_k}-\frac{\partial R_z[u,0]}{\partial \widetilde{p}_k}\right), \tag{4.31}$$

where $\widetilde{p}_m^{(i)}$ is the estimate $\widetilde{p}_m$ at i-th iteration. α is a convergence parameter ($\alpha \ll 1$). Note the calculation of gradient by (4.26)–(4.27) and (4.28)–(4.29) does not involve numerically intensive operations such as matrix inversion or transformation between time- and frequency-domain. The required calculation is mostly

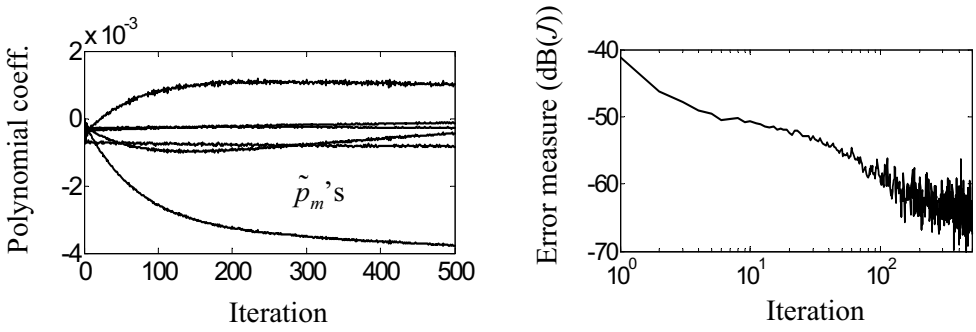

(a) Convergence of polynomial coefficients (b) Error measure history

Figure 4.4: Convergence of mismatch parameters and error measure using adaptive implementation of the generalized blind correction.

double-convolution, therefore further reduction in complexity would be possible using fast Fourier-transform operation

4.6.5 Simulation Example

In this section, a simulation example is given to demonstrate the efficient implementation of generalized blind correction. The $M = 2$ TIADC array under simulation has 12-bit resolution with 0.4% static gain and 0.6% sampling time mismatch. Each channel has a single pole around $0.6\omega_s$, and the mismatch in pole location is 2%. The magnitude and phase of CTF are modeled as a $Q = 2$ polynomial. The input signal has three tones with equal magnitudes at $0.065\omega_s$, $0.185\omega_s$ and $0.405\omega_s$. This particular signal enables unique polynomial identification up to $Q = 2$ (Section 4.4).

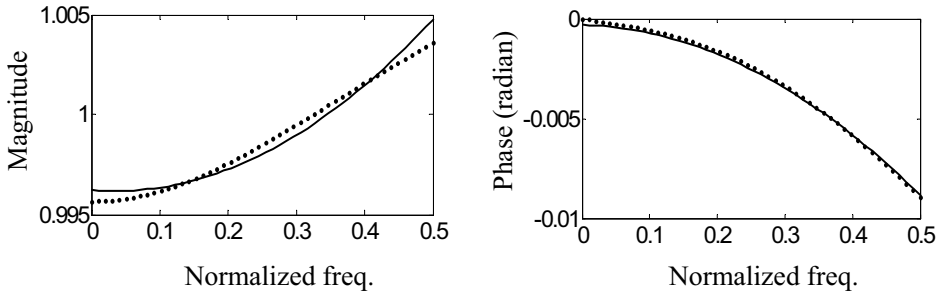

(a) Dotted line: actual mismatch. Solid line: Estimates of generalized mismatch model (2nd-order polynomial)

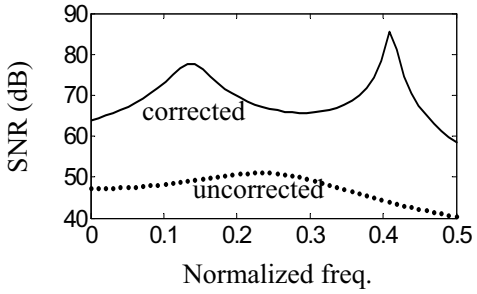

(b) SNR improvement

Figure 4.5: Comparison of correction results from gain-timing model and generalized model using adaptive algorithm.

Total 500 iterations are performed according to the descent rule (4.30). For each iteration, R_y is obtained by time-averaging $N = 100,000$ uncorrected output samples. $L = 20$ and $U_{max} = 5$. Figure 4.4 shows a convergence plot for parameter estimate $\widetilde{p}_m$ and error measure J, respectively. Figure 4.5(a) compares the true and estimated CTF. A close agreement is seen, which obviously the simple gain-timing model cannot provide. Finally, mismatch-limited SNR is estimated by $1/\left|H(\omega,\widetilde{\mathbf{p}}) - H(\omega,\mathbf{p}^*)\right|$, and shows 15–30 dB improvement after calibration in Figure 4.5(b).

4.7 Conclusions

In this chapter, it is proposed and demonstrated that generalized mismatch errors can be *blindly* identified and corrected, achieving significant SNR and SFDR improvement (15–35 dB), for an $M = 2$ TIADC under realistic assumptions. Parameterized filter banks and cyclostationary spectral analysis is a key to the algorithm implementation and theoretical analysis, respectively.

Polynomial approximation in polar coordinate has been used for the present study, but in principle other parameterizations are also possible. The best parameterization will be application specific. It will capture the physics of mismatches with a minimal number of parameters while systematically avoiding the possibility

of false correction. The proposed approach and theoretical framework can also be applied to general sampling networks, as well as A/D conversion systems, where the sampler performance is sensitive to periodic patterning artifacts.

Chapter 5

Mismatch Correction for TIADCs: Mixed-Domain Blind Method

Currently known techniques for TIADC mismatch correction can be categorized into training (foreground) [11, 20] and blind (background) methods [24, 27–29, 48–50, 56–63]. As discussed before, training methods are suitable for high-resolution application in general, since they are capable of correcting general linear mismatches [11], but at the cost of suspension of data acquisition during each calibration. They are also subject to post-calibration detuning due to temperature variation, aging, etc [11]. Blind methods, on the other hand, use normal input signals for calibration purpose, and therefore do not require dedicated calibration period. Slowly time-varying errors may also be tracked. There have been proposed a variety of blind methods with different accomplishments and limitations. One group of techniques performs error detection and correction entirely in the

digital domain [29, 48–50, 58], as illustrated in Figure 5.1(b). Another class of techniques use both analog and digital domain [24, 27, 28, 59, 62].

Previous mixed-domain methods typically involve special analog signal processing (e.g. adding a known signal to the input as in Figure 5.1(c)) to facilitate mismatch estimation, which may potentially compromise input signal integrity. Purely digital techniques keep the analog signal path intact, but their computational cost is highly demanding. This is partly due to the complex parameter search algorithm, but mostly due to digital correction of sampling time delay, since matrix inversion or transformation between the time and frequency domains is usually required for correction filter calculation. Further, the resulting correction filter is long ($\mathrm{sinc}(t)$ decays only as $1/t$), increasing hardware cost and complexity. Depending on blind correction algorithms, the estimation of timing error may also be computationally complex. For both classes of techniques, special assumptions are necessary (e.g. reduced input bandwidth, limited number of TIADC channels, wide-sense stationarity, or their combination, etc) to make the problem of blind estimation solvable. Full-digital techniques tend to require stronger assumptions, thus are more restrictive than mixed-domain methods. Using an extra ADC may provide a convenient calibration reference, but the analog input path is subject to switching, raising concerns about the input signal integrity.

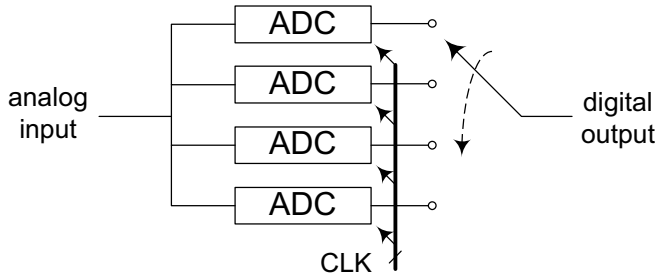

(a) $M = 4$ TIADC system

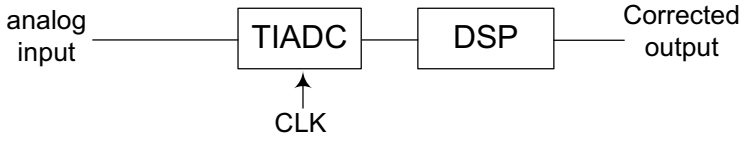

(b) Full digital-domain blind correction method

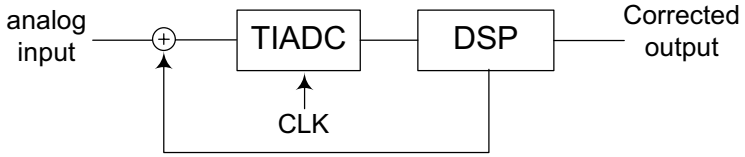

(c) Conventional mixed-domain method with analog input pre-processing

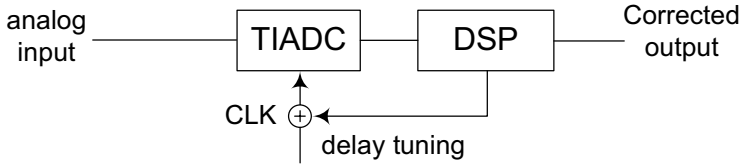

(d) Proposed mixed-domain method with sampling clock tuning

Figure 5.1: A $M = 4$ TIADC system with mismatch correction system

The above discussion naturally leaves us one interesting option in the mixed-domain: timing error correction in the analog domain by directly tuning sampling clocks (Figure 5.1(d)). This obviates long digital filters as well as their online calculation for timing correction. Additional benefit is that, now timing correction is ideal over multiple Nyquist zones. In contrast, a single set of digital filters can only provide approximate timing correction (e.g. limited usable bandwidth, in-band ripples, etc) over a single Nyquist zone. A reliable blind estimation method needs to be developed to close the feedback loop, preferably with weaker working assumptions to allow application to the widest range of signals. Since the clock tuning circuitry is subject to environmental changes, drift, etc (as with other analog circuits), the importance of a reliable estimation algorithm is emphasized.

In this chapter, an entirely new mixed-domain blind method is proposed, with complete theory and experimental results, in accordance with the above discussion. Dramatically reduced computational complexity and exceptionally wide applicability are among the contributions of the proposed method. The proposed blind method is based on the assumption that the input signal is wide-sense stationary (WSS). Under the input WSS assumption, the mismatch estimates are guaranteed to converge to true parameters. However, the proposed method is equally effective with most commonly-arising signals which do not meet the WSS constraint. In particular, the algorithm functions with sinusoidal input signals. No

further restriction is necessary other than the input WSS condition. Specifically, the TIADC can have an arbitrary number of channels, and the input spectrum can cover the full Nyquist bandwidth. In fact, the proposed blind method works in any Nyquist zone.

Section 5.1 describes the system model. Section 5.2 introduces the proposed error detection method, and Section 5.3 develops its adaptive implementation for parameter estimation. Section 5.4 discusses experimental results, and Section 5.5 gives conclusion.

5.1 System Model

Figure 5.2 shows a block diagram of the $M = 4$ TIADC structure with the proposed mismatch correction scheme. Each of four sub-converters successively samples the analog input signal $x(t)$ every $4T_s$ such that the overall sampling rate is f_s $(=1/T_s)$. Listed below are pertinent assumptions and clarifications with references to Figure 5.2.

- The input $x(t)$ is WSS and bandlimited from dc to $1/2f_s$. No further information about $x(t)$ is known.
- The sub-converters' resolution is sufficiently high enough for ADC quantization errors to be ignored.

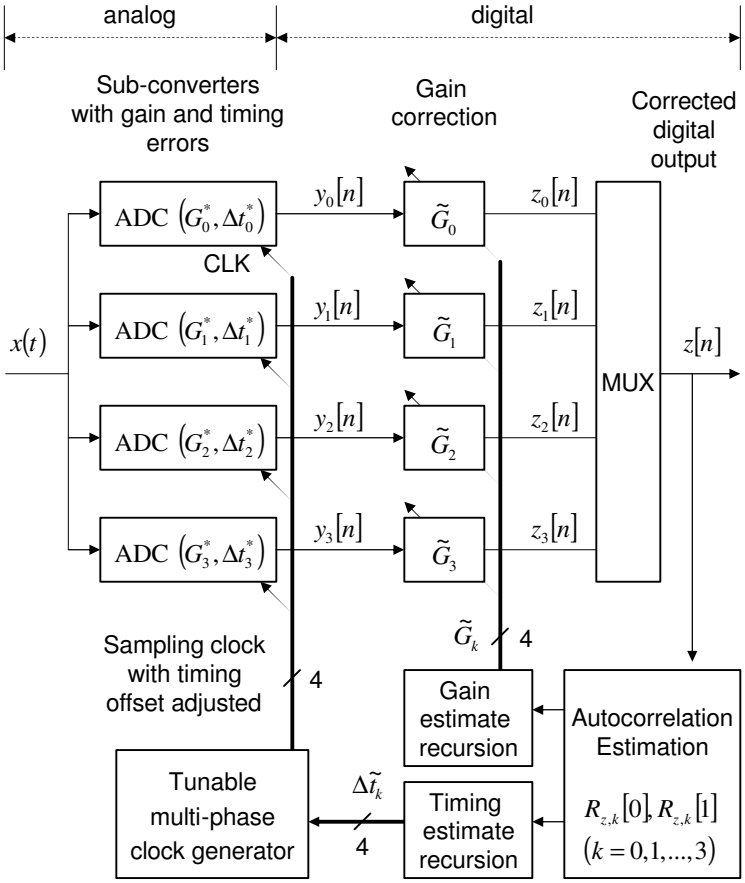

Figure 5.2: A $M = 4$ TIADC system with the proposed mixed-domain mismatch correction scheme.

- The mismatch in sub-converter dc offsets is independently corrected by first measuring and subsequently subtracting the time-average sub-converter outputs.
- The k-th channel sub-converter has intrinsic gain G_k^* and sampling time error Δt_k^* which are unknown.
- The estimate of the intrinsic gain and sampling time errors is $\widetilde{G}_k$ and $\Delta\widetilde{t}_k$, respectively.
- Correction of sampling time mismatches is achieved by tuning individual sampling clock to the estimate $\Delta\widetilde{t}_k$.
- Correction of gain error is performed by digitally dividing the sub-converter output by the gain estimate $\widetilde{G}_k$.
- Residual mismatch error is defined as the difference between intrinsic and estimated parameters.
- Finally, the magnitude of intrinsic mismatches is small. The precise interpretation will be made clear in the context.

The output of the k-th sub-converter, $y_k[n]$, is

$$y_k[n] = G_k^* x\left((Mn+k)\,T_s + \Delta t_k^* - \Delta\widetilde{t}_k^*\right),$$

where M is the number of TIADC channels. After gain correction,

$$z_k[n] = \frac{y_k[n]}{\widetilde{G}_k}. \tag{5.1}$$

Therefore, the subsequence $z_k[n]$ is a scaled, time-shifted, and undersampled version of $x(t)$,

$$z_k[n] = \left(\frac{G_k^*}{\widetilde{G}_k^*}\right) x\left((Mn+k)\,T_s + \Delta t_k^* - \Delta\widetilde{t}_k^*\right). \quad (k = 0, 1, ..., M-1) \tag{5.2}$$

The overall TIADC output $z[n]$ is obtained by taking $z_k[n]$'s in a cyclic fashion as follows.

$$z[n] = z_n \bmod {}_M \left[\text{floor}\left(\frac{n}{M}\right)\right], \tag{5.3}$$

where floor(x) is the greatest integer smaller than or equal to x.

5.1.1 TIADC Mismatch Model

If there is no residual mismatch, it follows from (5.2) and (5.3) that

$$z[n] = x(nT_s),$$

i.e. perfect reconstruction of the input. Otherwise, $z[n]$ is modulated by residual gain or sampling time errors. In the frequency domain, this modulation manifests itself as frequency-shifted input spectra, i.e. aliasing error. Let $H_k(f)$ the linear time-invariant (LTI) frequency response of k-th channel (which includes static

gain and time delay as a special case). The spectrum of $z[n]$ consists of linearly weighted, frequency-shifted input spectra (Section 2.3),

$$Z\left(e^{j2\pi f}\right) = \sum_{m=0}^{M-1} c_m\left(f - \frac{m}{M}f_s\right) X\left(f - \frac{m}{M}f_s\right), \tag{5.4}$$

where $Z(e^{j2\pi f})$ and $X(f)$ are the Fourier transform of $z[n]$ and $x(t)$, respectively. The conversion gain $c_m(f)$'s are obtained by taking the discrete Fourier transform (DFT) of $H_k(f)$'s with respect to k,

$$c_m(f) = \mathrm{DFT}\left(H_k(f)\right) \quad m,k = 0,1,...,M-1. \tag{5.5}$$

If no mismatch, $H_k(f)$'s are all equal. The only nonzero DFT coefficient in the case is $c_0(f)$, average of $H_k(f)$'s, yielding the following alias-free output

$$\begin{aligned} Z\left(\right) &= c_0(f)X(f) \\ &= \left(\frac{1}{M}\sum_{k=0}^{M-1} H_k(f)\right) X(f). \end{aligned} \tag{5.6}$$

5.1.2 Adjacent-Channel Timing Offset

It will prove to be useful to use the adjacent-channel timing offset δ_k between two cyclically neighboring channels,

$$\delta_k \equiv \Delta t_k - \Delta t_{k+1}. \quad (k = 0,1,...,M-2) \tag{5.7}$$

δ_k's do not retain the common timing offset in sampling instance, but the timing mismatch information is still preserved. To retrieve Δt_k's from δ_k's (to drive

tunable sampling clock), therefore, another constraint is required. Two reasonable choices are

$$\Delta t_k = \sum_{n=0}^{k-1} \delta_n, \quad \text{assuming } \Delta t_0 = 0, \tag{5.8}$$

$$\Delta t_k = \sum_{n=0}^{k-1} \delta_n - \frac{1}{M} \sum_{m=0}^{M-2} (M-1-m)\, \delta_m, \quad \text{assuming } \sum_{k=0}^{M-1} \Delta t_k = 0. \tag{5.9}$$

Equation (5.8) puts global timing reference on the sampling instance of the first channel, while (5.9) takes channel average as a timing reference. The conversion (5.8) allows simpler implementation than (5.9). Further, no clock tuning is necessary for the first channel for (5.8). The conversion rule (5.9), however, evenly distributes timing error across M tunable clocks, and so their delay dynamic-range requirement is always smaller than (5.8). Timing conversion in this work follows (5.9).

5.2 Stationarity-Based Blind Method

In general, looking at the TIADC output alone does not uniquely determine converter mismatches, since there are many input-mismatch combinations that will yield the same TIADC output. It is necessary, therefore, to constrain the permissible input signal to a proper subset of all Nyquist-bandlimited signals. It is desirable that these constraints are weak to admit as large classes of signals as possible, but strong enough to enable blind mismatch detection. How to constrain

the input signal is an important question deserving attention, since this determines the practicality and complexity of the blind algorithm.

Among proposed approaches has been to constrain the input signal bandwidth in the frequency domain, inspired by the frequency-translation action of mismatch in (5.4). The unoccupied portion of the input spectrum plays the role of *aliasing detector* (hence, mismatch detector). Some recent techniques require a small fraction of extra bandwidth for aliasing detection, attempting to minimize input spectrum loss. While these frequency-domain techniques are theoretically sound, their practical application is not easy because of the following two problems. First, parameter estimation is highly sensitive to out-band noise: additive thermal noise, out-of-band interferers, signal harmonics, adjacent-channel residual power, etc. Any of these signal component will raise a *false alram* to the aliasing detector, resulting erroneous mismatch detection. Second, the boundary between signal band and aliasing-detection band must be accurately known a priori. Imprecise knowledge of the aliasing-detection band will again increase the chance of *false aliasing detection*.

In this work, blind parameter estimation is based on the assumption that the TIADC input is WSS. There is no bandwidth restriction on the TIADC input signal (other than the Nyquist sampling criterion) unlike frequency-domain approaches, so the problem of out-of-band interferers are automatically removed.

Let the TIADC input $x(t)$ a WSS signal. Then, its autocorrelation is given by

$$R_x(\tau) = E\left[x(t+\tau)x(t)\right], \text{ for all } t \text{ and } \tau.$$

Let $R_{z,k}[0]$ and $R_{z,k}[1]$ be the zero-lag and unit-lag autocorrelation coefficients of the TIADC output $z[n]$, respectively, referenced to k-th channel,

$$R_{z,k}[0] = E\left[z_k^2[n]\right], \tag{5.10}$$

$$R_{z,k}[1] = \begin{cases} E\left[z_k[n]z_{k+1}[n]\right], & k = 0, 1, ..., M-2 \\ E\left[z_k[n]z_0[n+1]\right]. & k = M-1 \end{cases} \tag{5.11}$$

These can be rewritten in terms of the input autocorrelation $R_x(\tau)$ by using (5.2),

$$R_{z,k}[0] = \left(\frac{G_k^*}{\widetilde{G}_k}\right)^2 R_x(0), \tag{5.12}$$

$$R_{z,k}[1] = \frac{G_k^* G^*_{(k+1) \bmod M}}{\widetilde{G}_k \widetilde{G}_{(k+1) \bmod M}} \left(R_x(T_s) + \left(\delta_k^* - \widetilde{\delta}_k\right) \left.\frac{dR_x}{d\tau}\right|_{\tau=T_s}\right). \tag{5.13}$$

The first-order approximation in (5.13) is valid if δ_k^* and $\widetilde{\delta}_k$ are much smaller than T_s. Note $R_{z,k}[0]$ is a function of only gain mismatch, while $R_{z,k}[1]$ depends on both gain and timing errors. The following important observations are made from (5.12) and (5.13).

1. *No residual mismatch condition*: If there is no residual mismatches, then $R_{z,0}[m]$=$R_{z,1}[m]$... =$R_{z,M-1}[m]$ $(m = 0, 1)$. In other words, $R_{z,k}[m]$'s are equalized across channels, and shift-independence has been attained.

2. *Equalized autocorrelation condition*: If all $R_{z,k}[m]$'s are equalized ($m = 0, 1$), then gain and timing estimates are equal to intrinsic ones up to a common scale factor and time delay, respectively, i.e. $\widetilde{G}_0/G_0^*=\widetilde{G}_1/G_1^*... =\widetilde{G}_{M-1}/G_{M-1}^*$, and $\Delta\widetilde{t}_0 - \Delta t_0^*=\Delta\widetilde{t}_1 - \Delta t_1^*... =\Delta\widetilde{t}_{M-1} - \Delta t_{M-1}^*$.

3. *Equivalence condition*: Therefore, to within common time delay and scaling, *the attainment of equalization of $R_{z,k}[0]$'s and $R_{z,k}[1]$'s is necessary and sufficient for perfect mismatch correction.*

The proof of *No residual mismatch condition* and *Equalized autocorrelation condition* directly follows from (5.12) and (5.13). The *Equivalence condition* is a key result which the proposed blind method is based on. The next section will develop actual implementation to achieve the output correlation equalization.

5.3 Adaptive Estimation Algorithm

Adaptive algorithm for the proposed blind estimation method is developed in this section. The goal is to achieve equalization of the zero-lag ($R_{z,k}[0]$) and unit-lag ($R_{z,k}[1]$) correlation coefficients. Convergence analysis is also presented. For adaptation to time-varying mismatch errors, the algorithm will be iterative in nature. Starting from an initial estimate, the calibration loop will gradually refine parameter estimates until the zero- and unit-lag output correlation coefficients

are all equalized. The equivalence result in Section 5.2 then guarantees that the estimates are equal to true parameters up to a common scale and time delay.

5.3.1 Empirical Output Autocorrelation

Calibration cycle starts with obtaining output autocorrelation coefficients $R_{z,k}[0]$'s and $R_{z,k}[1]$. Given a batch of sub-converter output $y_k[n]$, gain-corrected stream $z_k[n]$ is calculated from (5.1). Output correlation coefficients are then empirically obtained by

$$R_{z,k}^{(i)}[0] = \frac{1}{N}\sum_{n=0}^{N-1} z_k^{(i)}[n]^2, \tag{5.14}$$

$$R_{z,k}^{(i)}[1] = \begin{cases} \dfrac{1}{N}\displaystyle\sum_{n=0}^{N-2} z_k^{(i)}[n] z_{k+1}^{(i)}[n], & k = 0, 1, ..., M-2 \\ \dfrac{1}{N}\displaystyle\sum_{n=0}^{N-2} z_k^{(i)}[n] z_0^{(i)}[n+1], & k = M-1 \end{cases} \tag{5.15}$$

where the superscript indicates that the calculation is based on i-th iteration batch data. For simpler notation, this superscript will be dropped afterwards unless necessary for clarity.

5.3.2 Equalization Reference

Given the two sets of empirical correlation coefficients from (5.14) and (5.15), one can choose an appropriate equalization reference for each set against which empirical coefficients are compared. One of the sensible choices is the following

average coefficients,

$$R_{z,ref}[0] = \frac{1}{M}\sum_{k=0}^{M-1} \widetilde{G}_k^2 R_{z,k}[0], \tag{5.16}$$

$$R_{z,ref}[1] = \frac{1}{M}\sum_{k=0}^{M-1} R_{z,k}[1], \tag{5.17}$$

where $R_{z,ref}[0]$ and $R_{z,ref}[1]$ is the equalization reference for $R_{z,k}[0]$'s and $R_{z,k}[1]$'s, respectively. The reference coefficients in (5.16) and (5.17) are basically an average across channels, except for the weighting by gain estimate in (5.16). This weighting effectively prevents the common gain factor from drifting or unboundedly increasing over calibration cycles. In fact, $R_{z,ref}[0]$ is equal to the average correlation observed before digital gain correction, i.e. at $y_k[n]$. Using (5.16) is, however, more efficient than separately observing $y_k[n]$ and calculating its autocorrelation coefficients. After plugging (5.12) and (5.13) into (5.16) and (5.17), and neglecting common scaling factor, $R_{z,ref}[0]$ and $R_{z,ref}[1]$ can be rewritten as a function of TIADC input autocorrelation,

$$R_{z,ref}[0] = R_x(0), \tag{5.18}$$

$$R_{z,ref}[1] = R_x(T_s), \text{ if no residual gain error.} \tag{5.19}$$

5.3.3 Parameter Recursion

By subtracting (5.18) and (5.19) from (5.12) and (5.13), we have

$$R_{z,k}[0] - R_{z,ref}[0] = R_x(0)\left(\left(\frac{G_k^*}{\widetilde{G}_k}\right)^2 - 1\right), \tag{5.20}$$

$$R_{z,k}[1] - R_{z,ref}[1] = \frac{dR_x}{d\tau}\left(\delta_k^* - \widetilde{\delta}_k\right). \tag{5.21}$$

$R_x(0)$ is the input signal power, and so it is strictly positive for nonzero signals. The derivative $dR_x/d\tau$ at $\tau = T_s$ is strictly negative or positive depending on the occupied Nyquist zone. Therefore, the sign of the left-hand side of (5.20) and (5.21) uniquely determines if the current gain or timing estimate is greater or smaller than intrinsic ones. This leads to the following parameter update rule.

$$\widetilde{G}_k^{(i+1)} = \widetilde{G}_k^{(i)} + \beta_g\left(R_{z,k}^{(i)}[0] - R_{z,ref}^{(i)}[0]\right), \tag{5.22}$$

$$\widetilde{\delta}_k^{(i+1)} = \widetilde{\delta}_k^{(i)} + \beta_t\left(R_{z,k}^{(i)}[1] - R_{z,ref}^{(i)}[1]\right), \tag{5.23}$$

where $\beta_g > 0$ and

$\beta_t > 0$ if $x(t)$ is in odd-order Nyquist zones,

$\beta_t < 0$ otherwise.

$\widetilde{G}_k^{(i)}$ and $\widetilde{\delta}_k^{(i)}$ are the estimate of k-th channel gain and adjacent-channel timing error at i-th iteration, respectively. Once $R_{z,k}[0]$'s and $R_{z,k}[1]$'s are all equalized, the driving term in the parenthesis in (5.22) and (5.23) is zero, convergence being achieved. The stability and speed of convergence is controlled by β_g and

β_t which will be referred to as convergence parameters. Note that the use of adjacent-channel timing parameters enabled decoupling of parameter update for each channel.

5.3.4 Algorithm Summary

The overall calibration loop is represented as a signal-flow graph in Figure 5.3. Adjacent-channel timing parameters are converted to sampling time offsets before driving clock tuning circuitry. Note that the calculation of $2M$ correlation coefficients is practically all that is necessary for a single parameter update. This is significantly more efficient than previous blind techniques. The recursion rule in (5.22) and (5.23) also yields faster convergence than finite-difference methods or general search algorithms, because parameter adjustment is made with a priori known direction of decreasing residual error. Convergence is guaranteed given appropriate choice of convergence parameters (see next subsection). All these benefits come from the deliberate mixed-domain operation, i.e. direct tuning of sampling clocks driven by autocorrelation-based error detection in the digital domain.

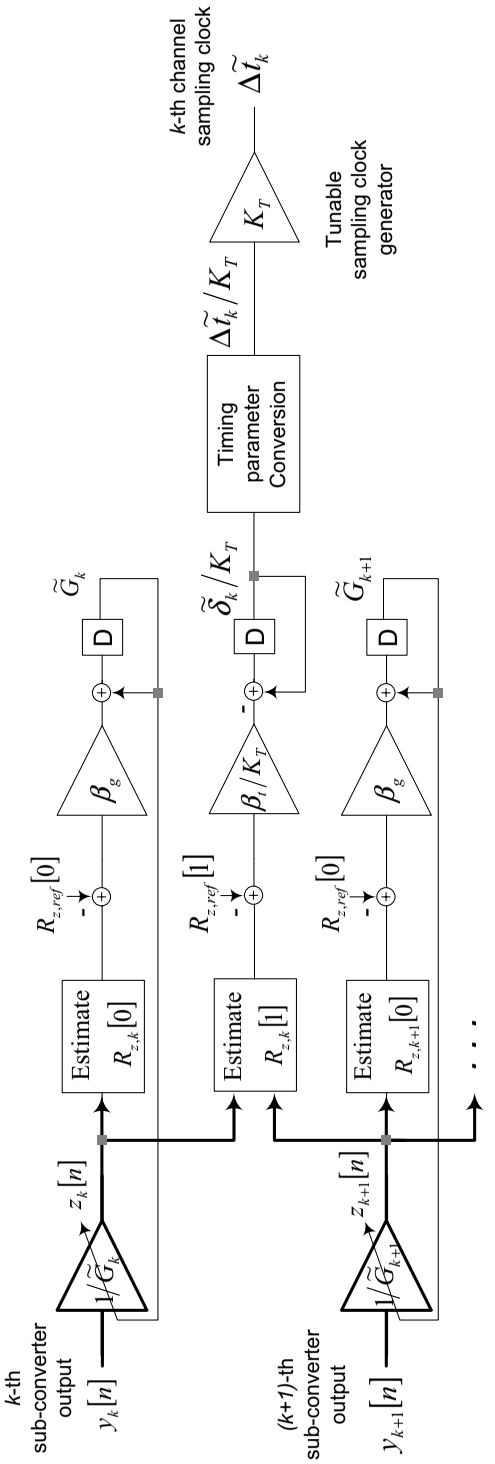

Figure 5.3: Signal-flow graph for the proposed mixed-domain blind calibration loop. K_T is the sensitivity of clock tuning circuitry. Thick line area has $1/T_s$ of clock rate, but thin line area has much lower activity for a batch-mode processing.

5.3.5 Convergence Analysis

Let's define $\gamma_k^{(i)}$ and $\varepsilon_k^{(i)}$ as residual gain and adjacent-channel timing error at i-th iteration, respectively.

$$\gamma_k^{(i)} = \widetilde{G}_k^{(i)} - G_k^*, \tag{5.24}$$

$$\varepsilon_k^{(i)} = \widetilde{\delta}_k^{(i)} - \delta_k^*. \tag{5.25}$$

Then, from (5.20)–(5.23), it can be shown that $\gamma_k^{(i)}$ and $\varepsilon_k^{(i)}$ follows a geometric series under a small-mismatch regime,

$$\gamma_k^{(i)} = (1 - 2\beta_g R_x(0))^i \, \gamma_k^{(0)}, \tag{5.26}$$

$$\varepsilon_k^{(i)} = \left(1 - \beta_t \frac{dR_x}{d\tau}\right)^i \varepsilon_k^{(0)}. \tag{5.27}$$

The effect of residual gain error is neglected in Figure 5.27, for simplicity. The magnitude of geometric ratios in (5.26) and (5.27) should be less than one to ensure convergence. For monotonous convergence, which is usually preferred over an oscillatory one, β_g and β_t must lie in the following range.

$$0 < \beta_g < \frac{1}{2R_x(0)}, \tag{5.28}$$

$$0 < \beta_t < \frac{1}{\dfrac{dR_x}{d\tau}}. \tag{5.29}$$

It is seen from the above that small values of β_g and β_t will in general guarantee monotonous convergence. Having large values of β_g and β_t will accelerate convergence as long as (5.28) and (5.29) are satisfied. This will, however, necessarily

amplify noise from the driving term (the one in the parenthesis in (5.22) and (5.23)), making the steady-state estimate also noisy. With same β_g and β_t, on the other hand, the gain and timing estimate will generally converge faster with higher input power and fast-changing input signal, respectively, as the geometric ratio in (5.26) and (5.27) becomes smaller.

5.3.6 Other Considerations

For simplicity, previous analysis assumed perfect gain match when discussing timing estimate convergence. Equation (5.13) suggests that nonzero residual gain error may bias timing error estimates. As long as the gain calibration loop is in action, however, timing estimates will eventually converge to a true parameter (see Section 5.4 for experimental results).

There are several factors which will more or less affect parameter estimation: ADC quantization noise, sampling clock random jitter, autocorrelation estimation error due to finite observation, finite-resolution sampling clock tuning, etc. Using small values of β_g and β_t, or increasing the batch size N, in general decrease the contribution of these noise sources. However, sampling clock quantization error can only be reduced by increasing its resolution. The minimum tuning resolution should be commensurate with the target signal-to-noise ratio (SNR) or spurious-free dynamic range (SFDR) level. For example, 80 dB of target SNR requires

approximately $0.00003T_s$ of timing control resolution (assuming the input sinusoid is at $1/2f_s$). If the delay control range is $0.03T_s$, for instance, then approximately 1000 quantization levels (i.e. 10-bit level) will be necessary.

Other than the minimum resolution requirement for timing control, the proposed calibration scheme is tolerant to analog imperfections in clock tuning circuitry. For example, the precise tuning curve needs not be known. It can even change between calibration cycles since the feedback action of the blind calibration will eventually track such variations. As a final remark, note that the recursion rule in (5.22))-(5.23) is only a basic realization retaining essential features. More sophisticated or efficient implementation may be possible. See e.g. [64].

5.4 Experimental Results

Experimental results based on an $M = 4$ TIADC are presented in this section to demonstrate the proposed calibration method. The proposed calibration method is tested with a number of different input signals, across multiple Nyquist zones.

5.4.1 Setup

Figure 5.4 shows the $M = 4$ TIADC experimental setup. Four 14-bit 100 MSPS commercial ADC's (AD6645 from Analog Devices, Inc.) are used to obtain 400 MSPS of aggregate sampling rate. The logic analyzer performs both data acquisition and digital signal processing by custom C-program. Four-phase sampling clock is derived from a single 100 MHz reference clock, followed by a voltage-controlled delay line. Each tunable line consists of a single 50 ohm T-section $(L - C - L)$ with reverse-biased varactor diodes (MV104 from ON Semiconductor) for delay control. The delay line provides approximately $0.2T_s$ ($T_s = 2.5ns$) of delay tuning range across 0–3 V of tuning voltage. Tuning sensitivity K_T is 0.06 T_s/V at the center. A single iteration takes 1–10 s, depending on the batch size N. The speed is mainly limited by the logic analyzer arming and acquisition time.

5.4.2 Narrowband Input Test

Sinusoids are used as a representative narrowband input signal. Convergence parameters are chosen to be 1/10 of the stability limit given by (5.28)-(5.29) (β_g, $\beta_g \approx 0.2$). Batch size for all narrowband tests is N=4,096.

First, a 171.567 MHz sinusoid is applied at the TIADC input, and the blind calibration loop is initiated. Figure 5.5 shows the measured convergence curve for

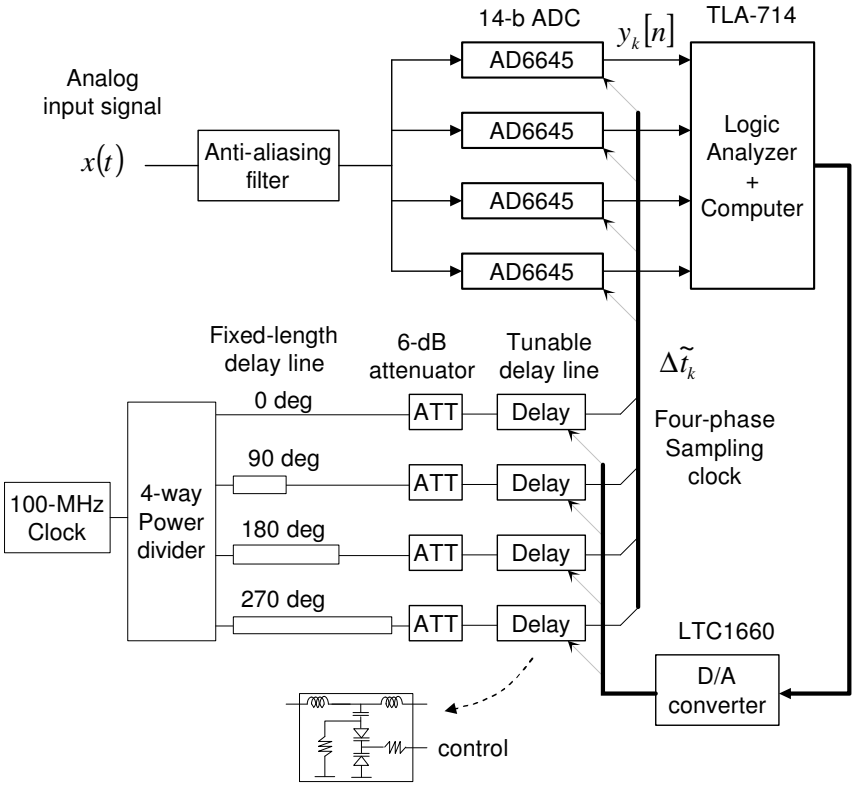

Figure 5.4: Experimental setup for a $M = 4$, 400 MSPS TIADC with the proposed mixed-domain blind adaptive calibration loop. Sampling clock is fine-tuned by a single $L - C - L$ section of varactor-loaded delay line. Six-dB attenuators minimize impedance variation with varactor tuning, thus preventing undesirable cross-line tuning effects.

gain and sampling time error estimate. Theoretical learning curves are calculated by (5.24)-(5.27), and superimposed on the same plot (dotted lines). It is seen that the measurement closely follows prediction. Small discrepancy in timing convergence plot is due to slight curvature in delay tuning characteristic (the prediction assumes linear tuning).

Figure 5.6 shows the TIADC output spectrum before and after 300 calibration iteration. The proposed calibration suppressed mismatch spurs by more than 40 dB, achieving >80 dB of SFDR. Figure 5.7 shows the improvement in SFDR over iterations. Note that the initial linear increase (in dB scale) comes from exponential parameter convergence. The total number of observation samples to reach 80 dB of SFDR is approximately 10^6 ($\approx 230N$). Equalization process of output correlation coefficients is shown in Figure 5.8.

Next, the frequency of the input sinusoid is swept across the first two Nyquist zones, i.e. 10–390 MHz, with the same batch size N=4,096. SFDR in the steady state is measured and plotted against test frequencies in Figure 5.9. Up to 70–90 dB of SFDR is consistently observed.

There are three frequencies in the first Nyquist zone where the stationary input assumption fails for $M = 4$: 50 MHz, 100 MHz, and 150 MHz. As the input sinusoid comes closer to one of these frequencies, longer batch size is required to maintain calibration performance (for more effective phase randomization).

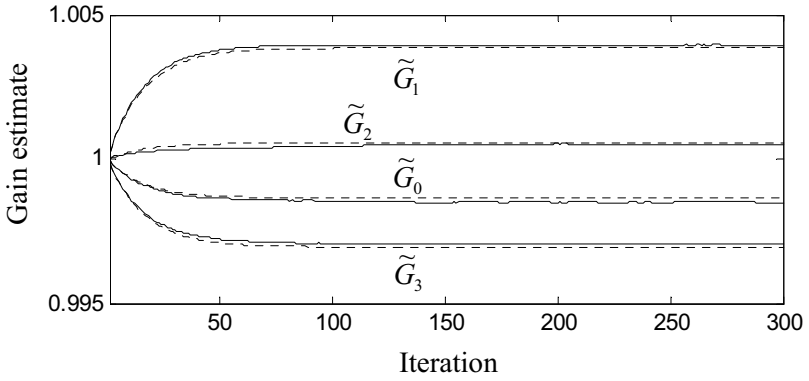

(a) Convergence of gain estimates

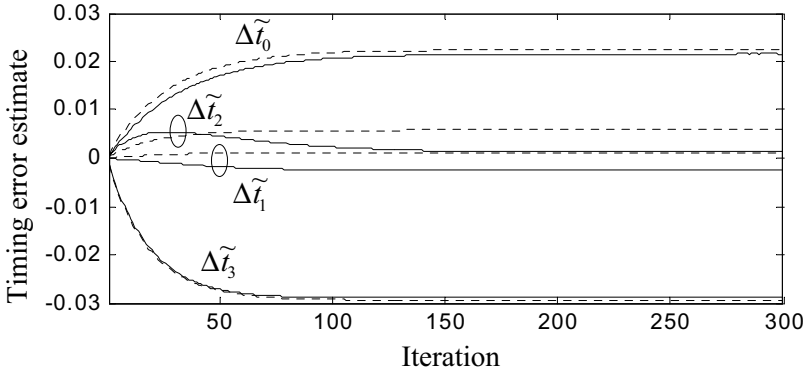

(b) Convergence of timing estimates

Figure 5.5: Measured convergence plot of gain and timing error estimates with a 171.567 MHz sinusoidal input. Solid lines represent measurement. Dotted lines denote predicted curves by (5.26)-(5.27)) with intrinsic gain [0.99865, 1.0038, 1.0005, 0.99695], and sampling timing errors [$0.0224T_s$, $0.0012T_s$, $0.0058T_s$, -$0.0294T_s$] characterized at 172.8 MHz by a training method (Chapter 2)

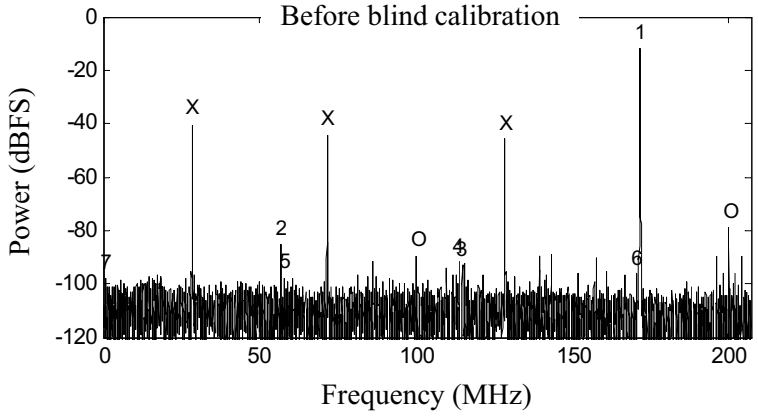

(a) Before iteration begins

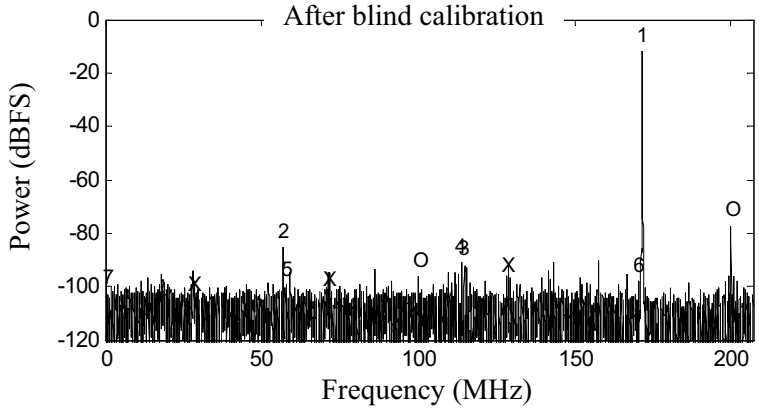

(b) After 300 iterations ($N = 4,096$)

Figure 5.6: Measured TIADC output spectrum with a 171.567 MHz input (marked with '1'). Gain and sampling time mismatch spurs are labeled with 'X'. 'O' represents offset spurs. Input signal harmonics up to 7-th order are also shown as numbers.

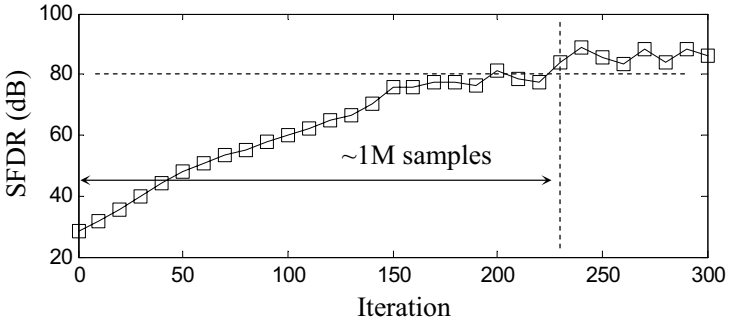

Figure 5.7: Improvements in SFDR during 300 iterations with a 171.567 MHz sinusoid input ($N = 4,096$). Total 10^6 samples are used to reach 80 dB of SFDR.

Calibration performance versus batch size near 150 MHz is investigated in Figure 5.10. No performance loss is observed down to 150.5 MHz. If the input is at 150.05 MHz, however, SFDR drops below 50 dB (still 20 dB of calibration gain), and at least $N = 10^5$ is necessary to regain 80 dB of SFDR level. In summary, the batch size N=4,096 can meet 80 dB of single-tone SFDR requirement over 98.5% of the entire Nyquist band. If longer observation up to $N = 10^5$ is allowed, then the spectral performance is maintained over 99.85% bandwidth.

Note that the multiple Nyquist-zone operation as shown in Figure 5.9 would not be feasible in fully digital blind methods, unless switching through different sets of correction filters.

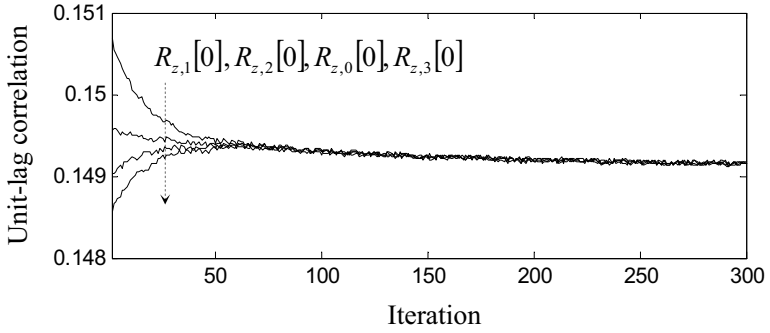

(a) Equalization of unit-lag correlation coefficients

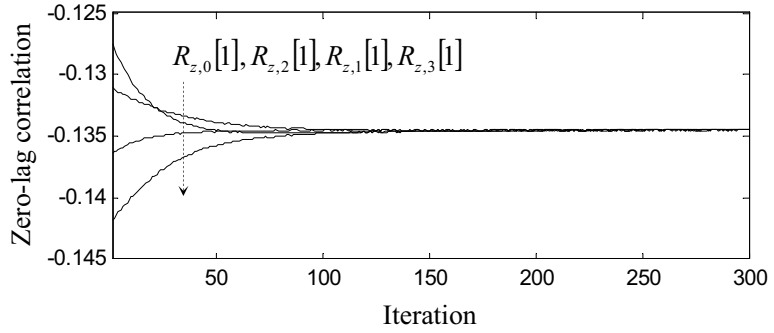

(b) Equalization of zero-lag correlation coefficients

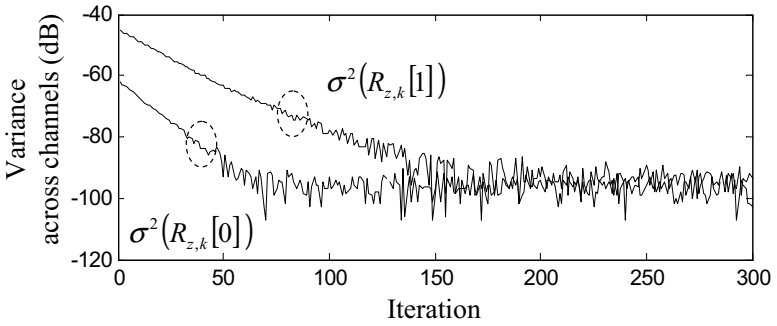

(c) Variation of correlation coefficients across channels

Figure 5.8: Measured equalization plot of correlation coefficients and their cross-channel variance. The input signal is a sinusoid at 171.567 MHz.

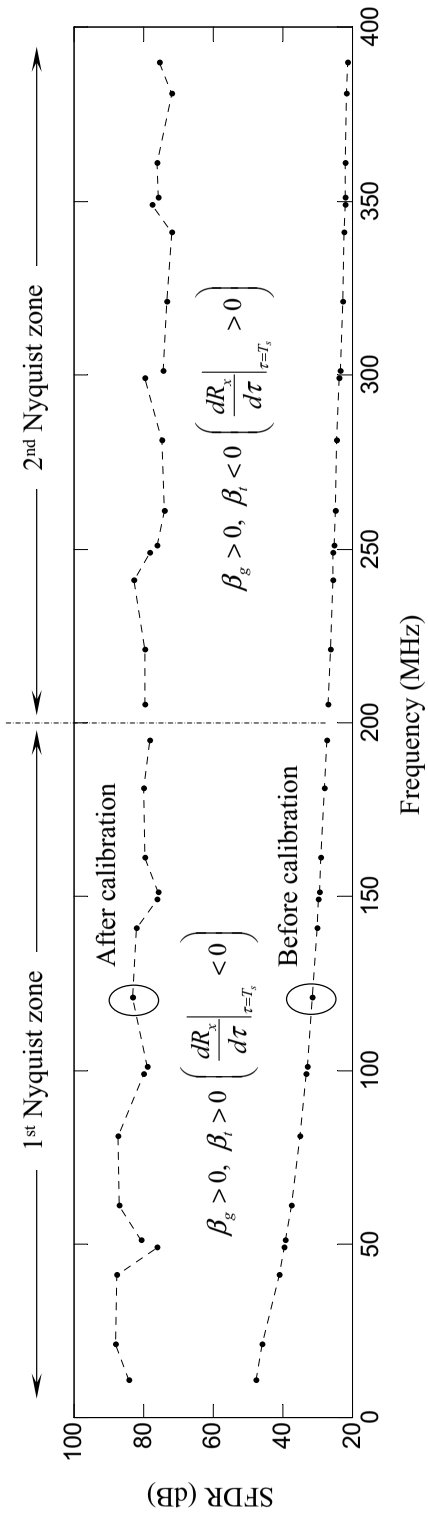

Figure 5.9: Single-tone SFDR test across multiple Nyquist zones ($N = 4,096$). Six measurements were averaged for each test point (shown as dot). The sign of correlation derivative and convergence parameters is also shown. The input anti-aliasing filter (cutoff=187 MHz) was removed for this test.

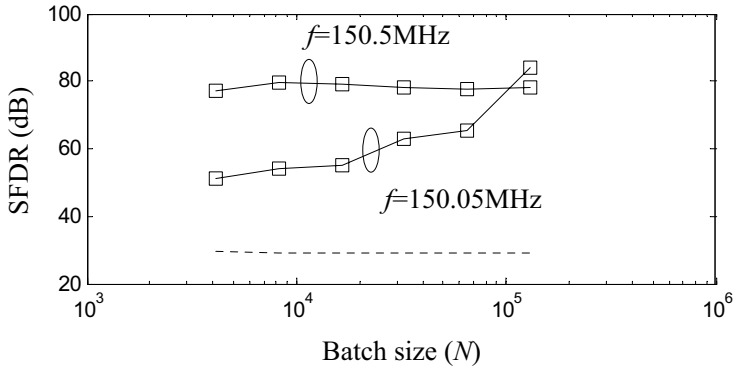

Figure 5.10: Single-tone calibration performance near 150 MHz input, which is one of the failure frequencies (50, 100, and 150 MHz). The closer the input frequency approaches to 150 MHz, the longer batch is required. Dotted line is uncalibrated performance.

5.4.3 Wideband Input Test

An independent, identically distributed sequence is first generated by an arbitrary waveform generator, and filtered by a 10-tap FIR filter. Its occupied bandwidth is approximately 180 MHz. Unlike sinusoidal inputs, wideband input signals mostly overlap with their own aliasing products. For the purpose of alias identification, a deep notch is created at 80 MHz. Before calibration, there exist significant channel mismatches, and the notch at 80 MHz is partially filled with frequency-shifted input spectra (Figure 5.11(a)). After 1,200 iterations, calibration suppresses aliasing products, and the deep notch is restored, as seen in Figure 5.11(b). Parameter convergence plots are shown in Figure 5.12. Note that the batch size $N = 131,072$ is much longer than the narrowband case. This

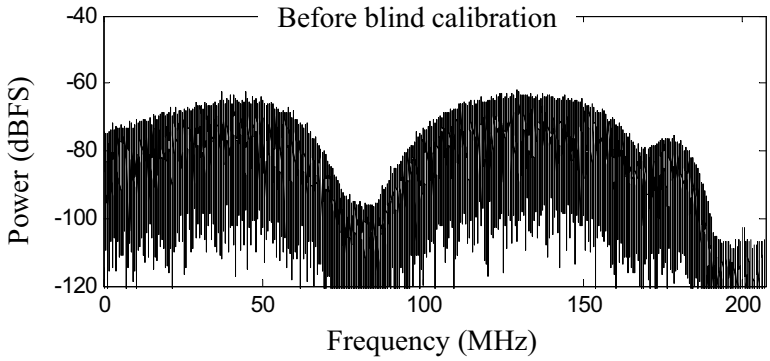

(a) Before iteration begins

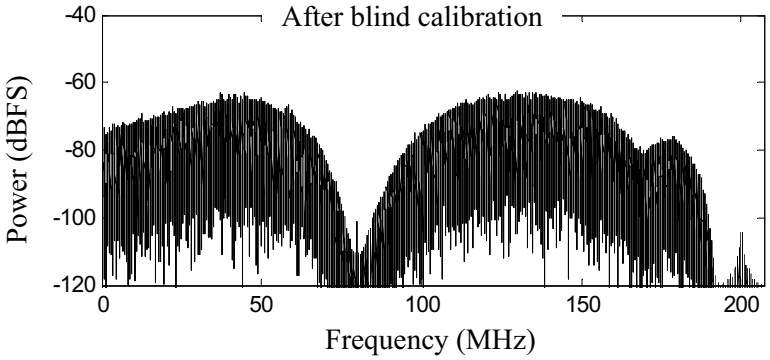

(b) After 1,200 iterations ($N = 131,072$)

Figure 5.11: Measured TIADC output spectrum with a dc–to–180 MHz wideband input signal before and after blind calibration. The original deep notch at 80 MHz was masked by aliasing products before calibration, but is restored after calibration, implying that mismatch is corrected.

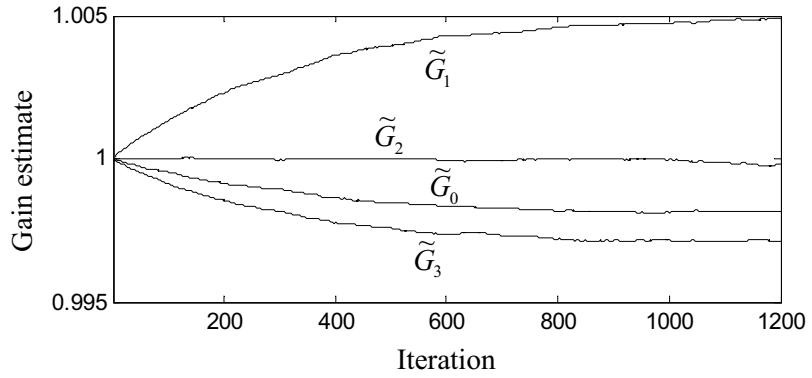

(a) Convergence of gain estimates

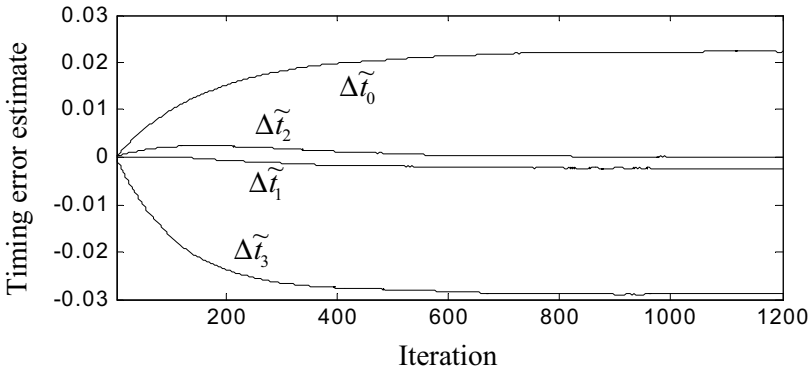

(b) Convergence of timing estimates

Figure 5.12: Measured convergence plot of gain and timing estimates with the wideband input signal in Figure 5.11($N = 131,072$).

is because empirical correlation coefficients for wideband signals are noisier than narrowband ones, in general.

5.4.4 Effects of Residual Gain Error on Timing Convergence

As a last test, timing calibration loop is first initiated with a 171.567 MHz sine input, with gain correction turned off. In Figure 5.13(b), timing estimates are seen to converge with bias in the presence of residual gain error. After 200 iterations, gain correction loop begins (Figure 5.13(a)), and timing parameters start re-adjusting themselves. After another 100 iterations, both gain and timing estimates achieved convergence to a true parameter. Under a small-mismatch regime, in general, residual gain error does not significantly affect the convergence of timing parameters, as experimentally verified by Figure 5.13(b) and Figure 5.13(c).

5.5 Conclusions

In this chapter, a new adaptive blind technique for multi-channel TIADC's is demonstrated. The analog-domain correction of timing mismatches, combined with autocorrelation-based error detection, dramatically reduces hardware and

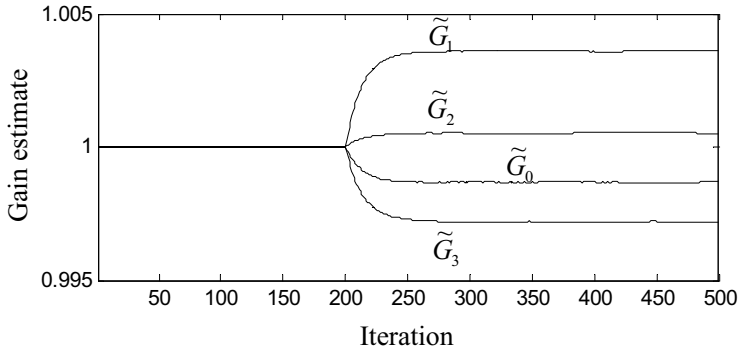

(a) Convergence of gain estimates

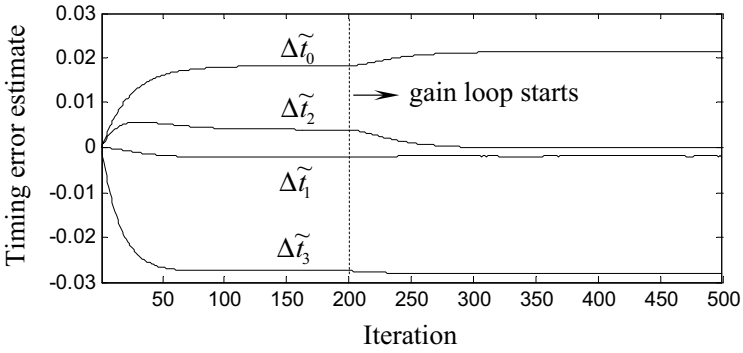

(b) Convergence of timing estimates

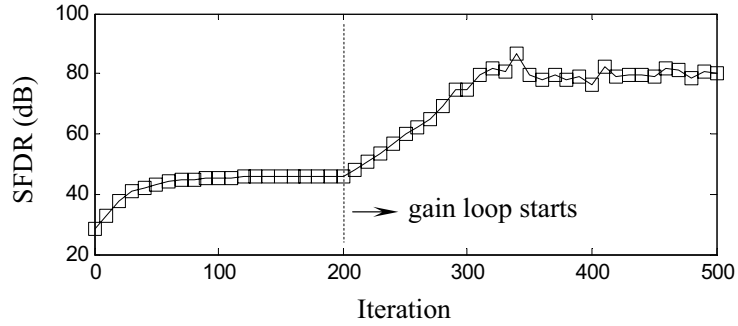

(c) SFDR

Figure 5.13: Measured convergence plot with a 171.567 MHz sine input. Gain adaptation is intentionally delayed by 200 iterations to see its effect on timing error convergence.

computational complexity. Specifically, empirical calculation of $2M$ output autocorrelation coefficients is practically enough for a single parameter update. Exceptional spectral performance of 70–90 dB of mismatch-limited SFDR was experimentally achieved across the first two Nyquist zones. Proof of parameter convergence is given under WSS input assumption, but the algorithm accepts many practical non-WSS signals as well. There is no restriction in the number of TIADC channels, input bandwidth, etc

Chapter 6

Millimeterwave Imaging Sensor Nets: A Scalable 60 GHz Wireless Sensor Network

Sensor networks provide distributed information collection and transmission, and are useful for many industrial, environmental or military applications. A large number of sensors are randomly or systematically deployed over a certain field for local data gathering. Such information is transferred to a final destination in a multi-hop fashion (Figure 6.1) among neighboring sensors by locally forming an ad-hoc network. For a complete information map, a certain kind of positioning is also necessary in most cases, i.e. each sensor node needs to provide its own location information as well. External positioning capability such as GPS may be used for this purpose.

This conventional approach is widely used in many practical applications, but scalability issue arises when the number of sensor nodes is very large (e.g.

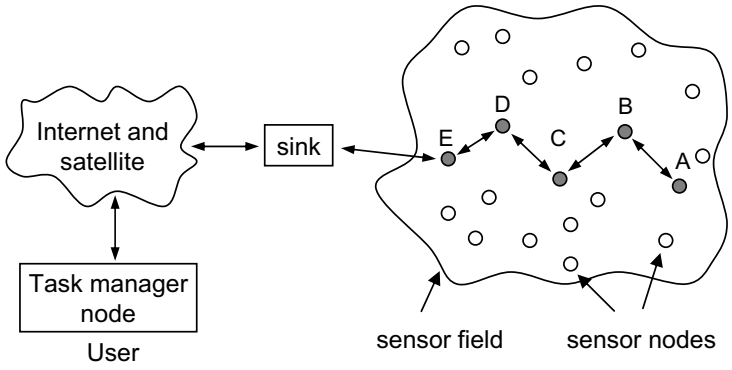

Figure 6.1: A Multi-hop based wireless sensor network. After [8].

$> 1,000$). First, multi-hop data transmission is not very efficient in a large scale network. Second, the cost of each sensor may not scale down commensurately with the scale of network because of the minimum required intelligence (for e.g. positioning and ad-hoc networking). The complexity of sensor also strongly correlates with power consumption. Although modern CMOS technologies enable efficient signal processing, the collective cost and energy expenditure may be unacceptable for very large scale sensor networks.

In this chapter, we demonstrate a new approach to large-scale sensor nets [65–67]. The next section describes the proposed system architecture. The following sections present the system design and experimental characterization results based on a short-range (< 10 m) indoor radio experiment.

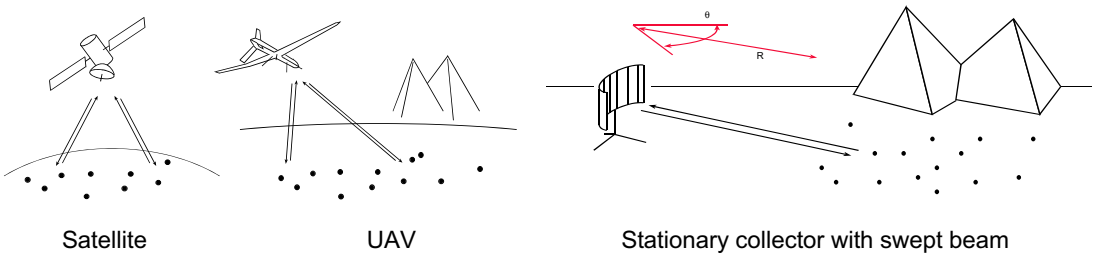

Figure 6.2: Typical realizations of the proposed imaging sensor networks with three different kinds of information collectors

6.1 Imaging Sensor Net Architecture

The motivation behind the proposed architecture is best described by simplistic sensors: stripped of their complexity to retain only essential functionality without any geolocation (positioning) or networking capability. This will enable ultimate cost and energy efficiency in favor of a very large scale network. The system complexity (or functionality) is instead moved to an information collector, whose spatially narrow radio beam selectively activates a subset of sensor nodes.

Figure 6.2 illustrates three representative scenarios. In either case, the collector beam sequentially scans a sensor field (2-D or 3-D in general). Illuminated sensors respond to the beacon by appropriately modulating and sending it back to the collector, as illustrated in Figure 6.3. The collector, upon completing a full scan, acquires necessary information map across sensor field. The location of each sensor can also be accurately determined by using a wide bandwidth, spa-

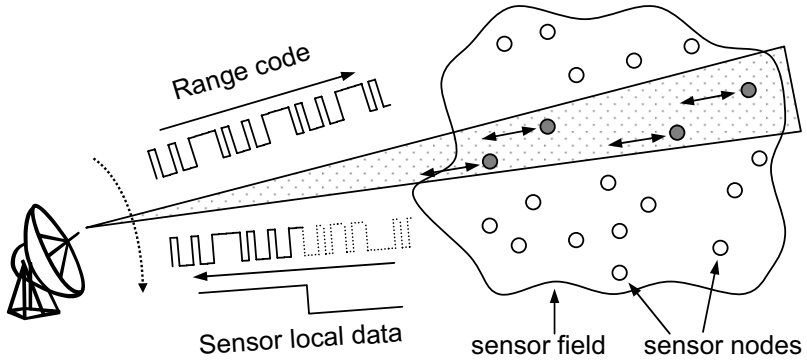

Figure 6.3: Virtual imaging approach to the wireless sensor network

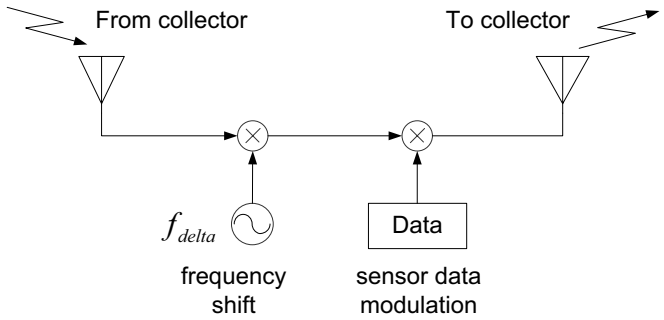

Figure 6.4: Equivalent circuit for a imaging sensor node

tially narrow beacon in analogy to radar. The return signal, however, also carries local data from possibly a number of sensors, unlike conventional radar. Furthermore, sensors intentionally shift the frequency of the received beam to differentiate their transmission signal with direct ground return or environmental reflections (Figure 6.4). This necessitates non-coherent signal processing unlike conventional synthetic aperture radar (SAR). The proposed sensor net can also be interpreted

as a virtual imaging network: image map is drawn from reflected light by a large number of target pixels.

6.2 Radio Link Characterization

The round-trip radio link between the collector and passive sensor is governed by the following relationship.

$$\begin{aligned} \frac{P_r}{P_t} &= \left(\frac{P_r}{P_t}\right)_{up} G_{sens} \left(\frac{P_r}{P_t}\right)_{down} \\ &= \left(D_{TX} D_{sens} \lambda_{down}^2 \frac{e^{-\alpha R}}{(4\pi R)^2}\right) G_{sens} \left(D_{RX} D_{sens} \lambda_{up}^2 \frac{e^{-\alpha R}}{(4\pi R)^2}\right). \end{aligned} \tag{6.1}$$

In (6.1), P_r and P_t are the collector receive and transmit power, respectively. D_{TX}, D_{RX} and D_{sens} are collector TX, RX and sensor antenna gain. λ_{up} and λ_{down} are up and down-link wavelength, respectively. R is the distance and α is atmospheric attenuation constant, 6–16 dB/km in the 60 GHz unlicensed band. G_{sens} models modulation loss in the sensor ($\simeq -5.6$ dB). Other sources of power attenuation include matching loss, polarization loss, etc. Note from (6.1) that the received power quickly drops as $1/R^4$. To revert to more desirable $1/R^2$ dependency, the sensor must operate in a power-limited regime with sufficiently high RF gain.

At a sensor data rate of B, the received E_b/N_0 is

$$\frac{E_b}{N_0} = \frac{P_r}{kTBF}, \tag{6.2}$$

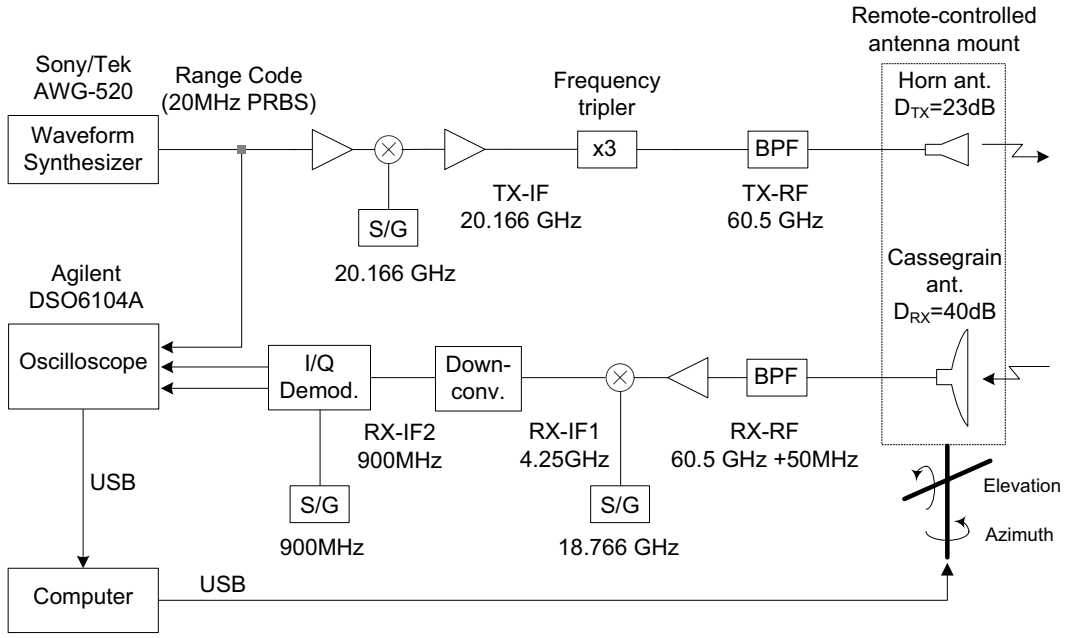

Figure 6.5: Block diagram of the 60 GHz prototype collector

where $kT = -174$ dBm and F is the receiver noise figure. Assuming BPSK or differentially-encoded BPSK (DBPSK) modulation, approximately 12 dB of E_b/N_0 is required to achieve 10^{-6} of uncoded bit-error rate (BER).

6.3 Prototype Collector

Figure 6.5 and Figure 6.6 show a simplified block diagram and a photo of the experimental 60 GHz collector, respectively. It consists of three functional blocks: up-down converter, steerable high-gain antennas and digital signal processing routine.

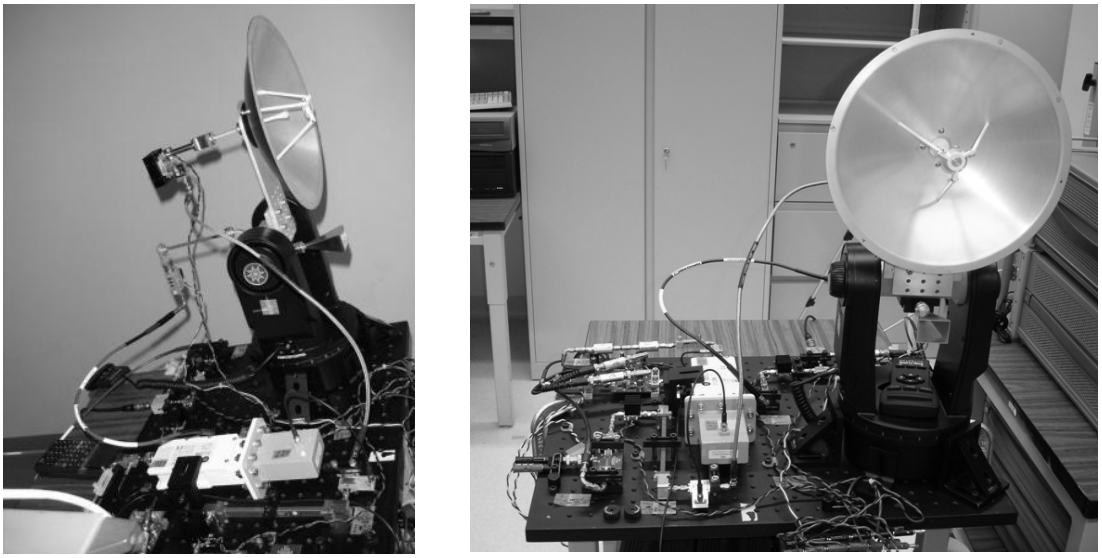

Figure 6.6: A photograph of the collector prototype

6.3.1 60 GHz Up/Down Converter

The input to the up/down converter is a range code, which is basically a wide-band signal having a sharp autocorrelation peak. By taking cross-correlation between its transmit and receive copy, and by finding the location of peak, the relative distance between the collector and sensor can be estimated. In this initial work, a pseudo-random bit sequence (PRBS) signal is adopted.

The chip-rate (CR) and length of PRBS determines raw range resolution and the sensor field size, respectively. With higher CRs, a single chip travels shorter distance in the air, and thus the correlation peak becomes sharper, providing finer range resolution. One PRBS period must be long enough to enable round-

trip propagation from the most distant sensor. Otherwise, a single correlation peak will correspond to two or more different ranges, causing ambiguity. The CR and its length is chosen to be 20 MHz and $2^6 - 1$, respectively. A single chip round-trip gives $c/(2CR) = 7.5$ m of range resolution (c=the speed of light). The PRBS repeats itself for every $(2^6-1)/CR = 3.15$ us, and this is enough for unique determination of the range up to 472.5 m.

The PRBS is upconverted to *TX-IF* (=20.166 GHz) followed by frequency triplication to reach 60.5 GHz. The tripler output power is 7 dBm. The transmitted beam, once received by a sensor, is shifted in frequency by 50 MHz (to filter out ground returns), and received by a high-gain collector antenna. A harmonic mixer and block down-converter translates the received beam down to the first IF (*RX-IF1* =4.25 GHz) and second IF (*RX-IF2* =900 MHz), respectively. The final *I/Q* demodulator output is digitized by a multi-channel oscilloscope for subsequent digital signal processing. A copy of transmit PRBS code is also captured for timing (and hence range) reference.

6.3.2 Steerable High-gain Antennas

High-gain antennas are beneficial for the proposed imaging sensor nets for two reasons. First, higher-gain antennas have proportionately narrower beam angles,

yielding finer angular resolution. This is seen from the following relationship [68].

$$D \approx \frac{\pi}{\Theta_1 \Theta_2}, \tag{6.3}$$

where D is the antenna gain, and Θ_1 and Θ_2 are half-power beamwidth (in radians) of the antenna along two orthogonal directions, respectively. Second, transmit power density is proportional to the antenna gain. The collector beacon therefore reaches further with higher gain antenna. The gain of TX and RX antenna for the prototype collector in Figure 6.5 is D_{TX}=23 dB and D_{RX}=40 dB, respectively. Their half-power beamwidth is approximately 14 degree and 2 degree, respectively. They are mounted on a motorized positioner so that the beam can be steered in azimuth and elevation with sub-degree accuracy.

6.3.3 Digital Signal Processing: Localization and Demodulation

The role of collector signal processing is first, to accurately determine the location of sensors, and second, to reliably demodulate local sensor data at the same time. An outline of the localization process is given fist, neglecting sensor data modulation for simplicity. The detailed description is given next.

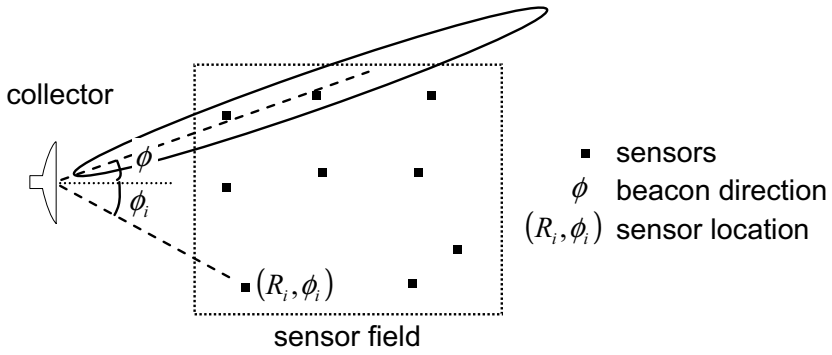

Figure 6.7: Imaging sensor net geometry in angular coordinate

Outline of the Localization Process

Figure 6.7 illustrates the sensor network coordinate assuming a beam-steerable collector. Only one angular coordinate is considered for simplicity. The discussion however easily extends to a more general case with two orthogonal angular coordinates for full 3-D localization.

Let $s(t)$ the range code, and $r(t, \phi)$ the collector receive signal as a function of azimuth angle ϕ and time t. Assume the collector is at origin, and a single sensor is located at (R_1, ϕ_1). $r(t, \phi)$ is then represented as

$$r(t, \phi) = G\left(\phi - \phi_1\right) s\left(t - R_1/2c\right) + n(t), \tag{6.4}$$

where $G(\phi)$ and $n(t)$ is the antenna gain function (AGF) and Gaussian noise, respectively. The maximum-likelihood (ML) estimate of the sensor location,

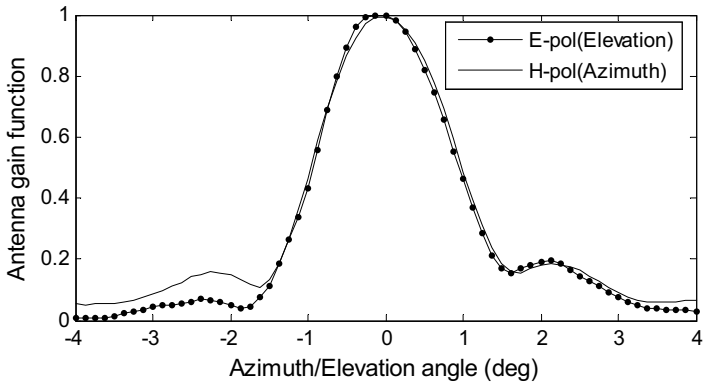

(a) Measured 1-D AGF across E-pol (vertical) and H-pol (horizontal) plane.

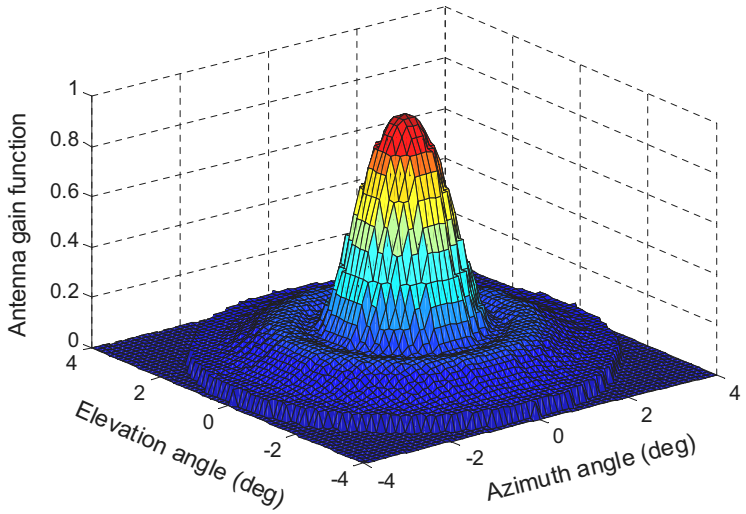

(b) Reconstructed 2-D AGF from (a) assuming circular symmetry.

Figure 6.8: Measured antenna gain function (AGF).

$(\widetilde{R}_1, \widetilde{\phi}_1)$, can be obtained from the observation $r(t, \phi)$ by

$$(\widetilde{R}_1, \widetilde{\phi}_1) = \arg\min_{(\widetilde{R}, \widetilde{\phi})} \left\langle G\left(\phi - \widetilde{\phi}\right), \left| \left\langle r(t, \phi), s\left(t - \widetilde{R}/2c\right) \right\rangle_t \right| \right\rangle_\phi , \qquad (6.5)$$

where $< \cdot >_t$ and $< \cdot >_\phi$ is taking cross-correlation in t and ϕ, respectively. Equation (6.5) is essentially 2-D matched filtering, but only the magnitude is taken from the range correlation output. This is because the phase of $r(t, \phi)$ is unknown to the collector. The AGF $G(\phi)$ is equal to the cascade of collector TX and RX antenna. For the present prototype, $G(\phi)$ is almost equal to RX antenna (40 dB cassegrain) pattern since the TX antenna (23 dB horn) has a much wider 3 dB beamwidth.

Figure 6.8 shows the measured AGF as a function of two orthogonal angular coordinates, i.e. the elevation and azimuth. The actual localization process, therefore, involves triple matched filtering as a direct extension of (6.5).

Detailed Description

This section presents detailed descriptions on the signal processing algorithm for sensor data extraction and location estimation. The algorithm operates on the I- and Q- channel data captured from the collector receiver along different orientations of the collector antenna (termed *snapshots*). In order to support real-time processing speeds, suboptimal but efficient strategies are adopted. The algorithm must operate in the presence of a residual frequency offset, due to sensor

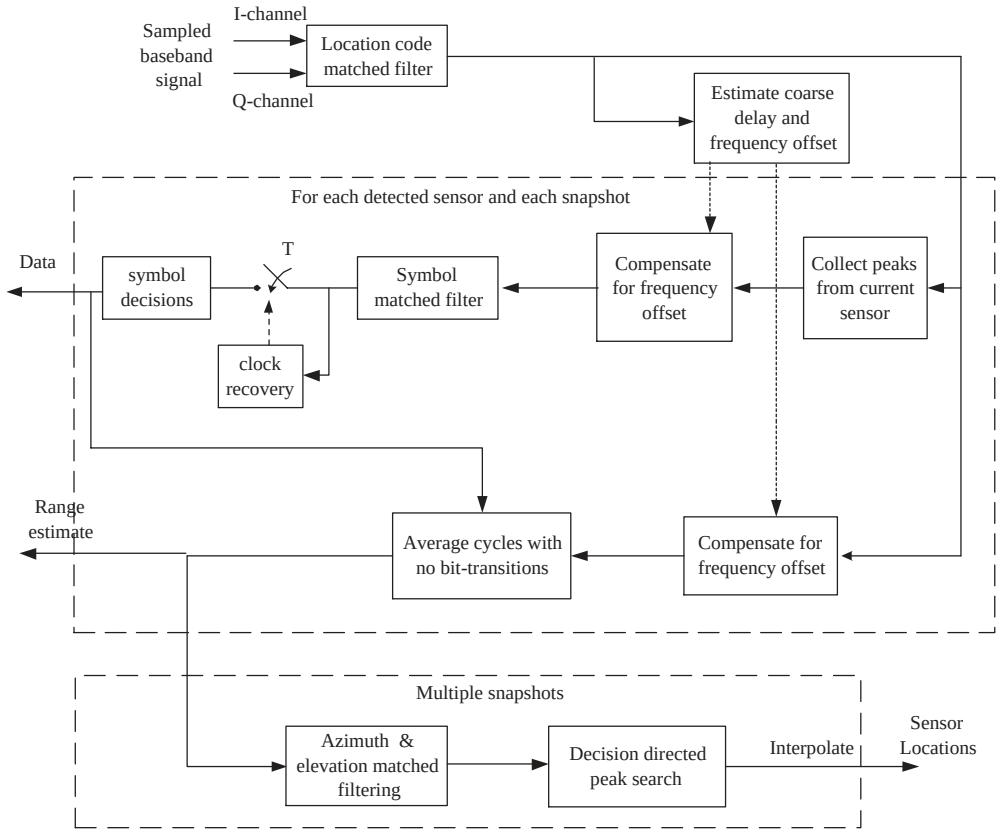

Figure 6.9: Block diagram of the collector signal processing algorithm (Courtesy of Bharath Ananthasubramaniam)

frequency offset uncertainties, and without timing synchronization between the sensor and collector, which is unlike a standard spread-sprectrum (SS) system.

The signal at the output of the collector receiver chain, in complex baseband notation, is given by

$$r(t) = A \underbrace{b(t)}_{\text{Data}} e^{j2\pi\Delta f t + j\psi} \sum_k \underbrace{s(t - kT_c - 2\tau)}_{\text{Range}} + n(t). \tag{6.6}$$

where A is the received signal amplitude, ψ and Δf are the phase and frequency offsets between the collector and sensor LOs, τ is the one-way propagation time between the collector and the sensor, $s(t)$ is one period of the BSPK-coded range code with a single chip time T_c, the differential BPSK data stream is $b(t) = \sum_l d_l\, p(t - lT_b - \delta)$, where $p(t)$ is the symbol pulse shape, T_b is the symbol interval (duration of $p(t)$), and δ is timing offset between the collector and sensor clocks, and $n(t)$ is AWGN in the received signal from both the collector receiver and sensor transceiver.

It is clear from (6.6) that the sensor data and sensor location information are tightly coupled in the received signal, and the residual frequency modulation must also be undone before the data or the range can be estimated. We simplify the processing by choosing the location code bandwidth $\sim 1/T_c$ to be much larger than the residual frequency offset Δf and data rate $1/T_b$. Such a choice ensures that data and frequency offset have little effect on the the phase coding in the location code. The matched filtering with the location code can thus be performed with the location code template to extract the propagation delay τ before the residual frequency offset estimation and data extraction. The block diagram of the complete signal processing algorithm is shown in Figure 6.9 and we briefly discuss each block below.

Location Code Matched Filter: The received signal $r(t)$ is matched filtered against the location code $s(t)$ neglecting the effects of the residual frequency modulation and data. If a sensor reflection is present, periodic peaks in the in the matched filter (MF) output corresponding to the sensor range (2τ) is obtained for each location code cycle separated by T_c seconds in the absence of noise. In particular, the round trip propagation delay is measured differentially between peaks in the matched filter local copy of the location code and peaks in the sensor return, in order to compensate for any drifts in the collector chip clock.

It can be observed that the peaks in the MF output are scaled by a product of the residual frequency offset and the modulating data. Since, by design, both the frequency offset and data vary far slower than a location code period, the sequence of peaks is an oversampled version of the data stream with the residual frequency modulation.

Coarse Delay and Frequency Offset Estimation: In order to extract this sequence of complex factors, the peak locations must be estimated after averaging out noise. Therefore, the MF output is coherently averaged for each of several discrete hypotheses for the delay and frequency offset, and the hypotheses that capture the most of the signal energy are chosen to correspond to reflecting sensors. In essence, we generate a delay-frequency profile of the received signal and search for sensors in this two dimensional space. Since the I- and Q-channel sig-

nals are already sampled in time, these samples naturally provide a set of coarse "delay bins" to search over. A periodogram is constructed for each delay bin, which is efficiently computed using the FFT.

Collection of Peaks in MF output: The coarse delay estimate can now be used to extract the sequence of peaks in the MF output. The noise is white as the output of the MF is sampled every T_c seconds maintaining the independence between samples.

Frequency Offset Compensation: The residual frequency modulation can be canceled by appropriately rotating the phase of the peak samples using the estimated residual frequency offset. We are now left with the problem of decoding DBPSK data in AWGN, which is easily accomplished.

Symbol Matched Filter: The data stream that is embedded in AWGN can be recovered by matched filtering with the symbol pulse shape $p(t)$. But, the optimal times for sampling the symbol matched filter (SMF) output are not known. Therefore, the data symbol clock must also be recovered from the SMF output.

Symbol Clock Recovery and Symbol Decisions: We utilize the Gardner detector [69] that only requires only two samples of the SMF output per symbol period, one of which is used for symbol decisions. The detector determines the optimal sampling instants by searching for maxima in the rectified SMF output using a searching for the instant when the average derivative goes to zero. Since this

detector does not require phase synchronization it is resilient to residual phase errors from the frequency offset compensation. Finally, the DBPSK data, which is also robust to residual phase errors, is differentially demodulated.

Data and Frequency Offset Compensation: The coarse delay was estimated using the delay-frequency profile is not accurate enough for range estimation. To enable coherent averaging, the effects of the data and residual frequency modulation on the MF output are first undone. However, this is not equivalent to the MF output in the absence of data and residual frequency offset as data symbol transitions alter the phase coding in the location code destroying its autocorrelation properties.

Soft Delay Estimation: In order to avoid the computational burden of compensating for the data and frequency offset prior to the MF, we use the compensated MF output in the previous step, but drop all the cycles of the location code that contain a symbol transition. Since there are sufficiently many location code cycles in every symbol interval and the residual frequency modulation causes very little phase variation in a cycle duration, the cycles with no symbol transitions (known from demodulated data) are equivalent to MF outputs in the absence of data and residual frequency modulation. It is now simple to average multiple periods of the MF output that are aligned in phase to obtain one period of the MF output

that can be used for range localization. In order to get subsample resolution the averaged MF output is suitably interpolated.

Now, an azimuth and elevation matched filtering across multiple snapshots can be further performed to locate the sensor in three dimensional coordinates.

6.4 Prototype Sensor

The essential functionality of imaging net sensors is to receive, modulate and re-radiate the 60 GHz beacon. The construction of communication circuits in the 60 GHz band presents a certain level of difficulty in low-cost implementation. One quarter-wavelength at 60 GHz is approximately 0.5 mm on a $\varepsilon_r = 4$ substrate. This is rather small compared to lithographic tolerance ($\approx$ 1 mil=0.025 mm) and minimum line width/spacing (4$\approx$5mil=0.1$\approx$0.125 mm) in standard low-cost PC board manufacturing (finer technologies may be sought, e.g. LTCC, but at a potentially significant cost penalty.). Sensor RF circuitry (antenna, matching network, etc) will therefore suffer from detuning. RFIC integration will be cost-effective, but the sensor antenna will still need to be off-chip due to its considerable size. Further, dielectric loss and skin effects introduce significant signal attenuation at 60 GHz band, especially with low-cost substrates. All above con-

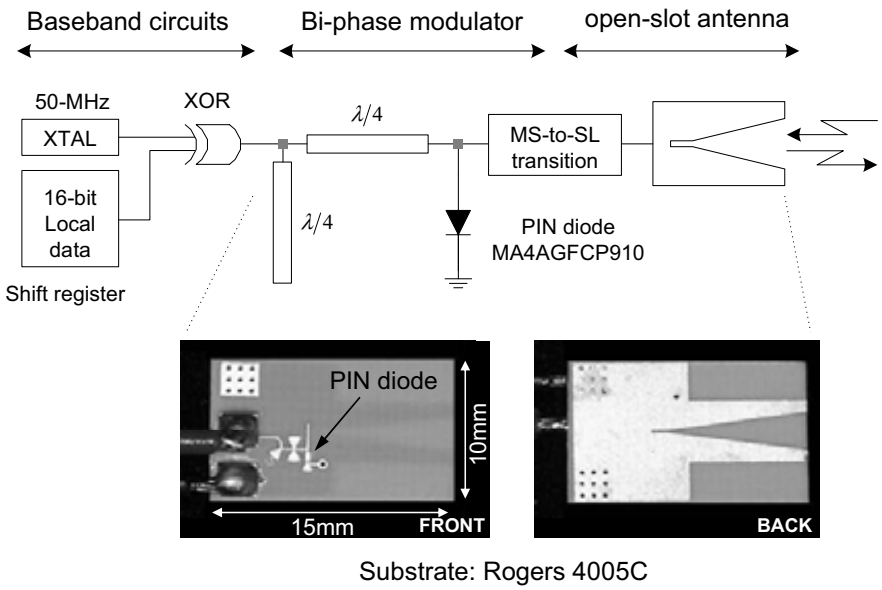

Figure 6.10: A prototype 60 GHz low-cost passive sensor with a wideband antenna and BPSK modulator.

siderations suggest that the sensor RF circuitry must be simple and robust against manufacturing error.

Figure 6.10 shows the 60 GHz prototype sensor block diagram. The RF circuitry is implemented on a low-cost Rogers 4005C substrate (thickness=0.2 mm and $\varepsilon_r = 3.38$). A linearly-tapered open-slot antenna (LTSA) is chosen for the present work in favor of its broadband operation and relatively high gain [70–73]. It has an approximately frequency-independent geometry, and therefore it is relatively insensitivity to manufacturing error, allowing for the use of low-cost PC board manufacturing. Figure 6.12 compares the manufacturing tolerance of two

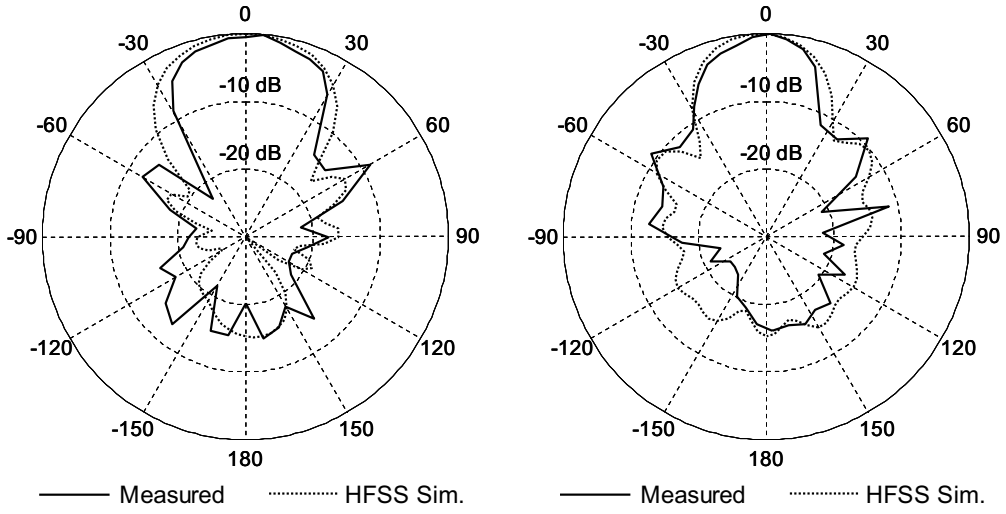

(a) E-plane (vertical)

(b) H-plane (horizontal)

Figure 6.11: Radiation pattern of the sensor LTSA. Solid line: measured, dotted line: HFSS simulation

representative types of planar antennas: patch antenna and LTSA. Patch antennas, in general, have a relatively narrow bandwidth due to their resonant structure, especially on a thin substrate [74]. On the other hand, open slot antennas provide an inherently wideband characteristic due to the non-resonant, travelling-wave mechanism of radiation [75], making their performance less sensitive to small changes in design parameters than patch antennas.

The slot feed line, microstrip line and their transition is carefully designed under the 5 mil resolution constraint [76–78]. The designed antenna has $>$ 10 GHz bandwidth centered at 60 GHz. Its half-power beamwidth is approximately

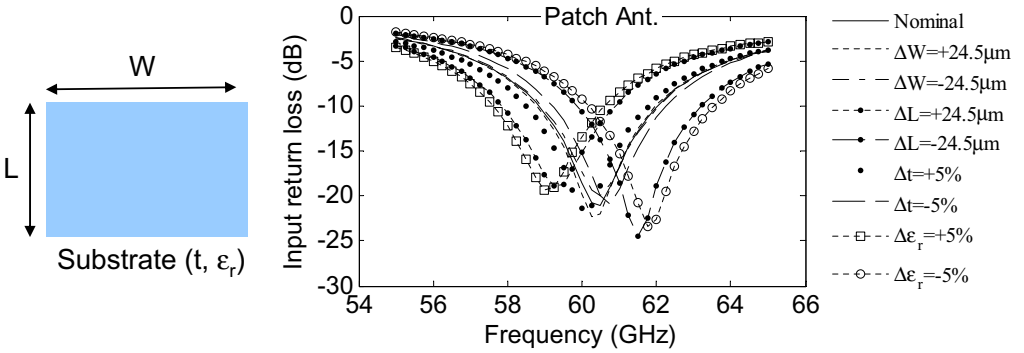

(a) Patch antenna

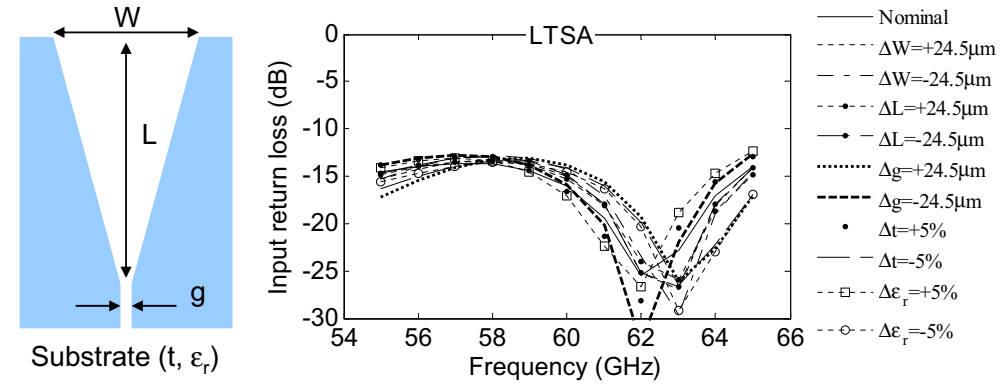

(b) Linearly-tapered open-slot antenna (LTSA)

Figure 6.12: Comparison of manufacturing tolerance between two representative planar-type antennas. The sensitivity of the input impedance match to variations in design parameters, for each type of antenna, is obtained by electromagnetic simulation (Agilent Momentum and Ansoft HFSS for a patch antenna and LTSA, respectively).

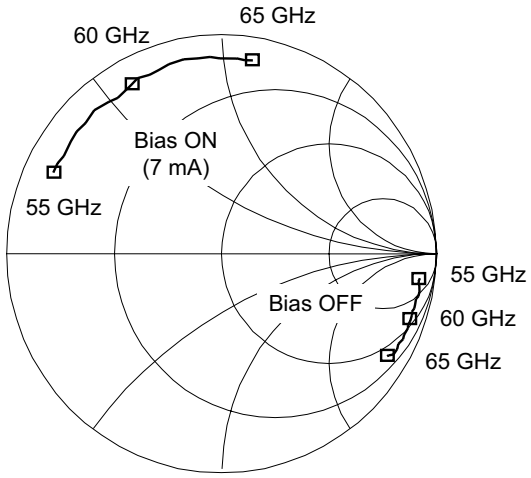

Figure 6.13: Measured impedance of the PIN-diode based one-port modulator.

40 degree with 7 dB of realized gain accounting for loss. The radiation patterns are presented in Figure 6.11.

The collector beam is received by a LTSA terminated by a PIN diode. The input bias turns on and off the PIN diode, presenting two impedance states with approximately 180 degree phase difference (Figure 6.13). The beacon is hence reflected with either 0 or 180 degree relative phase shift, and eventually re-transmitted toward the collector. 16-bit local data and 50 MHz shifting LO (to avoid direct ground returns) are simultaneously imposed on diode bias through a XOR gate. The prototype consumes 7 mA of dc current from a 3 V supply to forward-bias the PIN diode. The dc power consumption will, however, significantly drop (e.g. μW level) if the entire circuit (except for the LTSA) is implemented on silicon.

The current prototype sensor is passive without any active RF amplification. Its reflected power entirely depends on the collector transmit power. On one hand, this suits well with the simplistic sensor approach; the sensor has minimal RF functionality, and corresponding implementation loss can be compensated by raising the beacon power. On the other hand, passive sensors are practically unsuitable for longer range communication (e.g. >1 km). Scaled CMOS devices (e.g. 90-nm node or below) will again provide low-cost millimeterwave amplification [79–83] and help to scale up the sensor network.

6.5 Radio Experiment

In this section, radio link experiments are presented. Figure 6.14 shows the overall experimental setup including collector, sensor and all required instruments.

6.5.1 Experiment Plan

The system is operated in four different settings depending on the presence or absence of range code and sensor data modulation. These mode of operations are deliberately chosen such that comparison of experimental results between different modes will unambiguously reveal a certain performance metric we are interested in.

(a) Collector system on a cart

(b) View from a sensor

Figure 6.14: Photographs of indoor radio experiment

1. *Pilot Mode*: There is no data modulation at the sensor, and the range code at the collector side is also turned off. Therefore, the transmitted waveform from the collector is equal to a pure sinusoid. The received signal by the collector consists of the frequency-shifted sinusoid plus additive Gaussian noise. The parameter of the sinusoid, noise variance and finally the E_b/N_0 at the receiver can be estimated by using the standard maximum-likelihood (ML) method [84].

2. *Data Only*: The data modulation at the sensor node is turned on while the range code is still inactive at the receiver. This mode of operation provides a useful bit error rate statistics which can be compared against the nominal mode where the received signal is also modulated by the range code.

3. *Range Code Only*: The data modulation at the sensor is turned off, with only range code modulation at the collector. This mode of operation provides a useful range estimation statistics which can be compared against the nominal mode where the received signal is also modulated by the sensor data.

4. *Data + Range Code*: This is the nominal mode of sensor network operation, with both sensor data and range code modulation.

First, a comparison of E_b/N_0 will be made between measurement and prediction by link budget analysis. Second, bit error rate (BER) is measured and

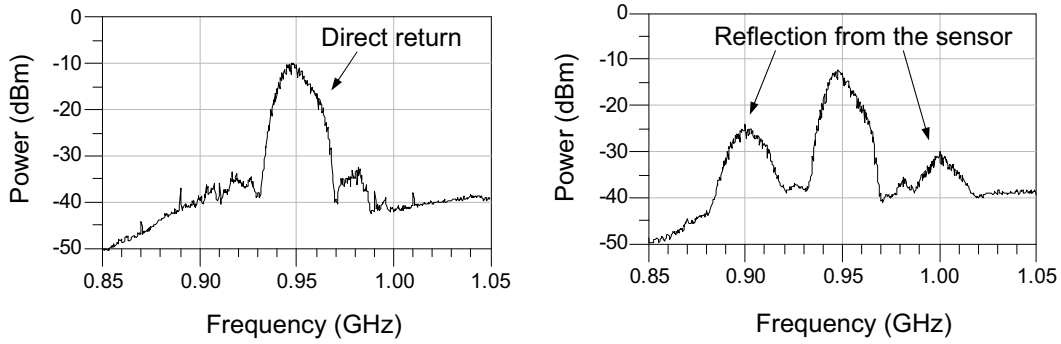

(a) Sensor turned off

(b) Sensor turned on

Figure 6.15: Collector RX-IF2 spectrum with a sensor at 3m. Sensor return signal is seen at 50 MHz away from the 20 MHz PRBS beacon directly reflected from indoor environments.

discussed. Then, the localization performance of the imaging sensor network is demonstrated.

6.5.2 Radio Link Verification

Figure 6.15 shows the received spectrum at the collector IF frequency. Sensor reflection is clearly seen 50 MHz away from the center frequency when the sensor is turned on. In Figure 6.16, the E_b/N_0 measured using the pilot mode is plotted against the expected E_b/N_0 using the radio link characterization in Section 6.2. The collector received power roughly falls as $1/R^4$, as expected by the link equation. In Figure 6.16, the loss of aperture efficiency due to near field effect is also taken into account.

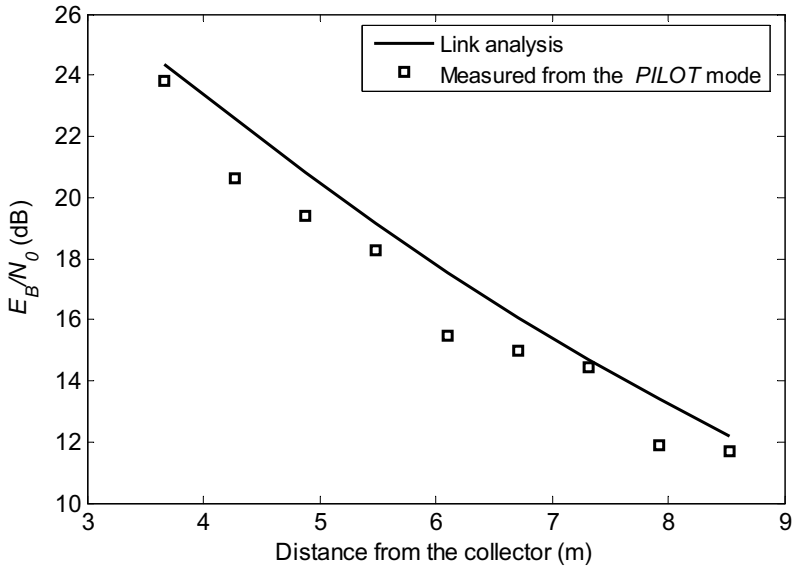

Figure 6.16: Measured versus predicted E_b/N_0

6.5.3 Bit Error Rate

In Figure 6.17, a comparison of the BER performance of the prototype under the nominal and data mode at 100 kbps is shown. The E_b/N_0 for each sensor location is measured from the pilot mode experiments, with the smallest E_b/N_0 in the plot corresponding to the maximum range of 8.54 m. The measured BER for distance less than 5.5 m was less than 10^{-5} (no errors were found in 100,000 bits). It is observed that the BER measured in the nominal mode is only marginally worse (< 1 dB) compared to the data mode. One can, therefore, conclude that data demodulation is not significantly affected by the presence of range code modulation. Nevertheless, the BER in the nominal mode is roughly 4–5 dB worse than the

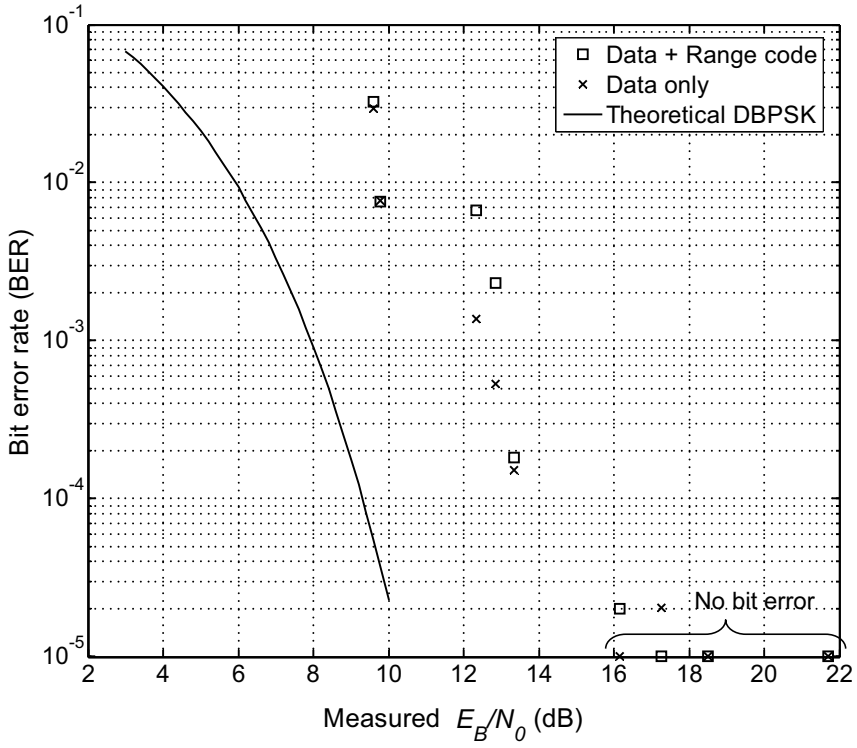

Figure 6.17: Measured BER performance at the sensor data rate of 100 Kbps (based on observing 100,000 bits)

expected BER for DBPSK modulation [85] at the same E_b/N_0. It was found that two factors are mainly responsible for this loss of E_b/N_0: increase in the receiver noise floor due to strong direct echoes, and signal processing implementation loss (especially during the range-code correlation).

6.5.4 Localization

Figure 6.18 shows the range estimate (20 measurements for each point), with the expected range also shown as a dotted line. By comparing Figure 6.18(a) and Figure 6.18(b), one can conclude that the presence of sensor data modulation does not noticeably affect the estimation of range. It is also seen that the range estimate consistently has approximately 12.6 m of offset. This is due to the "electrical" delay (a.k.a *group* delay) present in the collector and sensor electronics. Most RF circuits can be modeled as a cascade of a single L-C section at their passband, which resembles an artificial *delay* line. The delay from these L-C sections, all combined, amounts to 12.6 m, which is an order of magnitude greater than the actual physical size of collector/sensor electronics.

Figure 6.20 and Figure 6.21 illustrates how the 2-D and 3-D localization is done. The color image shown is the magnitude of matched filter output. The peak of each image corresponds to the most likely location of the sensor.

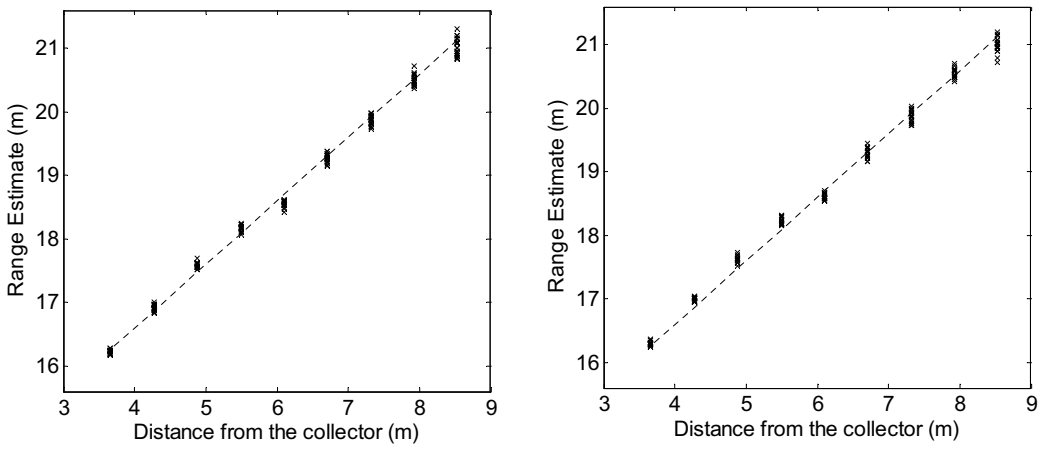

(a) Range Code only

(b) Data + Range Code

Figure 6.18: Measured distance between the collector and sensor. For each sensor location, 20 measurements were carried out.

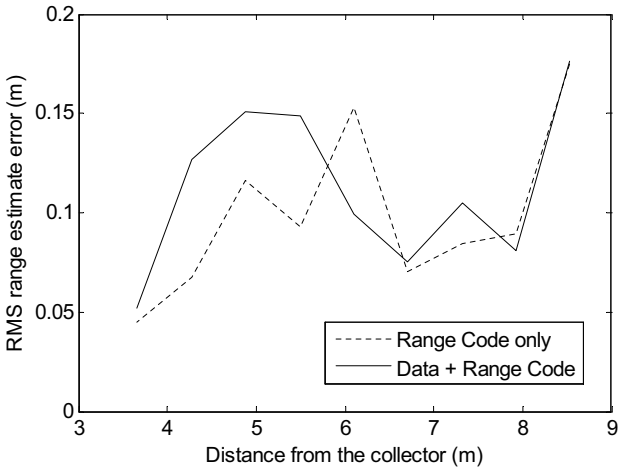

Figure 6.19: RMS range error.

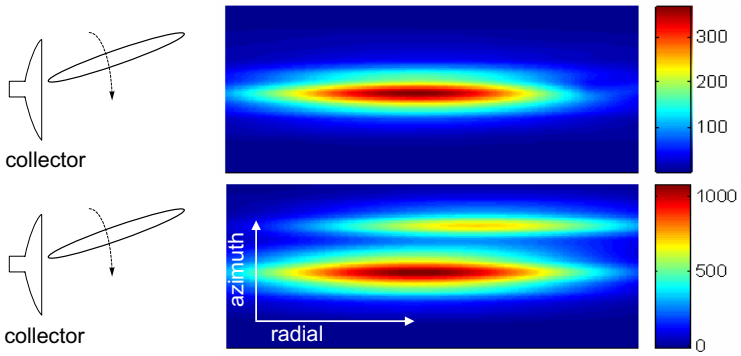

Figure 6.20: An example of 2-D localization: Reconstructed sensor field from the magnitude of 2-D matched filter output with a single sensor(top) and two sensors (bottom). The peak(s) on each map indicate(s) the most probably sensor location(s). Note: maps not to scale; actual field size is 12 m by 0.6 m.

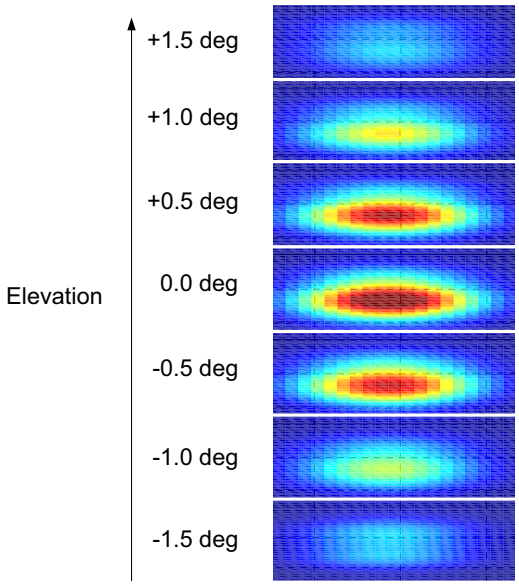

Figure 6.21: An example of 3-D localization

6.6 Conclusions

In this chapter, the basic link, localization and demodulation performance of a prototype 60 GHz wireless sensor network is presented, based on a virtual-imaging approach. One of the main limitations of imaging sensor networks based on a passive sensor is the short communication range, as discussed in Section 6.2. The communication range can be increased by realizing *active* gain in the sensor RF circuitry. Link budget analysis shows that the current state-of-the art RF CMOS technology can, in principle, support up to several kilometers of range. Another viable approach to increase the range is to form a *virtual sensor array* so that the collector can coherently combine signals from each sensor. Research is currently under way to critically evaluate these possibilities [86].

Chapter 7

Conclusions

In this dissertation, the outcome of two research projects is presented: High-resolution time-interleaved A/D conversion (TIADC) system, and millimeter-wave wireless sensor network. In this chapter, key achievements are summarized, as well as related on-going efforts and suggestions for future work.

7.1 Mismatch Correction for TIADCs

Time-interleaved A/D converters (TIADC) provide an architectural solution to a very fast A/D conversion by using multiple parallel ADCs. Their practical use, however, has been limited to low-to-moderate resolution applications due to the nonlinear distortion created by channel mismatches. This thesis presents a series of novel comprehensive, high-resolution correction methods of such channel mismatches under various operating scenarios. Experimental results demonstrated that > 80 dB of spurious-free dynamic range (SFDR) performance can be

achieved after error correction. This level of SFDR represents the state-of-the art at the time of thesis writing, and is believed to satisfy the requirements of most demanding applications.

Specifically, first, a training-based calibration method is developed. Channel mismatches are characterized by applying a known input signal. The design of digital correction filters is based on a modified weighted least squares (WLS) method, where aliasing spurs can be individually controlled. The proposed design method is capable of exploiting signal stop-bands for more efficient error correction than conventional design methods.

Next, *blind* correction methods are proposed and demonstrated, where the TIADC input signal is not known a priori. Instead, statistical signal processing techniques are employed for mismatch estimation under wide-sense stationary (WSS) input assumption. Parameterized filter banks provides a unified framework for mismatch correction. Blind methods are necessary when training-based methods are not effective, for example when system interruption for calibration is not allowed, or when hardware mismatches are substantially time-varying.

A novel mixed-domain approach to the blind method is proposed. Mismatch estimation is performed in the digital domain, but the correction of timing mismatch is achieved in the analog domain by directly tuning sampling clock. This

particular correction method allows for a very efficient hardware implementation for mismatch estimation as well as correction.

7.1.1 Future Work

A/D conversion is an inevitable operation for almost all digital communication receiver. Therefore, if a TIADC is part of the receiver, we can consider combining TIADC mismatch correction with channel equalization. This may enable a better system-level trade-off without significantly increasing the complexity due to mismatch correction. We can also actively exploit the specific signal format to aid mismatch estimation. One such example is the estimation of offset mismatches for OFDM receivers [87]. Overall, this communication-receiver-oriented approach is relatively unexplored so far, but is under active investigation at UCSB [88].

Time-interleaved operation can also be used for digital-to-analog (D/A) conversion as well, although so far it has been employed almost exclusively for A/D conversion. The overall sampling rate is multiplied by the number of DAC channels, and this can be useful for ultra-fast signal generation. See e.g. [89] for the application of time-interleaved D/A converter (TIDAC) in a UWB transmitter.

Digital signal processing in this dissertation is mostly done on MATLAB after data acquisition from the $M = 4$ experimental prototype. Monolithic implementation (e.g. CMOS) of the proposed correction methods will be therefore of interest

for low-cost and low-power applications. In particular, the mixed-domain blind method, introduced in Chapter 5, allows for a very efficient monolithic implementation. To obtain gain and timing mismatch estimates, online calculation of two correlation coefficients is all that is necessary (i.e. two multipliers and accumulators per each channel). Adjustable clock tuning is also easily implemented. This will make feasible a single-chip, high-resolution ($>$ 80 dB) TIADC with background correction circuitry for high-speed instrumentation, communication, radar, etc.

7.2 Millimeterwave Wireless Sensor Network

An entirely novel approach to wireless sensor network (WSN) is proposed and demonstrated by a 60-GHz experimental prototype in collaboration with Prof. Madhow's research group at UCSB. A sophisticated information collector sweeps a millimeterwave beam across the sensor field for data gathering as well as sensor localization. Key motivation is simplistic, minimalistic sensor hardware in favor of very large-scale networks. The system, instead, exploits millimeterwave frequencies and signal processing techniques at the collector side to compensate for simplistic sensor hardware. The proposed approach draws upon an imaging principle, interpreting sensors as a reflective source, or a "pixel." The 60-GHz pro-

totype system consists of a collector transceiver, mechanically steerable high-gain antenna, signal-processing algorithms and diode-based passive sensors. Results from indoor radio experiment have been presented.

7.2.1 Future Work

In a typical wireless sensor network, sensor nodes are subject to severe energy constraint. In this circumstance, the energy consumption of a sensor needs to be minimized for a longer battery life. The dc power consumption of the prototype 60 GHz sensor is on the order of 20 mW, which is dominated by the PIN diode bias current. To significantly reduce the dc power consumption, the entire sensor circuitry is recently designed and fabricated in 90-nm CMOS process. Key building blocks are ultra low-power ring oscillator [90] and 60 GHz impedance modulator. Characterization of the IC is currently under way, and the measured dc power consumption is less than 10 μW (A button-sized Lithium battery will last more than one year at this level of dc power consumption).

The current 60-GHz prototype is based on passive-type sensors, which reflects a millimeterwave beacon from the collector. While this enables very simple sensor hardware, the communication range is severely limited due to the small sensor transmit power. One way to increase the range is to implement *active* gain on the sensor. Recently, deep sub-micron CMOS technologies (e.g. 90-nm or be-

low) prove useful for low-cost millimeterwave amplification [79–83]. Link-budget analysis shows that the sensor field can be scaled up to several kilometers by using *active* sensors in the 60 GHz bands.

The current collector prototype performs mechanical beam sweeping. Electrical beamsteering by a phased array system is an attractive option, since this is more flexible, and enables substantially faster beam sweeping. System reliability can also be enhanced by minimizing mechanically moving parts. The design and implementation of a millimeterwave phased-array system is, however, challenging. Currently, a millimeterwave phased-array transmitter in a SiGe technology, capable of 2-D beam sweeping, is under development at UCSB [91].

Another very interesting option to scale up the proposed sensor network is *distributed* beamforming, where a number of neighboring passive sensors collaborate with others to form a large equivalent phased array [92–94]. The challenge is to line up the phase and frequency of RF carriers from randomly distributed sensors, to achieve in-phase power combining at the collector receiver. This is in contrast to conventional *regular* beamformers, where each transmitting/receiving element is at a known position with a common frequency standard. The distributed beamforming approach with unknown sensor frequency/phase is currently under active investigation [86].

Bibliography

[1] "Rethinking Analog Design." [Online]. Available: http://rad.stanford.edu/

[2] F. Zhao and L. Guibas, *Wireless Sensor Networks: An Information Processing Approach*. Morgan Kaufmann, 2004.

[3] A. Cerpa, J. Elson, D. Estrin, L. Girod, M. Hamilton, , and J. Zhao, "Habitat monitoring: Application driver for wireless communications technology," *ACM SIGCOMM Workshop on Data Communications in Latin America and the Caribbean*, Apr. 2001.

[4] J. Lundquist, D. Cayan, , and M. Dettinger, "Meteorology and hydrology in yosemite national park: A sensor network application," *Proc. Information Processing in Sensor Networks (IPSN)*, Apr. 2003.

[5] G. Werner-Allen, K. Lorincz, M. Ruiz, O. Marcillo, J. Johnson, J. Lees, and M. Welsh, "Deploying a wireless sensor network on an active volcano," *Internet Computing, IEEE*, vol. 10, no. 2, pp. 18–25, March-April 2006.

[6] J. Lundquist, D. Cayan, , and M. Dettinger, "A survey of research on context-aware homes," *Wearable, Invisible, Context-Aware, Ambient, Pervasive and Ubiquitous Computing (WICAPUC)*, Feb. 2003.

[7] D. Puccinelli and M. Haenggi, "Wireless sensor networks: applications and challenges of ubiquitous sensing," *IEEE Circuits and Systems Magazine*, vol. 5, no. 3, pp. 19–31, 2005.

[8] I. Akyildiz, W. Su, Y. Sankarasubramaniam, and E. Cayirci, "A survey on sensor networks," *Communications Magazine, IEEE*, vol. 40, no. 8, pp. 102–114, Aug. 2002.

[9] M. Vossiek, L. Wiebking, P. Gulden, J. Wieghardt, C. Hoffmann, and P. Heide, "Wireless local positioning," *Microwave Magazine, IEEE*, vol. 4, no. 4, pp. 77–86, Dec. 2003.

[10] P. Gupta and P. Kumar, "The capacity of wireless networks," *Information Theory, IEEE Transactions on*, vol. 46, no. 2, pp. 388–404, Mar. 2000.

[11] M. Seo, M. Rodwell, and U. Madhow, "Comprehensive digital correction of mismatch errors for a 400-msamples/s 80-dB SFDR time-interleaved analog-to-digital converter," *Microwave Theory and Techniques, IEEE Transactions on*, vol. 53, no. 3, pp. 1072–1082, Mar. 2005.

[12] W. Black, Jr. and D. Hodges, "Time interleaved converter arrays," *IEEE Journal of Solid-State Circuits*, vol. 15, no. 6, pp. 1022–1029, Dec. 1980.

[13] K. Poulton, J. Corcoran, and T. Hornak, "A 1-GHz 6-bit ADC system," *IEEE Journal of Solid-State Circuits*, vol. 22, no. 6, pp. 962–970, Dec. 1987.

[14] A. Montijo and K. Rush, "Accuracy in interleaved ADC systems," *Hewlett Packard J.*, vol. 44, no. 5, pp. 38–46, Oct. 1993.

[15] T. Clark and P. Matthews, "Real-time photonic analog-digital converter based on discrete wavelength-time mapping," *Int. Topical Microwave Photonics Meeting*, vol. 1, pp. 231–234, Nov. 1999.

[16] R. Williamson, P. Juodawlkis, J. Wasserman, G. Betts, and J. Twichell, "Effects of crosstalk in demultiplexers for photonic analog-to-digital converters," *J. Lightw. Technol.*, vol. 19, no. 2, pp. 230–236, Feb. 2001.

[17] J. Twichell, J. Wasserman, P. Juodawlkis, G. Betts, and R. Williamson, "High-linearity 208-MS/s photonic analog-to-digital converter using 1-to-4 optical time-division demultiplexers," *Photonics Technology Letters, IEEE*, vol. 13, no. 7, pp. 714–716, Jul. 2001.

[18] P. Juodawlkis, J. Twichell, G. Betts, J. Hargreaves, R. Younger, J. Wasserman, F. O'Donnell, K. Ray, and R. Williamson, "Optically sampled analog-to-digital converters," *Microwave Theory and Techniques, IEEE Transactions on*, vol. 49, no. 10, pp. 1840–1853, Oct. 2001.

[19] K. Poulton, R. Neff, A. Muto, W. Liu, A. Burstein, and M. Heshami, "A 4 Gsample/s 8b ADC in 0.35 μm CMOS," *Solid-State Circuits Conference, 2002. Digest of Technical Papers. ISSCC. 2002 IEEE International*, vol. 1, pp. 166–457, 2002.

[20] K. Poulton, R. Neff, B. Setterberg, B. Wuppermann, T. Kopley, R. Jewett, J. Pernillo, C. Tan, and A. Montijo, "A 20 GS/s 8 b ADC with a 1 MB memory in 0.18 μm CMOS," *Solid-State Circuits Conference, 2003. Digest*

of Technical Papers. ISSCC. 2003 IEEE International, vol. 1, pp. 318–496, 9-13 Feb. 2003.

[21] Y.-C. Jenq, "Digital spectra of nonuniformly sampled signals: fundamentals and high-speed waveform digitizers," *Instrumentation and Measurement, IEEE Transactions on*, vol. 37, no. 2, pp. 245–251, Jun. 1988.

[22] ——, "Digital spectra of nonuniformly sampled signals: a robust sampling time offset estimation algorithm for ultra high-speed waveform digitizers using interleaving," *Instrumentation and Measurement, IEEE Transactions on*, vol. 39, no. 1, pp. 71–75, Feb. 1990.

[23] C. Conroy, D. Cline, and P. Gray, "An 8-b 85-MS/s parallel pipeline A/D converter in 1-μm CMOS," *Solid-State Circuits, IEEE Journal of*, vol. 28, no. 4, pp. 447–454, Apr. 1993.

[24] K. Dyer, D. Fu, S. Lewis, and P. Hurst, "An analog background calibration technique for time-interleaved analog-to-digital converters," *Solid-State Circuits, IEEE Journal of*, vol. 33, no. 12, pp. 1912–1919, Dec. 1998.

[25] D. Hummels, I. Mcdonald, J.J., and F. Irons, "Distortion compensation for time-interleaved analog to digital converters," *Instrumentation and Measurement Technology Conference, 1996. IMTC-96. Conference Proceedings, IEEE*, vol. 1, pp. 728–731, 1996.

[26] Y.-C. Jenq, "Perfect reconstruction of digital spectrum from nonuniformly sampled signals," *Instrumentation and Measurement, IEEE Transactions on*, vol. 46, no. 3, pp. 649–652, Jun. 1997.

[27] D. Fu, K. Dyer, S. Lewis, and P. Hurst, "A digital background calibration technique for time-interleaved analog-to-digital converters," *Solid-State Circuits, IEEE Journal of*, vol. 33, no. 12, pp. 1904–1911, Dec. 1998.

[28] H. Jin and E. Lee, "A digital-background calibration technique for minimizing timing-error effects in time-interleaved ADCs," *Circuits and Systems II: Analog and Digital Signal Processing, IEEE Transactions on [see also Circuits and Systems II: Express Briefs, IEEE Transactions on]*, vol. 47, no. 7, pp. 603–613, Jul. 2000.

[29] S. Jamal, D. Fu, N.-J. Chang, P. Hurst, and S. Lewis, "A 10-b 120-Msample/s time-interleaved analog-to-digital converter with digital background calibration," *Solid-State Circuits, IEEE Journal of*, vol. 37, no. 12, pp. 1618–1627, Dec. 2002.

[30] W. Namgoong, "Finite-length synthesis filters for non-uniformly time-interleaved analog-to-digital converter," *Circuits and Systems, 2002. ISCAS 2002. IEEE International Symposium on*, vol. 4, pp. 815–818, 2002.

[31] J. Pereira, P. Girao, and A. Serra, "An FFT-based method to evaluate and compensate gain and offset errors of interleaved ADC systems," *Instrumentation and Measurement, IEEE Transactions on*, vol. 53, no. 2, pp. 423–430, Apr. 2004.

[32] A. Petraglia and S. Mitra, "Analysis of mismatch effects among A/D converters in a time-interleaved waveform digitizer," *Instrumentation and Measurement, IEEE Transactions on*, vol. 40, no. 5, pp. 831–835, Oct. 1991.

[33] B. Yu and J. Black, W.C., "Error analysis for time-interleaved analog channels," *Circuits and Systems, 2001. ISCAS 2001. The 2001 IEEE International Symposium on*, vol. 1, pp. 468–471, 6-9 May 2001.

[34] N. Kurosawa, H. Kobayashi, K. Maruyama, H. Sugawara, and K. Kobayashi, "Explicit analysis of channel mismatch effects in time-interleaved ADC systems," *Circuits and Systems I: Fundamental Theory and Applications, IEEE Transactions on [see also Circuits and Systems I: Regular Papers, IEEE Transactions on]*, vol. 48, no. 3, pp. 261–271, Mar. 2001.

[35] S. Velazquez, "Hybrid filter banks for analog/digital conversion," Ph.D. dissertation, Dept. Elect. Eng. Comput. Sci., MIT, Cambridge, MA, 1997.

[36] S. R. Velazquez and R. J. Velazquez, "Parallel processing analog and digital converter," U.S. Patent 6 473 013, Oct. 29, 2002.

[37] P. Lowenborg, "Asymmetric filter banks for mitigation of mismatch errors in high-speed analog-to-digital converters," Ph.D. dissertation, Dept. Elect. Eng., Linkoping Univ., Linkoping, Sweden, Dec. 2002.

[38] A. Petraglia and S. Mitra, "High-speed A/D conversion incorporating a QMF bank," *Instrumentation and Measurement, IEEE Transactions on*, vol. 41, no. 3, pp. 427–431, Jun. 1992.

[39] S. Velazquez, T. Nguyen, and S. Broadstone, "Design of hybrid filter banks for analog/digital conversion," *Signal Processing, IEEE Transactions on [see also Acoustics, Speech, and Signal Processing, IEEE Transactions on]*, vol. 46, no. 4, pp. 956–967, Apr. 1998.

[40] "AD12400: 12-Bit, 400 MSPS A/D converter data sheet," Analog Devices Inc., Norwood, MA, 2004. [Online]. Available: http://www.analog.com

[41] "AD12500: 12-Bit, 500 MSPS A/D converter data sheet," Analog Devices Inc., Norwood, MA, 2003. [Online]. Available: http://www.analog.com

[42] S. Mitra, *Digital Signal Processing: A Computer-Based Approach.* New York: McGraw-Hill, 2001.

[43] T. Moon and W. Stirling, *Mathematical Methods and Algorithms for Signal Processing.* Upper Saddle River, NJ: Prentice-Hall, 2000.

[44] T. Parks and C. Burrus, *Digital Filter Design.* New York: Wiley, 1987.

[45] V. Valimaki, "Discrete-time modeling of acoustic tubes using fractional delay filters," Ph.D. dissertation, Dept. Elect. Commun. Eng., Helsinki Univ. Technol., Helsinki, Finland, 1995.

[46] "AD6645: 14-Bit, 80/105 MSPS A/D converter data sheet," Analog Devices Inc., Norwood, MA, 2003. [Online]. Available: http://www.analog.com

[47] A. Oppenheim, *Disctete-Time Signal Processing.* Englewood Cliffs, NJ: Prentice-Hall, 1989.

[48] S. Jamal, D. Fu, M. Singh, P. Hurst, and S. Lewis, "Calibration of sample-time error in a two-channel time-interleaved analog-to-digital converter," *Circuits and Systems I: Regular Papers, IEEE Transactions on [Circuits and Systems I: Fundamental Theory and Applications, IEEE Transactions on]*, vol. 51, no. 1, pp. 130–139, Jan. 2004.

[49] V. Divi and G. Wornell, "Signal recovery in time-interleaved analog-to-digital converters," *Acoustics, Speech, and Signal Processing, 2004. Proceedings. (ICASSP '04). IEEE International Conference on*, vol. 2, pp. 593–596, 17-21 May 2004.

[50] J. Elbornsson, F. Gustafsson, and J.-E. Eklund, "Blind adaptive equalization of mismatch errors in a time-interleaved A/D converter system," *Circuits and Systems I: Regular Papers, IEEE Transactions on [Circuits and Systems I: Fundamental Theory and Applications, IEEE Transactions on]*, vol. 51, no. 1, pp. 151–158, Jan. 2004.

[51] ——, "Blind equalization of time errors in a time-interleaved ADC system," *Signal Processing, IEEE Transactions on [see also Acoustics, Speech, and*

Signal Processing, IEEE Transactions on], vol. 53, no. 4, pp. 1413–1424, Apr. 2005.

[52] P. Vaidyanathan, *Multirate Systems and Filter Banks*. Englewood Cliffs, NJ: Prentice-Hall, 1993.

[53] Y. Eldar and A. Oppenheim, "Filterbank reconstruction of bandlimited signals from nonuniform and generalized samples," *Signal Processing, IEEE Transactions on [see also Acoustics, Speech, and Signal Processing, IEEE Transactions on]*, vol. 48, no. 10, pp. 2864–2875, Oct. 2000.

[54] W. Gardner, *Introduction to Random Processes with Application to Signals and Systems*. New York: McGraw-Hill, 1989.

[55] S. Ohno and H. Sakai, "Optimization of filter banks using cyclostationary spectral analysis," *Signal Processing, IEEE Transactions on [see also Acoustics, Speech, and Signal Processing, IEEE Transactions on]*, vol. 44, no. 11, pp. 2718–2725, Nov. 1996.

[56] M. Seo, M. Rodwell, and U. Madhow, "Blind correction of gain and timing mismatches for a two-channel time-interleaved analog-to-digital converter: Experimental verification," *Circuits and Systems, 2006. ISCAS 2006. Proceedings. 2006 IEEE International Symposium on*, pp. 3394–3397, 21-24 May 2006.

[57] ——, "Blind Correction of Gain and Timing Mismatches for a Two-Channel Time-Interleaved Analog-to-Digital Converter," *Signals, Systems and Computers, 2005. Conference Record of the Thirty-Ninth Asilomar Conference on*, pp. 1121–1125, Oct. 28 - Nov. 1, 2005.

[58] V. Divi and G. Wornell, "Scalable blind calibration of timing skew in high-resolution time-interleaved ADCs," *Circuits and Systems, 2006. ISCAS 2006. Proceedings. 2006 IEEE International Symposium on*, 21-24 May 2006.

[59] E. Iroaga, B. Murmann, and L. Nathawad, "A background correction technique for timing errors in time-interleaved analog-to-digital converters," *Circuits and Systems, 2005. ISCAS 2005. IEEE International Symposium on*, pp. 5557–5560, 23-26 May 2005.

[60] S. Huang and B. Levy, "Adaptive blind calibration of timing offset and gain mismatch for two-channel time-interleaved ADCs," *Circuits and Systems I: Regular Papers, IEEE Transactions on [Circuits and Systems I: Fundamental*

Theory and Applications, IEEE Transactions on], vol. 53, no. 6, pp. 1278–1288, June 2006.

[61] S. Huang and B. C. Levy, "Blind Calibration of Timing Offsets for Four-Channel Time-Interleaved ADCs," *Circuits and Systems I: Regular Papers, IEEE Transactions on [Circuits and Systems I: Fundamental Theory and Applications, IEEE Transactions on]*, vol. 54, no. 4, pp. 863–876, April 2007.

[62] C.-Y. Wang and J.-T. Wu, "A background timing-skew calibration technique for time-interleaved analog-to-digital converters," *Circuits and Systems II: Express Briefs, IEEE Transactions on [see also Circuits and Systems II: Analog and Digital Signal Processing, IEEE Transactions on]*, vol. 53, no. 4, pp. 299–303, April 2006.

[63] M. Seo, M. Rodwell, and U. Madhow, "A Low Computation Adaptive Blind Mismatch Correction for Time-Interleaved ADCs," *Circuits and Systems, 2006. MWSCAS '06. 49th IEEE International Midwest Symposium on*, vol. 1, pp. 292–296, 6-9 Aug. 2006.

[64] S. Haykin, *Adaptive Filter Theory*, 4th ed. Upper Saddle River, NJ: Prentice-Hall, 2002.

[65] B. Ananthasubramaniam and U. Madhow, "Virtual radar imaging for sensor networks," *Information Processing in Sensor Networks, 2004. IPSN 2004. Third International Symposium on*, pp. 294–300, 26-27 Apr. 2004.

[66] M. Seo, B. Ananthasubramaniam, M. Rodwell, and U. Madhow, "Millimeterwave Imaging Sensor Nets: A scalable 60-GHz wireless sensor network," *Microwave Symposium, 2007. IEEE/MTT-S International*, pp. 563–566, 3-8 June 2007.

[67] ——, "Recent progress on a 60-GHz imaging sensor network," *40th Asilomar Conference on Signals, Systems, and Computers*, Oct. 2007.

[68] J. Kraus, *Antennas*. McGraw-Hill, 1988.

[69] F. Gardner, "A BPSK/QPSK Timing-Error Detector for Sampled Receivers," *Communications, IEEE Transactions on [legacy, pre - 1988]*, vol. 34, no. 5, pp. 423–429, May 1986.

[70] K. Yngvesson, T. Korzeniowski, Y.-S. Kim, E. Kollberg, and J. Johansson, "The tapered slot antenna-a new integrated element for millimeter-wave applications," *Microwave Theory and Techniques, IEEE Transactions on*, vol. 37, no. 2, pp. 365–374, Feb. 1989.

[71] S. Prasad and S. Mahapatra, "A new MIC slot-line aerial," *Antennas and Propagation, IEEE Transactions on [legacy, pre - 1988]*, vol. 31, no. 3, pp. 525–527, May 1983.

[72] D. Schaubert, E. Kollberg, T. Korzeniowski, T. Thungren, J. Johansson, and K. Yngvesson, "Endfire tapered slot antennas on dielectric substrates," *Antennas and Propagation, IEEE Transactions on [legacy, pre - 1988]*, vol. 33, no. 12, pp. 1392–1400, Dec. 1985.

[73] S. Reynolds, B. Floyd, U. Pfeiffer, T. Beukema, T. Zwick, J. Grzyb, D. Liu, and B. Gaucher, "Progress toward a low-cost millimeter-wave silicon radio," *Custom Integrated Circuits Conference, 2005. Proceedings of the IEEE 2005*, pp. 563–570, 18-21 Sep. 2005.

[74] D. Pozar, "Considerations for millimeter wave printed antennas," *Antennas and Propagation, IEEE Transactions on [legacy, pre - 1988]*, vol. 31, no. 5, pp. 740–747, Sep. 1983.

[75] P. Gibson, "The Vivaldi aerial," *9th European Microwave Conference*, pp. 101–105, 17-20, Sept. 1979.

[76] S. Cohn, "Slot line on a dielectric substrate," *Microwave Theory and Techniques, IEEE Transactions on*, vol. 17, no. 10, pp. 768–778, Oct. 1969.

[77] E. Mariani, C. Heinzman, J. Agrios, and S. Cohn, "Slot Line Characteristics," *Microwave Theory and Techniques, IEEE Transactions on*, vol. 17, no. 12, pp. 1091–1096, Dec. 1969.

[78] J. Knorr, "Slot-Line Transitions," *Microwave Theory and Techniques, IEEE Transactions on*, vol. 22, no. 5, pp. 548–554, May 1974.

[79] B. Heydari, M. Bohsali, and A. M. Adabi, E. abd Niknejad, "Millimeter-Wave Devices and Circuit Blocks up to 104 GHz in 90 nm CMOS," *Solid-State Circuits, IEEE Journal of*, vol. 42, no. 12, pp. 2893–2903, Dec. 2007.

[80] T. Yao, M. Q. Gordon, K. K. W. Tang, K. H. K. Yau, M.-T. Yang, P. Schvan, and S. P. Voinigescu, "Algorithmic Design of CMOS LNAs and PAs for 60-GHz Radio," *Solid-State Circuits, IEEE Journal of*, vol. 42, no. 5, pp. 1044–1057, May 2007.

[81] T. Dickson, K. Yau, T. Chalvatzis, A. Mangan, E. Laskin, R. Beerkens, P. Westergaard, M. Tazlauanu, M.-T. Yang, and S. Voinigescu, "The Invariance of Characteristic Current Densities in Nanoscale MOSFETs and Its

Impact on Algorithmic Design Methodologies and Design Porting of Si(Ge) (Bi)CMOS High-Speed Building Blocks," *Solid-State Circuits, IEEE Journal of*, vol. 41, no. 8, pp. 1830–1845, Aug. 2006.

[82] B. Razavi, "A 60-GHz CMOS receiver front-end," *Solid-State Circuits, IEEE Journal of*, vol. 41, no. 1, pp. 17–22, Jan. 2006.

[83] C. Doan, S. Emami, A. Niknejad, and R. Brodersen, "Millimeter-wave CMOS design," *Solid-State Circuits, IEEE Journal of*, vol. 40, no. 1, pp. 144–155, Jan. 2005.

[84] L. Sharf, *Statistical Signal Processing: Detection, Estimation and Time Series Analysis*. Addison-Wesley, 1991.

[85] J. Proakis, *Digital Communications*. McGraw-Hill, 2001.

[86] M. Seo, M. Rodwell, and U. Madhow, "A feedback-based distributed phased array technique and its application to 60-GHz wireless sensor network," *submitted to 2008 IEEE/MTT-S International Microwave Symposium*.

[87] Y. Oh and B. Murmann, "System embedded ADC calibration for OFDM receivers," *Circuits and Systems I: Regular Papers, IEEE Transactions on [Circuits and Systems I: Fundamental Theory and Applications, IEEE Transactions on]*, vol. 53, no. 8, pp. 1693–1703, Aug. 2006.

[88] "Signal Processing with Low-Precision A/D Conversion: A Framework for Low-Cost Gigabit Wireless Communication," WCSL posters presented at Engineering Insights 2006, UCSB, CA, 2006. [Online]. Available: http://sputnik.ece.ucsb.edu/wcsl/currentresearch.html

[89] C. Krall, C. Vogel, and K. Witrisal, "Time-Interleaved Digital-to-Analog Converters for UWB Signal Generation," *Ultra-Wideband, 2007. ICUWB 2007. IEEE International Conference on*, pp. 366–371, 24-26 Sept. 2007.

[90] B. Warneke and K. Pister, "An ultra-low energy microcontroller for Smart Dust wireless sensor networks," *Solid-State Circuits Conference, 2004. Digest of Technical Papers. ISSCC. 2004 IEEE International*, vol. 1, pp. 316–317, 15-19 Feb. 2004.

[91] C. Carta, M. Seo, and M. Rodwell, "A mixed-signal row/column architecture for very large monolithic mm-Wave phased arrays," *International Journal of High Speed Electronics and Systems*, vol. 17, no. 7, pp. 111–114, Jun. 2007.

[92] H. Ochiai, P. Mitran, H. Poor, and V. Tarokh, "Collaborative beamforming for distributed wireless ad hoc sensor networks," *IEEE Transactions on Signal Processing]*, vol. 53, no. 11, pp. 4110–4124, Nov. 2005.

[93] R. Mudumbai, G. Barriac, and U. Madhow, "On the Feasibility of Distributed Beamforming in Wireless Networks," *Wireless Communications, IEEE Transactions on*, vol. 6, no. 5, pp. 1754–1763, May 2007.

[94] R. Mudumbai, J. Hespanha, U. Madhow, and G. Barriac, "Scalable feedback control for distributed beamforming in sensor networks," *Information Theory, 2005. ISIT 2005. Proceedings. International Symposium on*, pp. 137–141, 4-9 Sep. 2005.